

Πανεπιστήμιο Κρήτης
Σχολή Θετικών και Τεχνολογικών Επιστημών
Φυσικό Τμήμα

Μελέτη Βιολογικών λειτουργιών με
Μοριακή Τομογραφία Φθορισμού

Ανίκητος Γαροφαλάκης

Υπεύθυνος Καθηγητής : Ελευθέριος Ν. Οικονόμου

Υπεύθυνος Ερευνητής : Jorge Ripoll

Ηράκλειο 2007

Fluorescence molecular tomography and in-vivo applications

Anikitos Garofalakis

Heraklion, March 2007

Tutor: Eleftherios N. Economou

Supervisor: Jorge Ripoll

Abstract

Given that Optical Tomography is capable of quantitatively imaging the distribution of fluorophores and fluorescent proteins in-vivo, there has been a great deal of interest in developing optical imaging systems under optimal experimental conditions. A novel system has been implemented that enables three dimensional (3D) imaging of fluorescent probes in whole animals using a non-contact setup, in parallel with a 3D surface reconstruction algorithm. The non-contact approach is a significant step forward in terms of experimental simplicity and provides comfort to the targeted animal. It allows the use of a CCD cameras as detector, resulting in large data sets, thus improving the accuracy of the inversion models used for quantitative 3D reconstruction of fluorochrome distribution, as well as facilitating imaging with higher spatial resolution.

In this study the system is tested in determining the distribution of Green Fluorescent Protein (GFP) expressed by T-lymphocytes in the hCD2-GFP transgenic mouse model, thus demonstrating the potential of the system for studying the immunology-based studies. In-vivo measurements have been also carried in the GFP CLIP-170 mouse model.

Contents

1	Introduction	3
1.1	Optical imaging	4
1.2	Non contact measurements	6
1.3	The forward and the inverse problem	7
2	Theory of diffuse light	9
2.1	From the radiative transfer equation to the diffusion equation	10
2.1.1	Transport Properties	11
2.1.2	Flux conservation	12
2.1.3	Diffusion Approximation	13
2.1.4	Fick's Law	14
2.2	The Diffusion Equation	15
2.3	High absorbing media	15
2.3.1	The diffusion coefficient in high absorbing media	17
2.4	Solutions of the diffusion equation for infinite homogeneous media	18
2.4.1	The excitation source term: the Continuous Wave (CW) laser source . .	19
2.4.1.1	Time dependent illumination sources	20
2.4.2	The fluorescent source term	21
2.4.2.1	The Born approximation	22
2.4.2.2	Propagation of fluorescent light	23
3	Solutions for bounded media	25
3.1	The diffusion approximation in arbitrary geometries	25
3.1.1	Boundary Conditions	26
3.1.2	The expression for the flux at the boundary	27
3.2	Free space propagation, the basis for non-contact tomography	28
3.3	From finite to infinite	32
4	Inverse problem	36
4.1	The Normalized Born algorithm	36
4.2	Discretization and the weight matrix	38

4.3 The Algebraic Reconstruction Technique (ART)	39
5 Materials and Methods	42
5.1 Transgenic mice	42
5.2 Tissue-like phantoms	43
5.3 Experimental setup	44
5.3.1 First generation setup	45
5.3.2 Second generation setup	46
5.3.2.1 Fast laser scanning	48
5.3.3 Synchronization of the devices	48
5.3.4 Comparison between the two systems	49
5.4 Multi-subject Tomography	49
5.5 Flow cytometry	50
6 Experimental protocol	53
6.1 Mouse treatment	53
6.2 Experimental protocol	55
6.2.1 Data collection	56
6.3 Data treatment	58
6.3.1 Surface geometry extraction	59
6.3.1.1 Surface Reconstruction Algorithm	59
6.3.2 Data projection	61
6.3.3 Inversion	62
7 In vivo experiments and results	64
7.1 Calibration	64
7.2 Imaging of the lymphoid organs	66
7.2.1 Adult mouse imaging	66
7.2.1.1 Thymus imaging: comparison with a control mouse	67
7.2.1.2 Cervical lymph nodes	69
7.2.1.3 Spleen imaging	71
7.3 Newborn imaging	72
7.3.1 Thymus monitoring	73
7.3.2 Cervical lymph nodes	75
7.3.3 Armpit lymph node	78
7.4 Quantification	78
7.5 Testis Imaging	79
8 Conclusions and future outlook	83

Chapter 1

Introduction

Over the last years, optical tomography is being established as one of the main tomographic modalities applied to molecular imaging studies [1]. Molecular Imaging can be defined as the application of non-invasive techniques for the visualization of molecular events in the cellular or the subcellular level, inside intact living systems [2, 3]. Molecular Imaging is a relatively new and rapidly growing discipline that merges aspects from different scientific fields. The rapid growth of Molecular Imaging has been mainly stimulated from advances in molecular biology¹ that have provided scientists with new exciting tools for the visualization of molecular processes in intact organisms [2]. Among the variety of molecular imaging probes, optical probes have allowed the implementation of optical imaging techniques for molecular imaging studies [4].

Optical imaging, before its adaptation as an molecular imaging modality, had already proved its potential for probing in deep tissues, mostly for clinical studies [5, 6]. Since the first approaches in formulating the theoretical framework for describing the propagation of light in tissue media [7, 8], the optical method has received great attention [9]. Light interaction with different tissue components enables the visualization of tissue abnormalities or pathologic processes [10, 9], thus medical applications of optical imaging techniques cover a wide range from probing hemodynamics [11, 12] to detecting tumors [13, 5, 6, 14] and providing functional imaging of the brain [15, 16]. In most medical applications the source of contrast is inherent (e.g. tissue absorption or scattering) relying upon correlating the scattering and the absorption of tissue with morphological changes caused by any pathological condition such as diseases.

Pathological and morphological changes, however, are the end effect of processes that occur at the molecular level. The direct visualization of molecular events, underlying disease or biological processes in general, would be of great importance. Molecular biology and Biotechnology have provided tools for the labelling cells and molecules with fluorescent probes which are valuable contrast agents for optical imaging studies [4]. Fluorescent contrast agents², first

¹Molecular Biology is the branch of biology that studies the structure and activity of macromolecules essential to life (such as proteins and nucleic acids)

²compounds used to improve the contrast of internal bodily structures and incorporate fluorescence as a source of contrast

applied in cell biology [17, 18] and cell microscopy [19], provide high signal to noise ratios and high specificity³, thus significantly improving the detection limit, the resolution and the depth localization efficacy. Fluorochromes, Fluorescent Proteins (FPs) and Bioluminescent Proteins (see Appendix A) can tag specific cells or proteins and thus can be invaluable tools for probing molecular events and pathways inside living systems [4].

In parallel with probe development, significant interest on small animal imaging is being reported [2] due to similarities between mouse development and that of other vertebrates. For this reason, mouse has a central role as a model organism for the study of the molecular genetics of mammalian development. Within the context of intact biological studies, transgenic mice models expressing fluorescent proteins in specific cell/organ types are invaluable tools for imaging biological processes. The number of transgenic animal models⁴ (see Appendix A for a list of biological relevant terms) carrying fluorescent tags in specific cells or organs is large and constantly growing [20, 21, 22].

1.1 Optical imaging

There are three major macroscopic techniques for imaging mice: Bioluminescence⁵ imaging, planar Fluorescence imaging and Optical Tomography. In Bioluminescence imaging, Luciferase is transgenically expressed in mice models as a contrast agent for in-vivo imaging. With the administration of luciferin via injection, visible light is emitted from Luciferase as the luciferin substrate is oxidized [23]. The emitted photons are recorded in photographic images by sensitive cameras in a planar geometry. Bioluminescent studies mainly involve the tracking of tumor cells [24] and the imaging of gene expression⁶ products [25]. Luciferase imaging can provide images of surface events with high signal to noise ratios. However, quantification of signals deeply seated in the body has not been yet realized using this technique (some initial methods for producing tomographic images have recently been proposed [26, 27, 28], however, bioluminescence tomography is under ongoing investigation and yet to be proven in-vivo). Furthermore the requirement of continuous delivery of the luciferin substrate to the animal compromises the need to keep the animal intact during long term experiments. Additionally, the intensity of emission and the wavelength is strongly dependent on the temperature and the pH.

In planar fluorescence imaging, fluorescent agents are administered to the animal and emit photons upon planar light exposure [29, 30, 31]. In terms of detection, planar imaging follows the same photographic principles as bioluminescence. Fluorescence imaging is a simple and high throughput technique for monitoring surface events. A variety of targeted and activatable

³the term specificity is used for describing the ability of a contrast agent to bind into a specific target molecule

⁴transgenic animal is an animal into which foreign DNA has been transferred in order to study the function of that DNA

⁵Bioluminescence is the ability of certain animals to produce light. This light is produced from conversion of chemical to radiant energy.

⁶the process by which the information in a gene is used to create proteins

probes have been used to detect tumors [32, 33] or certain transgenes⁷ [34] in mice. Green fluorescent protein is also commonly used as a contrast agent as it is proven to be an excellent marker in terms of specificity and signal strength [35]. Recent studies include tumour and metastases imaging as well as angiogenesis [31, 29, 30]. Gene expression is monitored after injection of a fluorescent probe to the region of interest. However due to the lack of multiple projections and/or several source positions, depth resolution is not feasible. Moreover, the nonlinear dependence of light over depth is not taken into account, deteriorating the ability to quantify and volumetrically image the fluorescent signals, thus restraining the technique to depths of a few millimeters under the skin. Alternatively, Diffuse Optical Tomography is the only technique that delivers volumetric and quantitative images [36, 37, 5]. In this approach, measurements at different source/detector positions are recorded. In Diffuse Optical Tomography the diffuse propagation of light⁸ inside the subject is theoretically modelled, incorporating the models of light propagation to the processing of the experimental images, so that quantitative information can be extracted [38]. Diffuse optical tomography was first developed for medical studies by delivering three dimensional maps of the scattering and/or the absorption properties of tissue [5], like oxygen saturation and blood volume.

Fluorescence Molecular Tomography (FMT) incorporates the principles of Diffuse Optical Tomography(DOT) with the use of fluorescent probes as a source of contrast [39, 40]. In FMT the subject that carries the fluorescent probe is exposed to light from different source positions and the emitted light is captured by detectors arranged in a spatially defined order. The information is then mathematically processed, resulting in a reconstructed tomographic image. Reconstruction of NIR probes were firstly explored due to higher penetration in tissue of NIR light but in recent studies tomographic images of GFP expression from deep seated locations *in vivo* have also been presented [41]. Recently, theoretical developments in modeling arbitrary shapes and diffuse light propagation in free-space [42] has led to the materialization of non-contact systems. Combining this non-contact approach with CCD-based measurements can offer high spatial sampling, leading to large data sets (compared with the old fiber-based systems) which are essential for high-quality tomographic images [43, 44]. In addition, the non-contact approach contributes to the simplification of the experimental procedure. Noncontact systems have already been implemented that incorporate the non-contact recording of the outgoing radiation [45] as well as the non-contact illumination of the subject [41]. Non-contact optical tomography has been verified by means of fluorescence measurements with phantoms [46] and controlled experiments on mice ex-vivo [45]. However, in these studies, the subject was either under compression while in contact with light delivering systems or immersed in index matching fluids to simplify boundary conditions

The main aim of the work presented in this thesis was the implementation and the de-

⁷gene from a dissimilar organism or an artificially constructed gene added by methods of molecular biology to another organism

⁸the way light is propagating in a high scattering medium such as tissue. The clouds, the milk and the foam are also high scattering media

velopment of a new non-contact, fluid/compression-free tomographic system that would fully explore the advantages of the non-contact approach. A fluorescent molecular tomographer was built that has the capacity to retrieve the distribution of fluorescent concentration inside small animals in a simple way. This tomographer was used for the in-vivo extraction of volumetric images of fluorescent concentration in intact transgenic mice expressing GFP in their T cells⁹. We chose to image organs of the immune system, such as the thymus, the spleen and the lymph nodes where T cells are residing. Although this new non-contact tomographic system is based on known tomographic principles, it implies great advances in terms of experimental simplicity. It can operate in either reflection or transmission geometry modes depending on the targeted area or organ and even scan the whole body area so that whole body tomography is feasible.

Before moving to the next chapters of this thesis, I would like to introduce the basic scheme of a noncontact tomographic imager. We will refer to this basic scheme many times not only in order to formulate the theoretical problem but also in order to experimentally implement a non contact tomographer in terms of instrumentation.

1.2 Non contact measurements

The general scheme of an ideal non-contact fluorescence imaging setup should have the geometry depicted in Figure [1.1]. As can be seen, a laser beam of wavelength λ_a illuminates a subject, propagates inside the medium and excites the residing fluorophores. Upon excitation, the fluorophores act as secondary sources and they emit light of different wavelength λ_b . A camera focused on the surface of the subject records either the fluorescence or the excitation light emerging from the boundary, depending the filter in front of the camera.

The tomographer is comprised from three main components, namely the source, the subject and the detector. The illumination source usually is a laser beam X_{inc} , in the position \mathbf{r} , pointing at the direction \mathbf{s} , t is the time dependency of the laser intensity and λ_a is the wavelength. The medium of volume V is turbid and in general an optically inhomogeneous medium which contains fluorophores whose concentration is denoted as $N_t(\mathbf{r})$. It is assumed that both the optical properties, namely the absorption and the scattering , expressed as $\mu_a(\mathbf{r})$ and $\mu'_s(\mathbf{r})$ respectively, and the fluorescent concentration remain constant or they change in a time scale much longer than the propagation of light. Excitation and emission light emerging from the surface is expressed as X_{prop} .

⁹white blood cells responsible for the body's immunity. T cells can destroy cells infected by viruses.

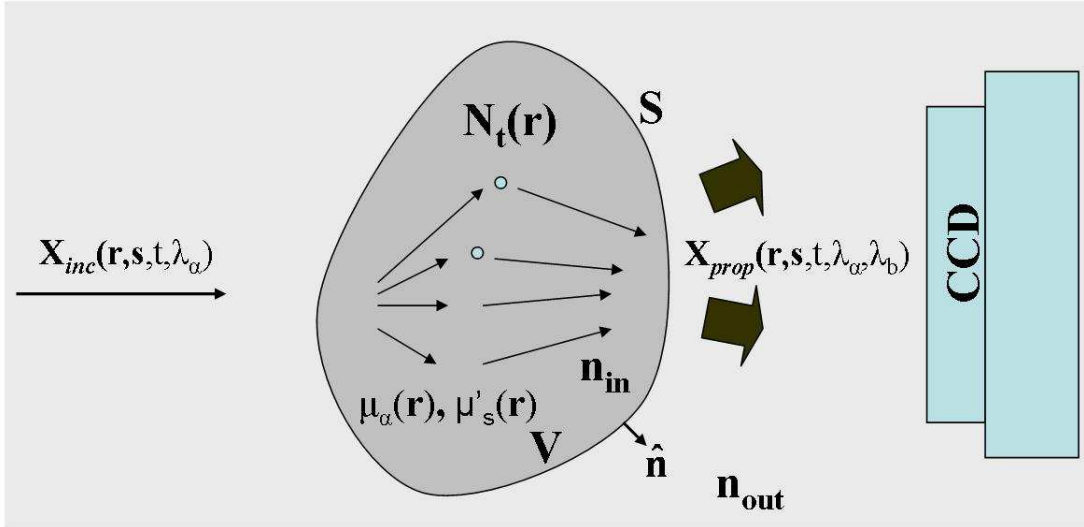


Figure 1.1: Basic experimental scheme

1.3 The forward and the inverse problem

As stated earlier, the only way to quantitatively image the distribution of the fluorescent concentration inside the subject is by performing tomography. Tomography refers to the cross-sectional imaging of an object from either transmission or reflection data collected by illuminating the object from many different directions. Fundamentally, irrespective of tomographic modality, tomographic imaging deals with reconstructing an image from its projections [47]. The term projection means the information derived from the transmitted energies, given the position of the source and the detector. The different projections which are necessary for the tomographic imaging can be captured by moving at least one of the three basic components of the setup, i.e the laser source, the target or the detecting system.

In our case we wanted to build an experimental setup that could be used to extract tomographic images of fluorescent activity inside small living systems. The problem of reconstructing the map of the fluorescent concentration, $N_t(\mathbf{r})$ from the interior of a turbid medium can be divided into two steps: the forward problem and the inverse problem. In order to formulate the two problems we will consider the geometry depicted in Figure [1.1].

The forward problem is the following:

Given the light source distribution X_{inc} and the distribution of the fluorescent concentration $N_t(\mathbf{r})$ within V , find the light at any position in the medium and consequently on the surface S , X_{prop} .

$$f[X_{inc}(\mathbf{r}, \mathbf{s}, t, \lambda_a); N_t(\mathbf{r})] \rightarrow X_{prop}(\mathbf{r}, \mathbf{s}, t, \lambda_a, \lambda_b)$$

Similarly, the inverse problem can be expressed as:

Given the distribution of light sources X_{inc} and a distribution of measurements on the surface S , X_{prop} , derive the distribution of the fluorescent concentration $N_t(\mathbf{r})$ within V .

$$f^{-1}[X_{inc}(\mathbf{r}, \mathbf{s}, t, \lambda_a); X_{prop}(\mathbf{r}, \mathbf{s}, t, \lambda_a, \lambda_b)] \rightarrow N_t(\mathbf{r})$$

Although this work was focused on reconstructing the fluorophore concentration, the above tomographic scheme is more general and can be also applied for the imaging of the scattering and/or the absorption properties distributions. The tomographic image is given by solving the inverse problem but, as we will be shown in the next chapters, one cannot solve the inverse problem without formulating a theory for the forward problem.

In this thesis the first three chapters describe the theoretical basis of extracting tomographic images from noncontact measurements. Based on the basic scheme of figure (1.1), chapter 2 describes the propagation of the excitation and the fluorescent light assuming an infinite medium. Then, in chapter 3 the contribution of the boundaries is accounted for to generate solutions for media of arbitrary geometries. We will also present a new method which has been developed for treating media with arbitrary boundaries. Chapter 4 describes the different subjects used in this work. These subjects include two types of GFP transgenic mice, i.e. hCD2-GFP transgenic mice expressing GFP in their T-cells and GFP CLIP-170 transgenic mice expressing GFP in the testis. In terms of the instrumentation, the different components of the setup that comprise our whole body tomographer are presented. Chapter 5 follows the steps of the experimental protocol for acquiring images. The method of processing the experimental images until a tomographic image is formed, is the scope of chapter 6. Chapter 7 discusses the results, where tomographic images of fluorescent activity are shown from measurements on several GFP transgenic mouse models. The quantification accuracy and the sensitivity of the system are then evaluated with data from a biologically relevant study. Final, in chapter 8, we discuss the impact of the in-vivo imaging of lymphoid organs to the study of the function of the immune system as well the ability of the tomographic technique to quantify the spermatogenesis process in the case of the CLIP-170 mouse models. Additionally, we propose how this non-contact whole body setup can be further developed and its applications expanded.

Chapter 2

Theory of diffuse light

This chapter deals with the forward problem as discussed in section (1.3). In this chapter the theory underlying the propagation of light in a scattering and absorbing medium that contains fluorophores will be presented. Biological tissue is visually opaque due to the fact that, besides absorption, there is high scattering of light. The photons from a collimated source suffer many scattering events between the particles of the medium so that light propagates in a diffuse way. Additionally, the propagation of visible light through biological tissue is governed by strong absorption. Inside tissue, photons can be scattered, absorbed or give excitation to fluorescent molecules and so they carry information by interacting with medium that they traverse.

Propagation of light in biological tissue can usually be modeled by using basically two theories; the wave theory (Maxwell's equations) and the transport theory. In wave theory, Maxwell's equations need to be solved for the substance of interest and the optical properties are defined via the dielectric constant $\epsilon(\mathbf{r})$. Although Maxwell's equations treat the problem of light propagation rigorously, in most practical systems extracting a solution is impossible due to the complexity of the problem. Theoretical research in tissue optics has been based on the Radiative Transfer Equation (RTE) [48, 7] or approximations to it where analytical solutions are easily extracted [38]. In transport theory, light is treated as energy propagating through a medium containing particles. It is assumed that there is no correlation between fields and therefore the addition of powers rather than the addition at fields holds [7]. The most common approach to the RTE is based on the diffusion approximation [7, 9] which provides simple analytical expressions (which have the form of a diffusion equation) for light transport and can be applied to a great variety of scattering systems. The absorption of tissue is related with the absorption of the major blood components like the Hemoglobin and Deoxyhemoglobin whose absorption spectra are shown in Figure (2.1). Light scattering in tissues is significantly dominant over absorption in the wavelengths between 650 and 1100nm and thus the diffusion approximation has been widely used for modelling the diffuse light of biological tissue in the near infrared (NIR) region.

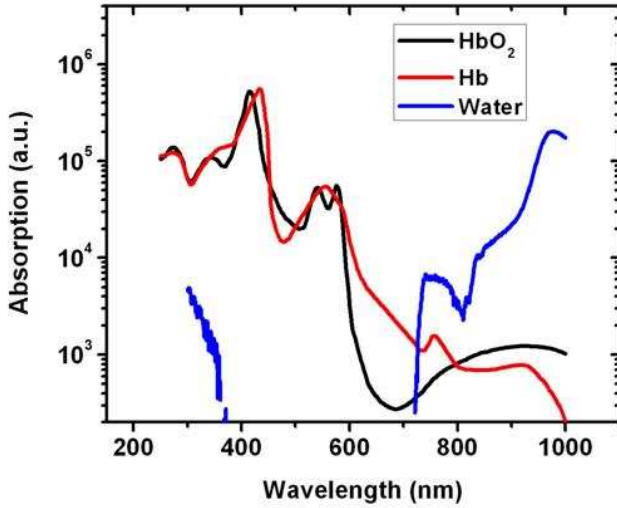


Figure 2.1: The absorption spectra of Hemoglobin and Deoxyhemoglobin

However, light is strongly absorbed in the visible wavelengths which is the case for the emission spectra of the fluorescent probes being imaged in this work. Improvements on the diffusion equation should be applied in order to expand the limits of its validity .

In this chapter, we will start with the Radiative Transfer Equation which is widely used to model light propagation in tissue like media. By introducing the diffusion approximation, the steps for deriving the diffusion equation will be then presented. We will show next a method of modelling light propagation inside scattering media exhibiting strong absorption. This is done within the context of the diffusion approximation. Then the solution for an infinite homogeneous medium will be extracted in order to model the propagation of the excitation light. Finally, since the majority of experiments presented in this thesis concern the tomographic imaging of fluorescent probes (fluorophores or fluorescent proteins) a theoretical approach will be presented for the generation and the propagation of the fluorescent light emitted by the fluorescent molecules upon excitation.

2.1 From the radiative transfer equation to the diffusion equation

Photon propagation in high scattering media is modeled with the use of the Boltzman transport equation which is also known as Radiative Transfer Equation (RTE)[7, 49].

$$\frac{n}{c} \frac{\partial I(\mathbf{r}, \hat{\mathbf{s}})}{\partial t} = -\hat{\mathbf{s}} \cdot \nabla I(\mathbf{r}, \hat{\mathbf{s}}) - \mu_t I(\mathbf{r}, \hat{\mathbf{s}}) + \frac{\mu_t}{4\pi} \int_{4\pi} p(\hat{\mathbf{s}}, \hat{\mathbf{s}'}) I(\mathbf{r}, \hat{\mathbf{s}'}) d\Omega' + \epsilon(\mathbf{r}, \hat{\mathbf{s}}) \quad (2.1)$$

In eq. [2.1], the quantitiy $I(\mathbf{r}, t)$ is called *specific intensity*. It is defined as the average power flux at the position \mathbf{r} , propagating along the unit vector $\hat{\mathbf{s}}$ and has units, $Wcm^{-2}sr^{-1}$ (sr=steradian=unit

solid angle). In eq. [2.1], μ_t is the total macroscopic cross section with units of cm^{-1} and $p(\hat{\mathbf{s}}, \hat{\mathbf{s}}')$ is the phase function that represents the probability of scattering into a direction $\hat{\mathbf{s}}'$ from a direction $\hat{\mathbf{s}}$. Finally $\epsilon(\mathbf{r}, s)$ is the spatial and angular distribution of the source. The RTE is a conservation equation for the specific Intensity inside a small volume element and in the direction \hat{s} . The first term on the right hand side describes the loss in \mathbf{r} and in the direction \hat{s} , the second term the losses due to absorption and scattering, the third term any gain due to scattering from other directions into \hat{s} and the last term the gains due to any source in \mathbf{r} .

2.1.1 Transport Properties

In this subsection, quantities presented in the RTE like the *macroscopic cross-section*, μ_t , the *phase function*, $p(\hat{\mathbf{s}}, \hat{\mathbf{s}}')$, or related to them, like the *scattering coefficient*, μ_s , the *absorption coefficient*, μ_a and the *anisotropy factor*, g are defined and discussed.

We will start with the macroscopic cross-section μ_t which is also called transport coefficient or total attenuation coefficient. The macroscopic cross-section has units of $[cm^{-1}]$ and is defined as:

$$\mu_t = \rho (\sigma_a + \sigma_s) \quad (2.2)$$

In this equation, ρ is the density of scatterers while σ_a and σ_s are the absorption and scattering cross-section respectively, measured in $[cm^2]$. The transport coefficient can be also be written as:

$$\mu_t = \mu_s + \mu_a . \quad (2.3)$$

In the above equation μ_s is the scattering coefficient. The scattering coefficient is the multiplicative inverse of the random-walk step length (which is also known as the scattering mean free path or just mean free path):

$$\mu_s = \frac{1}{l_{sc}} \quad (2.4)$$

where l_{sc} is equal to the characteristic distance between two scattering events.

Analogous to the scattering mean free path, the absorption length is defined in terms of the absorption coefficient μ_a as:

$$l_a = \frac{1}{\mu_a} . \quad (2.5)$$

The absorption length is the average distance that a photon undergoes before it is absorbed.

In the eq. (2.1) the phase function $p(\hat{\mathbf{s}}, \hat{\mathbf{s}}')$ was also presented. The phase function (which is also known as probability density function) represents the probability that a photon will scatter into a direction $\hat{\mathbf{s}}'$ from a direction $\hat{\mathbf{s}}$. The phase function holds the following relationship:

$$\frac{1}{4\pi} \int_{4\pi} p(\hat{\mathbf{s}}, \hat{\mathbf{s}}) d\Omega = \frac{\mu_s}{\mu_t} = W_0, \quad (2.6)$$

where W_0 is called albedo and which represents the “the whiteness” of a particle, i.e. its capability to scatter light. In biological tissues it is a common approach to assume that the phase function depends only on the angle between $\hat{\mathbf{s}}$ and $\hat{\mathbf{s}'}$, i.e. $p(\hat{\mathbf{s}}, \hat{\mathbf{s}'}) = p(\hat{\mathbf{s}} \cdot \hat{\mathbf{s}'}) = p(\cos \theta)$ and is often being approximated by the following form:

$$p(\cos \theta) = \frac{W_0(1-g^2)}{(1+g^2-2g \cos \theta)^{3/2}}. \quad (2.7)$$

The above equation is the well-known Henyey-Greenstein formula [50], and constitutes the most commonly used approximation for the phase function in biological media. In the eq. (2.7), g is the average cosine of the scattering angle and it is defined in terms of the phase function as:

$$g = \langle \cos \theta \rangle = \frac{\int_{4\pi} p(\hat{\mathbf{s}} \cdot \hat{\mathbf{s}'}) \hat{\mathbf{s}} \cdot \hat{\mathbf{s}'} d\Omega'}{\int_{4\pi} p(\hat{\mathbf{s}} \cdot \hat{\mathbf{s}'}) d\Omega'}. \quad (2.8)$$

According to its definition, g is a quantity which express the anisotropy of the scattered light after interacting with the particle and, as such, is called the anisotropy factor.

2.1.2 Flux conservation

If we now integrate over all 4π of solid angle in the RTE(eq.[2.1]) we will obtain:

$$\frac{1}{c} \frac{\partial}{\partial t} \int_{4\pi} I(\mathbf{r}, \hat{\mathbf{s}}) d\Omega = -\nabla \cdot \int_{4\pi} I(\mathbf{r}, \hat{\mathbf{s}}) \hat{\mathbf{s}} d\Omega - \mu_a \int_{4\pi} I(\mathbf{r}, \hat{\mathbf{s}}) d\Omega + \int_{4\pi} \epsilon(\mathbf{r}, \hat{\mathbf{s}}) d\Omega. \quad (2.9)$$

In eq. [2.9] we can recognise some interesting radiometric quantities: *the average Intensity* U and *total flux density* \mathbf{J} which are defined in terms of the specific Intensity as:

$$U(\mathbf{r}) = \int_{4\pi} I(\mathbf{r}, \hat{\mathbf{s}}) d\Omega \quad (2.10)$$

$$\mathbf{J}(\mathbf{r}) = \int_{4\pi} I(\mathbf{r}, \hat{\mathbf{s}}) \hat{\mathbf{s}} d\Omega. \quad (2.11)$$

Both the *the average Intensity* U and *total flux density* \mathbf{J} have units $[W/cm^2]$.

Inserting the quantities $U(\mathbf{r})$ and $\mathbf{J}(\mathbf{r})$ into the eq. (2.9), we obtain the following equation which is the equation of flux conservation:

$$\frac{1}{c} \frac{\partial U(\mathbf{r})}{\partial t} + \nabla \cdot \mathbf{J}(\mathbf{r}) + \mu_a U(r) = E(\mathbf{r}) \quad (2.12)$$

In eq. (2.12) we define:

$$E(\mathbf{r}) = \int_{4\pi} \epsilon(\mathbf{r}, \hat{\mathbf{s}}) d\Omega \quad (2.13)$$

measured in $[Wcm^{-1}]$, as the power generated per unit volume.

2.1.3 Diffusion Approximation

The RTE, being an integro-differential equation, cannot deliver simple solutions. Analytic solutions of the transport equation exist only for very simple geometries and numerical calculations require large amounts of computational power. Instead of attempting a full solution various methods based on simplifications or approximations to RTE are available. The most widely applied approximation is the diffusion approximation [8]. In the diffusion approximation, which is also known as the **P1** approximation, the specific intensity I at point \mathbf{r} flowing in direction $\hat{\mathbf{s}}$, is expanded in a series of spherical harmonics. If this expansion is truncated at the first term, this consists the **P1** approximation:

$$I(\mathbf{r}, \hat{\mathbf{s}}, t) \simeq \frac{1}{4\pi} U_t(\mathbf{r}, t) + \frac{3}{4\pi} \mathbf{J}_t(\mathbf{r}, t) \cdot \hat{\mathbf{s}} \quad (2.14)$$

where U_t is the time dependent average intensity, and \mathbf{J}_t represents the flux.

This approximation reduces Eq. (2.1) into simpler equations where analytical expressions can be derived. The diffusion approximation assumes that the intensity inside the scattering medium can be considered diffusive which means that the photons have undergone multiple scattering events and the light is considered highly incoherent. This is actually the case in a medium, when the scattering coefficient is much greater than the absorption coefficient, the phase function is not too anisotropic and we are away from light sources and boundaries. The diffusion approximation can be used to describe the propagation of NIR photons inside biological tissue since at the wavelength range between 650 and 1100 nm scattering is much greater than absorption. However, care should be taken when applying it in the region of visible light. A way to treat visible light within the context of the diffusion approximation will be presented in section (2.3).

If we substitute eq. (2.14) into eq. (2.1), multiply by $\hat{\mathbf{s}}$ and integrate over 4π we obtain:

$$\nabla U(\mathbf{r}) = -3(\mu'_s + \mu_a) \mathbf{J}(\mathbf{r}) - 3\frac{n}{c} \frac{\partial \mathbf{J}(\mathbf{r})}{\partial t} + \int \epsilon(\mathbf{r}, \hat{\mathbf{s}}) \hat{\mathbf{s}} d\Omega \quad (2.15)$$

The eq. [2.15] can be also written as:

$$\nabla U_t(\mathbf{r}, t) = -3\mu'_s \left[\frac{n_0}{c\mu'_s} \left(\frac{\partial}{\partial t} + \frac{c\mu_a}{n_0} \right) + 1 \right] \mathbf{J}_t(\mathbf{r}, t) + \int \epsilon(\mathbf{r}, \hat{\mathbf{s}}) \hat{\mathbf{s}} d\Omega \quad (2.16)$$

In eqs. (2.15) and (2.16), μ'_s is the reduced scattering coefficient, defined as:

$$\mu'_s = \mu_s \cdot (1 - g) . \quad (2.17)$$

In terms of μ'_s , we shall define the transport mean free path l_{tr} :

$$l_{tr} = \frac{1}{\mu'_s} = \frac{l_{sc}}{1 - g}. \quad (2.18)$$

which includes the anisotropy factor g .

The reduced scattering coefficient takes into account the anisotropy of the scattering. We will focus now on the meaning of the transport mean free path by assuming two limiting cases, when the scattering is fully isotropic and when the scattering is fully anisotropic. The first case means $g = 0$ and then from eq.[2.18] we have $l_{tr} = l_{sc}$. This means that the radiation can be scattered to any direction after travelling one scattering mean free path. On the other hand if the scattering is highly anisotropic then $g \sim 1$ and $l_{tr} \sim \infty$. This means that radiation is travelling large distances without changing its direction. Therefore, the transport mean free path ($1/\mu'_s$) can be understood as the average distance that a photon travels before its propagation direction is completely randomized by a series of scattering events. In other words, $1/\mu'_s$ defines a distance where the scattering can be regarded as isotropic.

The reduced scattering coefficient and the absorption coefficient express the inherent properties of the tissue and were firstly used for tissue imaging since there are cases that their value is correlated with the pathology of the tissue [51, 52]. The magnitude of μ'_s in a tissue is determined in part by the concentration of micron-sized optical heterogeneities, such as the cell organelles [10, 53] while the absorption coefficient μ_a depends on the concentration and absorption cross-section of various chromophores, such as the hemoglobin that resides in blood vessels [6].

2.1.4 Fick's Law

As presented in the previous section, if Eq. [2.14] is introduced in the time-dependent expression for the Radiative Transfer Equation, one finally reaches the following expression for an isotropic source in a medium with absorption coefficient μ_a , reduced scattering coefficient μ'_s and index of refraction n_0 :

$$\nabla U_t(\mathbf{r}, t) = -3\mu'_s \left[\frac{n_0}{c\mu'_s} \left(\frac{\partial}{\partial t} + \frac{c\mu_a}{n_0} \right) + 1 \right] \mathbf{J}_t(\mathbf{r}, t) \quad (2.19)$$

In eq. [2.16] we find two characteristic times:

$$t_{tr} = \frac{n_0}{c\mu'_s} = \frac{n_0}{c} l_{tr} \quad (2.20)$$

being the average time required for \mathbf{J} to travel one transport mean free path distance, and

$$t_a = \frac{n_0}{c\mu_a} \quad (2.21)$$

being the characteristic time of flux \mathbf{J} to change due to absorption. For the case of a continuous wave light source Eq. [2.16] is reduced to:

$$\mathbf{J}(\mathbf{r}) = -\frac{1}{3(\mu'_s + \mu_a)} \nabla U(\mathbf{r}) . \quad (2.22)$$

which is Fick's law for the diffusion of the average intensity.

2.2 The Diffusion Equation

There are several variations of the diffusion equation depending on the approximations taken through its derivation, as can be seen from the analysis in section (2.1.4). The limits of validity of the different diffusion equations have been studied in different publications [54, 8] and there is no consensus on what is the best expression. In this section we will derive a widely used form of the diffusion equation.

When inserting the function for the flux \mathbf{J} from the Eq. [2.22] into the equation of the flux conservation (Eq. [2.12]), we obtain a differential equation for the average Intensity U :

$$\frac{n}{c} \frac{\partial U(\mathbf{r}, t)}{\partial t} + \nabla[D \nabla U(\mathbf{r}, t)] + \mu_a U(\mathbf{r}, t) = E(\mathbf{r}, t) \quad (2.23)$$

with the following diffusion coefficient:

$$D = \frac{1}{3(\mu'_s + \mu_a)} . \quad (2.24)$$

This equation was presented in ref. [8], and is one of the most commonly used expressions. We should also say at this point, that in our analysis so far we assumed a homogeneous medium, meaning that both μ_s and μ_a are constant throughout the medium. This assumption seems exaggerated when referring to such a complex and anisotropic medium as the biological tissue. However the diffusion approximation has been extensively tested against tissue experiments and accurately predicts light propagation inside tissue even when assuming constant optical properties [9].

2.3 High absorbing media

Theoretical studies in describing the propagation of light were stimulated by the initial experimental observations that NIR light is travelling the tissue and thus optical imaging techniques can be developed. The majority of the theoretical works were based on the diffusion approximation to provide a simple and analytical expression for describing the propagation of NIR light inside the tissue [8]. One of the major assumptions when introducing the diffusion approximation is that the scattering is much stronger than the absorption. According to Figure (2.21),

this is the case for the spectral region between the 650 and 1100nm where the absorption is low and the scattering is the primary interaction between light and tissue.

Recently, the Green Fluorescent Protein(GFP) and its derivatives have been proposed as excellent probes, in terms of brightness and specificity, for molecular imaging studies. The GFP molecule as well as other commonly used fluorescent proteins have their excitation and emission peaks in the visible spectrum (see figure[2.2]) where the scattering becomes comparable to the absorption ($\mu'_s \simeq \mu_a$).

This means that we have to reconsider the theory developed for the high scattering regime, in order to model the propagation of the light that excites the fluorescent probes as well as the propagation of the fluorescent light that is emitted.

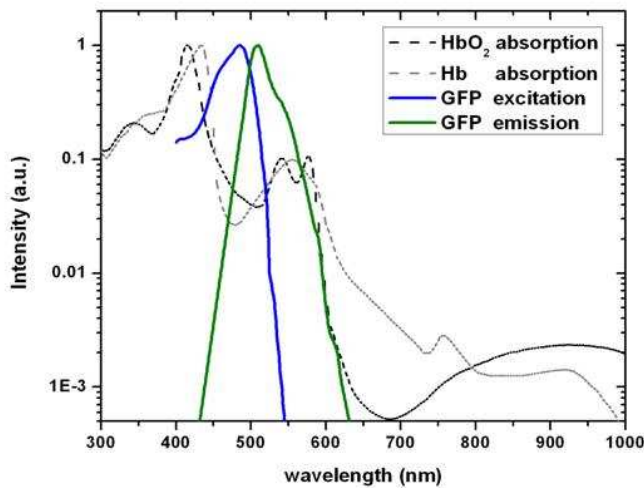


Figure 2.2: The excitation and emission spectra of the GFP molecule, against the absorption spectra of two main blood components

Many research papers are devoted to explore the range of validity of the diffusion approximation [55, 56, 57, 58, 59, 60, 61, 62, 63, 64, 65, 66, 67]. When dealing with strong absorbing media, the measured intensities strongly deviate from the ones predicted by the standard diffusion equation. This has been attributed to a failure of the diffusion approximation and it is believed that the diffusion approximation furnishes accurate results only for high scattering over absorption differences, where light has suffered multiple scattering events and can thus be treated as diffusive [60]. Some researchers, however, have proposed the use diffusion approximation after expanding its limits of validity in order to cover the strong absorption regime. Their approaches have been focused on the diffusion coefficient and the role of absorption coefficient μ_a in it. The dependence of the diffusion coefficient with absorption is used to be a controversial issue and many studies have been published dealing with the expression of the diffusion coefficient [65, 66, 67, 68, 69, 70]. Within this work we shall use the formula presented in Ref. [65], in which a modified form of the diffusion coefficient is used. This solution applies a modified diffusion coefficient with a weighted dependence on the absorption coefficient [71, 72].

This solution has been experimentally tested and has been shown to describe the propagation of light in highly absorbing media in in-vivo studies [41].

2.3.1 The diffusion coefficient in high absorbing media

This subsection is based mainly on studies by *Aronson et al* [72] and *Ripoll et al* [71]. In the former study, an absorption dependent expression for the diffusion coefficient was presented, while in the latter, the validity of this expression was studied experimentally. The reader is referred to those studies for a detailed analysis of their approaches.

In order to derive an equation capable of managing the propagation in high absorbing media we follow a simple analysis. Instead of solving the radiative transfer equation and account for the strong absorption, we will expand the limits of validity of the diffusion approximation. The basic idea of the approach is to account for the strong absorption but within the context of the diffusion approximation. We will focus on modifying the diffusion coefficient in order to describe the propagation of light in the strong absorbing regime.

Following Ref. [25], a useful way to represent the absorption dependence is by writing the diffusion coefficient as:

$$D = \frac{1}{3(\mu'_s + a\mu_a)} \quad (2.25)$$

where a will generally depend on the absorption, scattering and anisotropy of the medium. In terms of the scattering coefficient μ_s , we recall that the reduced scattering coefficient is written as $\mu'_s = (1 - g)\mu_s$.

Let us now assume that a continuous source of photons is applied on the source term of eq.[2.23]. The exact solution of the diffusion equation for a continuous source will be derived in the next section, however we present here the form of the solution for the average Intensity, U :

$$U(\mathbf{r}) \sim \exp\left(-\frac{\mathbf{r}}{L_d}\right). \quad (2.26)$$

In eq.[2.34], the quantity L_d is the *diffusion length*. The diffusion length is the distance at which the average Intensity decreases by a factor of e . In the next section we will show that the diffusion length L_d is defined as:

$$L_d = \sqrt{D/\mu_a}. \quad (2.27)$$

We notice that Eq. [2.27] defines the diffusion coefficient in terms of the diffusion length, as $D = L_d^2\mu_a$ and thus has the form of a dispersion relation. Several studies exist that calculate a dispersion relation for the L_d . We consider the anisotropic scattering ($g > 0$) which is the case for tissue (typical values of g in tissue range from $g = 0.7$ to $g = 0.95$). For anisotropic scattering, an expression for the dispersion can be found in ref.[73]. This expression will not be presented here for the sake of clarity.

If we expand the dispersion equation calculated in ref. [73] and we neglect the orders equal

or higher to two then we will find a diffusion coefficient that has the following form:

$$D = \frac{1}{3(\mu'_s + \mu_a)} \left[1 - \frac{4}{5} \frac{\mu_a}{\mu'_s(1+g) + \mu_a} \right]^{-1}. \quad (2.28)$$

from Eq. [2.28] we see that the diffusion coefficient depends nonlinearly on the scattering and the absorption properties of the medium. By comparing the Eq.[2.25] with Eq.[2.28] we find the expression for the a :

$$a = 1 - \frac{4}{5} \frac{\mu'_s + \mu_a}{\mu'_s(1+g) + \mu_a}. \quad (2.29)$$

The deviation in the value of a when considering higher-order contributions in the derivation of D is less than 2% [71]. Typical values of a range from 0.2 to 0.6, being of the order of 0.5 – 0.55 in the case of tissue in the visible, assuming an anisotropy factor of $g \sim 0.8$. In ref. [71] optical characterization measurements were performed on highly absorbing tissue-like phantoms, whose absorption coefficient varied in a controlled way. The modified expression for the diffusion coefficient was used in order to reconstruct the optical properties of the samples and was used to model the propagation of light inside the samples, retrieving the absorption coefficient with great accuracy. In contrast, the other variations of the diffusion coefficient, namely for $a = 1$ or $a = 0$, yielded inaccurate results. For the rest of the analysis presented in this thesis we will adopt the expression of the diffusion coefficient given by the eq.[2.25] with a being given by the eq.[2.29], always among $g = 0.8$.

2.4 Solutions of the diffusion equation for infinite homogeneous media

Although the object of the figure (1.1) is bounded by a surface, it is useful to find first the solution for the case of an infinite medium. The contribution of the boundaries will be accounted for by using the Green's theorem, as we will see in the next chapter. The Diffusion equation that we will adopt for the rest of the thesis and which we will referred to as the standard diffusion equation is given by:

$$\frac{1}{c} \frac{\partial U(\mathbf{r}, t)}{\partial t} - D \nabla^2 U(\mathbf{r}, t) + \mu_a U(\mathbf{r}, t) = E(\mathbf{r}, t). \quad (2.30)$$

This standard duffusion equation can be transformed into a Helmholtz equation by decomposing $\frac{\partial U}{\partial t}$ into frequencies.

Looking at the basic scheme of figure [1.1], we see that there are two sources of light i.e. the laser source of wavelength λ_a that illuminates the medium and the fluorescent molecules that emit light of wavelength λ_b when excited by the diffuse excitation light. We will first find an expression for the propagation of the excitation light by applying the excitation source term on the Eq. [2.30]. Then we will use the derived expression to define the fluorescent source term

and apply it in an analogous way to the diffusion equation in order to derive the propagation of the fluorescent light.

2.4.1 The excitation source term: the Continuous Wave (CW) laser source

The form of the Hemholtz equation depends on the light source used for the excitation of the fluorescent molecules. Let us consider a continuous wave(cw) laser source irradiating the object of Figure [1.1]. A common way of defining the source within a scattering medium is to consider a point source located at $z \sim l_{tr}$ (where l_{tr} transport mean free path) inside the medium. This approach to the source term may seem like an overly simplistic approximation but it has been shown to provide very good results even for small source/detector distances[74] in phantom and in-vivo experiments [5, 8, 39, 75]. This delta function implies isotropic emission of light and the source term of the Eq.(2.30) can be written as:

$$E(\mathbf{r}, t) \rightarrow S_0\delta(\mathbf{r}) \quad (2.31)$$

where S_0 is the source strength. If we use the Eq.[2.31] as the source term in eq.[2.30] the diffusion equation of the average Intensity obeys the following equation, which has the form of a modified Helmholtz equation:

$$\nabla^2 U(\mathbf{r}) + \kappa_0^2 U(\mathbf{r}) = -\frac{S_0\delta(\mathbf{r})}{D} \quad (2.32)$$

where κ_0 is the wavenumber:

$$\kappa_0 = i\sqrt{\frac{\mu_a}{D}}. \quad (2.33)$$

With the aid of Eq.[2.41] the diffusion length L_d is defined as:

$$L_d = \sqrt{\frac{D}{\mu_a}}. \quad (2.34)$$

We recall that, in the previous section the diffusion length was used to define the diffusion coefficient: $D = L_d^2\mu_a$.

The Helmholtz equation can be solved with the use of Green's functions. With respect to the eq.[2.32], the corresponding equation for the Green's function is written as:

$$\nabla^2 G(\kappa |\mathbf{r} - \mathbf{r}_s|) + \kappa_0^2 G(\kappa |\mathbf{r} - \mathbf{r}_s|) = -4\pi\delta(\mathbf{r} - \mathbf{r}_s) \quad (2.35)$$

and the solution to it, is [76]:

$$G(\kappa |\mathbf{r} - \mathbf{r}_s|) = \frac{\exp(i\kappa_0 |\mathbf{r} - \mathbf{r}_s|)}{|\mathbf{r} - \mathbf{r}_s|}.$$

Therefore, for the case of a point source, the distribution of the average Intensity in an infinite homogeneous medium is given as:

$$U(\mathbf{r}) = \frac{S_0}{4\pi D} \frac{\exp(i\kappa_0 |\mathbf{r} - \mathbf{r}_s|)}{|\mathbf{r} - \mathbf{r}_s|} \quad (2.36)$$

where S_0 is the source amplitude and D is the diffusion coefficient of the turbid medium. Substituting the κ_0 of eq.[2.41] to the eq.[2.36] we obtain:

$$U(\mathbf{r}) = \frac{S_0}{4\pi D} \frac{\exp(-\kappa |\mathbf{r} - \mathbf{r}_s|)}{|\mathbf{r} - \mathbf{r}_s|} \quad (2.37)$$

where $\kappa = \sqrt{\frac{\mu_a}{D}}$.

If we consider the more general case of a source term that has a spatial distribution $E(\mathbf{r}, t) \rightarrow S(\mathbf{r})$ then the solution of the diffusion equation gives:

$$U(\mathbf{r}) = \frac{1}{4\pi D} \int_V \frac{S(\mathbf{r}) \exp(i\kappa_0 |\mathbf{r} - \mathbf{r}_s|)}{|\mathbf{r} - \mathbf{r}_s|} dV.$$

2.4.1.1 Time dependent illumination sources

Although a continuous wave laser was used for the experiments of this work, we would like to present some alternative illumination schemes for optical imaging studies. This section introduces the reader to the concept of the Diffuse Photon Density Waves that played an improtant role in the devolepment of the optical imaging techniques in the previous decade [77, 78].

When the source of photons in a scattering medium is intensity modulated then the photon fluence inside the medium will oscillate at the same frequency. These scalar-damped traveling disturbances of light energy propagation that are created are called Diffuse Photon Density Waves (DPDW). Microscopically, individual photons undergo a random walk within the medium, but collectively, a spherical wave of photon density is produced and propagates outward from the source. The DPDW are characterized by a well defined wavelength, group velocity and decay length and have widely used for medical imaging studies based on the inherent contrast of the tissue [79, 80]. The theory of DPDW is presented below together with their special characteristics.

As it was mentioned before DPDW are driven by an oscillating source inside the turbid medium. Let us assume that the source term is intensity modulated at a frequency ω :

$$E(\mathbf{r}, t) = S_0(\mathbf{r}) + S_0(\mathbf{r}) \exp[-i\omega t] \quad (2.38)$$

If we apply Eq.[2.38] as the source term in Eq.[2.30] we expect the solution to be written as:

$$U(\mathbf{r}, t) = U_{DC}(\mathbf{r}) + U_{AC}(\mathbf{r}) \exp[-i\omega t] \quad (2.39)$$

We will solve the problem by concerning only the time-dependent part. The diffusion equation of the frequency dependent component obeys the well known Helmholtz equation:

$$\nabla^2 U_{AC}(\mathbf{r}) + \kappa_0^2(\mathbf{r}) U_{AC}(\mathbf{r}) = -\frac{S_0(\mathbf{r})}{D(\mathbf{r})} \quad (2.40)$$

where κ_0 is a complex wavenumber:

$$\kappa_0(\mathbf{r}) = \sqrt{-\frac{\mu_a(\mathbf{r})}{D(\mathbf{r})} + i \frac{\omega n}{c D(\mathbf{r})}}. \quad (2.41)$$

As can be seen from the eq. (2.41), κ_0 is frequency dependent.

2.4.2 The fluorescent source term

Let us assume the case of a biological medium that contains a distribution of fluorescent probes and is illuminated with a laser light of wavelength λ_a , that is close to the excitation peak of the fluorophores. The incident light will propagate inside the tissue in a diffuse way and will excite the fluorescent molecules which will emit photons of a different wavelength λ_b . The fluorescent photons will travel in a diffuse way inside the medium. In order to model the propagation of the fluorescent photons, we will solve the eq. [2.30] by applying to it the expression for the fluorescent source term.

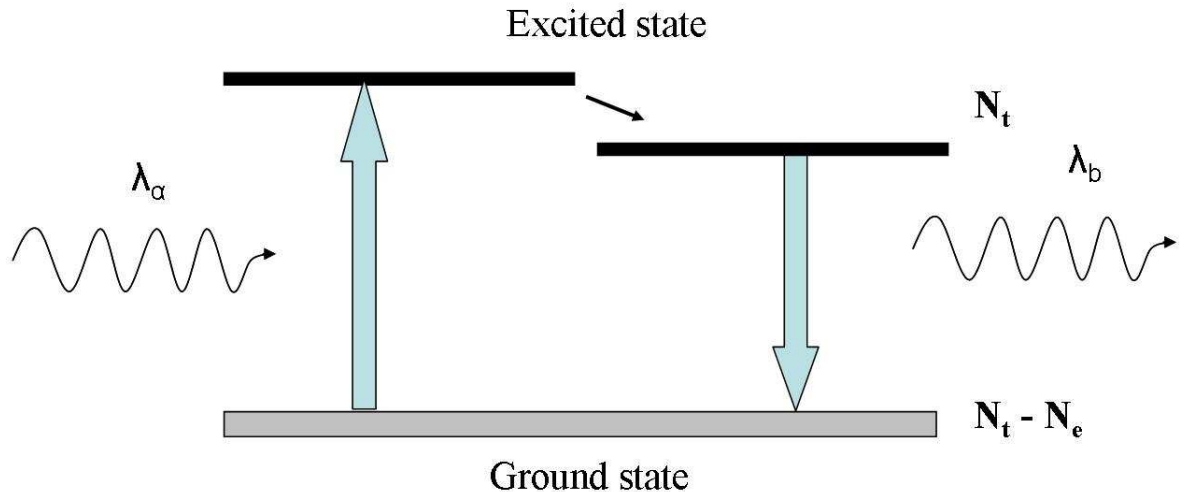


Figure 2.3: Two-level model for the fluorescence of the GFP.

The fluorophores act as secondary source of fluorescent light upon excitation by the incident laser light. In order to express the fluorescent source term, we approximate the fluorophores as two-level systems and we also assume that the medium has no gain (figure [2.3]). Although this approximation seems simplistic for modeling the molecular fluorescence however it offers simple expressions for deriving the fluorescence term and it is commonly used for tomographic imaging studies implying fluorescence molecules. The number of excited molecules per unit volume is given by the rate equation.

$$\frac{\partial N_e(\mathbf{r}, t)}{\partial t} = -\Gamma N_e(\mathbf{r}, t) + \sigma^{fluo} U^{exc}(\mathbf{r}, t)[N_t(\mathbf{r}, t) - 2N_e(\mathbf{r}, t)], \quad (2.42)$$

where $N_e(\mathbf{r}, t)$ is the number density of fluorescent molecules in the excited state at position \mathbf{r} and time t , $N_t(\mathbf{r}, t)$ is the total number density of the fluorescent molecules (the sum of excited and ground state molecules), σ^{fluo} is the absorption cross section of the molecule at the excitation wavelength λ_a , $U^{exc}(\mathbf{r}, t)$ is the excitation average Intensity and Γ is the total decay rate from the excited state to the ground state.

For a cw excitation source (eq.[2.37]), which is the case of our laser system we reach a steady state ($\frac{\partial N_e}{\partial t} = 0$) and the number of fluorescent photons emitted per unit volume becomes:

$$N_e(\mathbf{r}, \mathbf{r}_s) = \frac{\sigma^{fluo} N_t(\mathbf{r}, \mathbf{r}_s)}{\Gamma + 2\sigma^{fluo} U^{exc}(\mathbf{r}, \mathbf{r}_s)} U^{exc}(\mathbf{r}, \mathbf{r}_s). \quad (2.43)$$

Typical values of the absorption cross section are in the order of $10^{-6} cm^2$. The fluorescent lifetime for the fluorophores used is in the order of nanoseconds, so $\Gamma \sim 10^9$. For Intensities in the order of $\sim \frac{mW}{cm^2}$, which is the case for the intensities used in our experiments, $\Gamma \gg 2\sigma^{fluo} U^{exc}(\mathbf{r}, \mathbf{r}_s)$, and eq.[2.43] becomes:

$$N_e(\mathbf{r}, \mathbf{r}_s) \simeq \frac{\sigma^{fluo} N_t(\mathbf{r}, \mathbf{r}_s)}{\Gamma} U^{exc}(\mathbf{r}, \mathbf{r}_s). \quad (2.44)$$

The source term of the fluorescent light which represents the number fluorescent photons emitted per unit volume per second is thus

$$S^{fluo}(\mathbf{r}, \mathbf{r}_s) = \Gamma \eta N_e(\mathbf{r}, \mathbf{r}_s) = \eta \sigma^{fluo} N_t(\mathbf{r}, \mathbf{r}_s) U^{exc}(\mathbf{r}, \mathbf{r}_s) \quad (2.45)$$

where η is the fluorescence quantum yield.

2.4.2.1 The Born approximation

In order to get an expression for the source of the fluorescent light emerging from all the fluorophores inside the volume we will make the following approximation. We will assume first order only scattering interaction between the excitation intensity and the source of fluorescence, and we will treat the fluorophores as absorbers with σ^{fluo} being the absorption cross section of the fluorophore. In the Born expansion we write the intensity that excites the molecules as a

sum of the incident Intensity, i.e. the intensity that is present in the absence of the fluorophore and the scattered Intensity, $U^{sc}(\mathbf{r}, \mathbf{r}_s)$ that reaches the molecule after being scattered by other absorbers (see figure[2.4]).

$$U^{exc}(\mathbf{r}, \mathbf{r}_s) = U^{inc}(\mathbf{r}, \mathbf{r}_s) + U^{sc}(\mathbf{r}, \mathbf{r}_s). \quad (2.46)$$

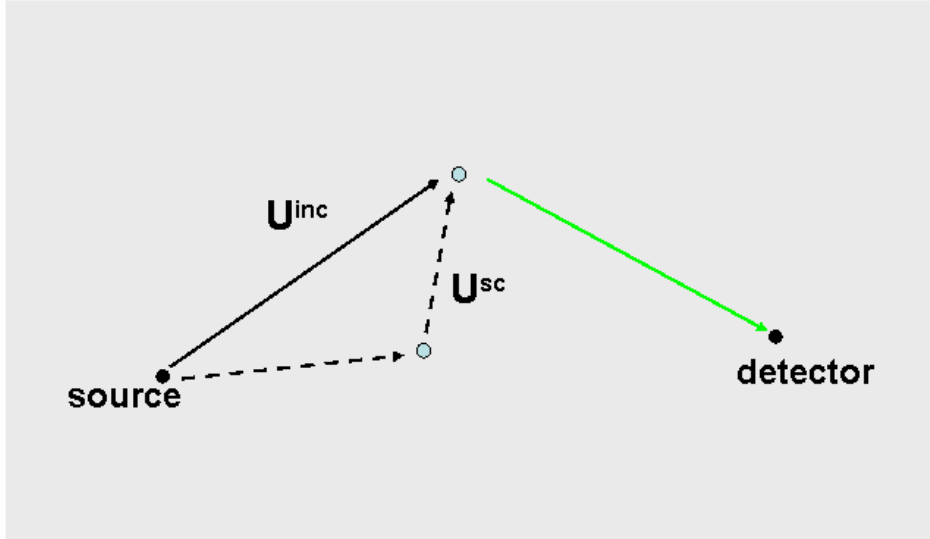


Figure 2.4: Representation of the fluorescent light generated upon excitation in medium containing fluorophores. The black line shows the excitation of the fluorophore by the excitation light. The dashed line shows the excitation of the fluorophore by the scattered light in the presence of surrounding absorbers. The green line shows the fluorescent light reaching the detector

In the Born approximation, we do not consider the non-linear effect that the presence of the other absorbers creates on the excitation Intensity: we assume that the average Intensity incident on the fluorophore is the same as in the absence of fluorescent and absorbing sources.

$$U^{exc}(\mathbf{r}, \mathbf{r}_s) \simeq U^{inc}(\mathbf{r}, \mathbf{r}_s) \quad (2.47)$$

This approximation is valid for a weakly absorbing spatial distribution of absorbers and has been used successfully in biologic media hosting fluorescent molecules.

2.4.2.2 Propagation of fluorescent light

A continuous wave point source with an optical wavelength that falls within the absorption band of the fluorescent molecule, creates an excitation light distribution which excites the fluorescent molecule. The fluorescent photons then add to create a fluorescent field originating from the source fluorescent distribution. The fluorescent radiation is assumed to be well separated in energy from that of incident photons so that we safely ignore the possibility of the excitation of the fluorescent molecules by the fluorescent re-emission.

The propagation of the fluorescent light is given by the diffusion equation (eq.[2.30]) for the fluorescent wavelength λ_b , assuming a weakly absorbing spatial distribution of fluorophores(see section(2.4.2.1)).The propagation of the fluorescent light may be determined by integration over the contributions from all fluorophores [81]:

$$U^{fluo}(\mathbf{r}) = \frac{\sigma^{fluo}\eta}{4\pi D_b} \int_V N_t(\mathbf{r}) U^{inc}(\mathbf{r}_1, \mathbf{r}_s) \frac{\exp(-\kappa_b |\mathbf{r} - \mathbf{r}_1|)}{|\mathbf{r} - \mathbf{r}_1|} dV_1, \quad (2.48)$$

where $\kappa_b = \sqrt{\frac{\mu_a(\lambda_b)}{D(\lambda_b)}}$.

It would be useful to write the general solution solution for the fluorescence propagation in terms of the Green's function according to the analysis of section (2.4.1):

$$U^{fluo}(\mathbf{r}) = \frac{\sigma^{fluo}\eta}{4\pi D_b} \int_V N_t(\mathbf{r}) U^{inc}(\mathbf{r}_1, \mathbf{r}_s) g(\kappa_{0b} |\mathbf{r} - \mathbf{r}_1|) dV_1. \quad (2.49)$$

with $\kappa_{0b} = i\kappa_b$. Finally, by applying the eq.[2.37] to eq.[2.48] we obtain:

$$U^{fluo}(\mathbf{r}) = \frac{\sigma^{fluo}\eta S_0}{16\pi^2 D_b D_a} \int_V \frac{\exp(-\kappa_a |\mathbf{r}_1 - \mathbf{r}_s|)}{|\mathbf{r}_1 - \mathbf{r}_s|} N_t(\mathbf{r}_1) \frac{\exp(-\kappa_b |\mathbf{r} - \mathbf{r}_1|)}{|\mathbf{r} - \mathbf{r}_1|} dV_1. \quad (2.50)$$

We notice that the fluorescent field is a superposition of two fields with different wavenumbers: one has the wavenumber at the excitation wavelength $\kappa_a = \sqrt{\frac{\mu_a(\lambda_a)}{D(\lambda_a)}}$ at the excitation wavelength λ_a and the other has the wavenumber κ_b at the fluorescence (emission) wavelength λ_b . In eq. [2.50] , $N_t(\mathbf{r}_1)$ gives the spatial distribution of the density of the fluorescent molecules and thus is the quantity whose reconstruction is the result of the tomographic imaging.

Eq.[2.50] can be written in a more general form, in terms of the Green's functions:

$$U^{fluo}(\mathbf{r}) = \frac{\sigma^{fluo}\eta S_0}{16\pi^2 D_{fluo} D_{exc}} \int_V g_{exc}(\mathbf{r}_1, \mathbf{r}_s) N_t(\mathbf{r}_1) g_{fluo}(\mathbf{r}, \mathbf{r}_1) dV_1. \quad (2.51)$$

where the subscripts a and b where replaced with the exc and $fluo$ respectively, in order to denote for the propagation of the excitation and the fluorescent light.

Chapter 3

Solutions for bounded media

As we saw in section 1.3, the forward problem consists of computing the solutions of a propagation model for light, given the geometry of the tomographic scheme. In the previous chapter, the forward problem was solved for the case of an infinite biological medium. We derived an expression for the propagation of light emitted by the fluorophores residing inside the subject. However, the surface of the subject has in general an arbitrary shape as implied in figure(1.1). To derive the expressions for the light that correspond to the real situation we need to account for the contribution of the surface to the light propagation for a subject that has a finite volume.

In the first section of this chapter the expression for the light distribution at any position inside media of arbitrary geometry will be derived. Given that the camera is at a distance from the surface of the medium, the light at the boundary need to be correlated with the camera images. Thus to complete the forward problem, the propagation of light from the surface of the medium to the camera should be modelled and the theoretical model for predicting the camera images given the light intensity at the surface will be presented. This consists of modelling the free space propagation of diffuse light emerging from the medium surface and reaching the CCD camera. Theoretical studies of the propagation of light emerging from a diffuse medium have driven the instrumentation of non contact tomographic systems. Finally, a means of transforming data from a medium of arbitrary shape into data that would have been obtained from an infinite medium will be presented. The information provided by the camera measurements at the surface is used to effectively transform any bounded medium into infinite. This theoretical approach greatly simplifies the forward problem since the contribution of the boundary is cancelled from the calculations.

3.1 The diffusion approximation in arbitrary geometries

We will adopt the results from the study presented in ref.[82] for modelling the light inside a diffuse medium of arbitrary shape by using the Green's theorem [83]. Let us consider the geometry depicted in Fig. (1.1) where we have a homogeneous diffusive volume V with diffusion coefficient D , absorption coefficient μ_a and index of refraction n_{in} . Taking into account

rigorously the effect of the interface S , the average intensity $U(\mathbf{r})$ generated by a light source $S(\mathbf{r})$, inside volume V is expressed through Green's theorem as:

$$U(\mathbf{r}) = U^{(inc)}(\mathbf{r}) - \frac{1}{4\pi} \int_s \left[U(\mathbf{r}') \frac{\partial g(\kappa|\mathbf{r}'-\mathbf{r}|)}{\partial \hat{\mathbf{n}}'} - g(\kappa|\mathbf{r}'-\mathbf{r}|) \frac{\partial U(\mathbf{r}')}{\partial \hat{\mathbf{n}}'} \right] dS', \quad \mathbf{r} \in V \quad (3.1)$$

where $\hat{\mathbf{n}}'$ represents the surface normal pointing outwards, g is the Green's function and

$$U^{(inc)}(\mathbf{r}) = \frac{1}{4\pi D} \int_V S(\mathbf{r}') g(\kappa|\mathbf{r}'-\mathbf{r}|) dV \quad (3.2)$$

is the average intensity obtained in the absence of the surface. Eq. [3.1] gives an expression for the general case of a light source that has a spatial distribution $S(\mathbf{r})$. In the previous chapter we saw that there are two sources of light for the forward problem of figure[1.3], the first is the laser source of wavelength λ_a , (eq.[2.31]) that illuminates the medium and the second are the fluorescent molecules that emit light of wavelength λ_b , (eq.[2.45]) when excited by the diffuse excitation light. By inserting the corresponding source term for each case, the expressions for the diffuse light in the presence of boundaries are derived.

3.1.1 Boundary Conditions

In order to find a solution at the surface of the medium, the boundary conditions must also be considered. For the derivation of the boundary conditions we will assume an interface that separates two regions with different indices of refraction. For the case of a biologic medium the surface separates the tissue whose index of refraction is usually approximated with that of the water, $n_{in} \sim 1.333$ and the air whose index of refraction is $n_{out} = 1$. Within the diffusion approximation the exact boundary condition for an index mismatched boundary is that the component of the flux normal to the interface, pointing from the non-scattering medium into the turbid medium, must be zero [84, 85]:

$$\mathbf{J}_{in}(\mathbf{r}) = 0. \quad (3.3)$$

In the case where the turbid medium is bounded by a transparent medium (like the tissue-air case) and their refractive indices are substantially different then we must consider all the possible Fresnel reflections at the interfaces from the flux inside the turbid medium [84]. The zero-flux condition must also be considered(eq.[3.3]) and therefore it is assumed that all the flux traversing the interface is toward the non-diffusive medium.

$$\mathbf{J}_{out}(\mathbf{r}) = J_n(\mathbf{r}).$$

Thorough derivation of the boundary conditions can be found in Refs. ([84, 85]). Generally, the boundary condition is expressed as an equation that relates $U(\mathbf{r})$ with $\mathbf{J}(\mathbf{r})$ at the interface,

$$U(\mathbf{r}) = C_{nd} \mathbf{J}(\mathbf{r}) \cdot \hat{\mathbf{n}} = C_{nd} J_n(\mathbf{r}), \quad (3.4)$$

where $\hat{\mathbf{n}}$ is the surface normal pointing outwards from the medium, J_n is the total flux traversing the interface and C_{nd} is a coefficient which takes into account the refractive index mismatch. For the cases of tissue/air interface $C_{nd} \sim 5$ [84, 85].

3.1.2 The expression for the flux at the boundary

Let us now go back to the previous section and equation [3.1]. We will rewrite it in terms of the flux $J_n(\mathbf{r})$ by using the boundary conditions (Eq. 3.4) and the Fick's law at the boundary, which relates the average intensity with the flux ($J = -D \frac{\partial U(\mathbf{r})}{\partial \hat{\mathbf{n}}}$).

$$J_n(\mathbf{r}) = \frac{1}{C_{nd}} U^{(inc)}(\mathbf{r}) - \frac{1}{4\pi C_{nd} D} \int_s \left[C_{nd} D \frac{\partial g(\kappa |\mathbf{r}' - \mathbf{r}|)}{\partial \hat{\mathbf{n}}'} - g(\kappa |\mathbf{r}' - \mathbf{r}|) \right] J_n(\mathbf{r}') dS', \quad \mathbf{r} \in S \quad (3.5)$$

The $J_n(\mathbf{r})$ can be found explicitly by solving the above equation. In order to solve the eq.[3.5] let us look again at the quantities of eq.[3.22]. The Green's functions are given from the corresponding Helmholtz equation of eq.[2.14] that describes the propagation of light given the source of light and the optical properties of the medium. In the previous chapter we assumed average values for the optical properties of the medium, namely the scattering and the absorption coefficients, in a heterogeneous medium which is the case of tissue. The average values of the scattering and absorption coefficients are obtained from optical characterization studies of the mouse tissue. In this work the applied average values for scattering coefficient and the absorption coefficient are $\mu'_s = 16 \text{ cm}^{-1}$ and $\mu_a = 2 \text{ cm}^{-1}$ respectively. In the next chapter, we will present a means of normalizing the data so that the contributions of the homogeneities effectively cancel out. The use of normalized measurements for reducing the effect of optical heterogeneity in tissue imaging has been experimentally justified [86].

Furthermore, for solving the surface integrals of eq.[3.5] the surface geometry must be known accurately. A method of retrieving the surface is by applying surface reconstruction algorithms such as those proposed in ref.[47]. In these measurements shadow projections of the subject are captured by a camera when a broad homogeneous white light source illuminates an opaque subject at different angles. The surface reconstruction was obtained by processing all projections (shadows) [87] using a back-projection algorithm. Details of this procedure can be found in ref.[88].

Accurate algorithms such as the Boundary Element Method [89, 90] or approximations to it such as the Kirchhoff Approximation [91], have been developed that provide solutions to the eq.[3.5].

3.2 Free space propagation, the basis for non-contact tomography

We will refer again to the basic experimental scheme of Fig. [1.1] in order to complete the solution to the forward problem. The CCD camera detects the light emerging from the subject by focusing on the surface. The expressions for flux at the surface boundary, $J_n(\mathbf{r})$ were derived previously in this chapter. Once we have studied the way light propagates in diffuse media of arbitrary shape, we have to relate the flux at the interface to the measurement at the CCD (see figure 3.1a). To do so we have to account for the free-space propagation of the diffuse light from the surface to the camera to transform the values at the focal plane of the imaging system to values at its image plane.

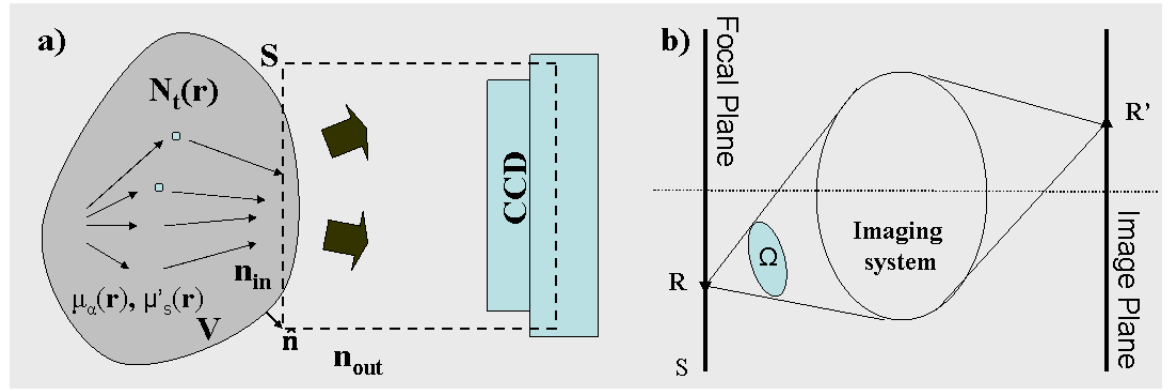


Figure 3.1: a) the free propagation of diffuse light, b) imaging system for a plane in focus

Let us consider the geometry of figure 3.1b which shows an imaging system that projects images of the focal plane to the image plane. The measurement at the position \mathbf{R} of the focal plane is imaged on the CCD at position \mathbf{R}' . For the case of our experimental setup, the focal plane lies at the surface of the subject and the image plane is at the chip of the CCD camera. The camera, thus is projecting the flux values at the surface to camera images. In an ideal imaging system there is a linear relationship between \mathbf{R} and \mathbf{R}' for the angles that fall within the numerical aperture Ω . For the analysis shown here, we will assume that we have an ideal imaging system, and we will focus on points lying at the focal plane. In free space the light is not diffusive and thus in the following analysis all the expressions will be derived in terms of the specific Intensity (section (2.1)). Since CCD cameras measure power we will recall that the specific intensity was defined as the average power flux propagating along the unit vector $\hat{\mathbf{s}}$.

Let us now assume that the intensity is irradiated from the surface element dS located at \mathbf{R} (see figure 3.2). By defining \mathbf{b} as the differential surface normal of dS , the total power that is emerging from \mathbf{R} due to dS , to the solid angle Ω is given by the following expression:

$$P(\mathbf{R}) = dS \int_{\Omega} I(\mathbf{R}, \hat{\mathbf{s}}) \mathbf{b} \cdot \hat{\mathbf{s}} d\Omega \quad (3.6)$$

As stated earlier for an ideal imaging system, $P(\mathbf{R})$ is equivalent with the power measured at the image plane, $P(\mathbf{R}')$.

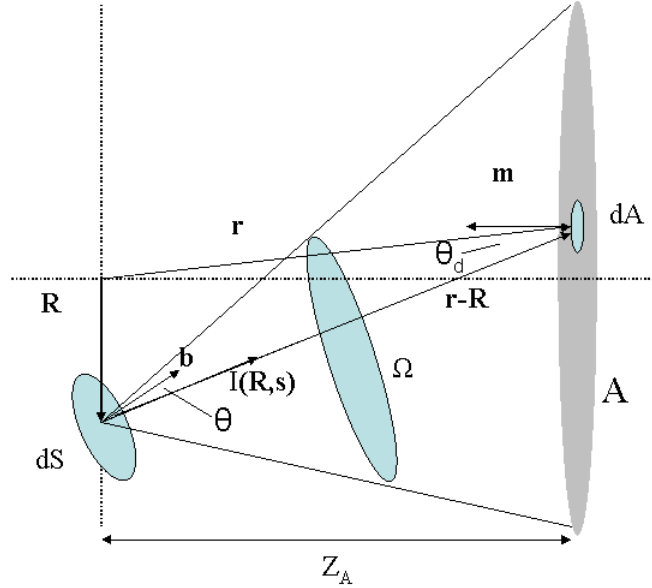


Figure 3.2: a differential emitting area dS and its contribution in the stop area A

According to the figure 3.2, the solid angle Ω for each position \mathbf{R} is defined by the area A which is the stop area of the imaging system. Let us now express the differential angle $d\Omega$ in terms of the differential area dA at the aperture, as:

$$d\Omega = \frac{\mathbf{m} \cdot \mathbf{u}_{\mathbf{R}-\mathbf{r}}}{|\mathbf{r} - \mathbf{R}|^2} dA \quad (3.7)$$

where \mathbf{m} is the normal to the aperture as shown in the figure 3.2 and

$$\mathbf{u}_{\mathbf{R}-\mathbf{r}} = \frac{(\mathbf{r} - \mathbf{R})}{|\mathbf{r} - \mathbf{R}|} \quad (3.8)$$

denotes for the direction of the specific intensity in terms of the position of the measurement \mathbf{R} and the vector \mathbf{r} that defines the position of the differential area dA in the aperture. By using the eqs.[3.6] and [3.7] the total power emitted by dS is given by integrating over the total area of the aperture:

$$P(\mathbf{R}) = dS \int_A I(\mathbf{R}, \mathbf{u}_{\mathbf{R}-\mathbf{r}}) (\mathbf{b} \cdot \mathbf{u}_{\mathbf{R}-\mathbf{r}}) \frac{(\mathbf{m} \cdot \mathbf{u}_{\mathbf{R}-\mathbf{r}})}{|\mathbf{r} - \mathbf{R}|^2} dA. \quad (3.9)$$

We can rewrite the eq.[3.9] as:

$$P(\mathbf{R}) = dS \int_A I(\mathbf{R}, \mathbf{u}_{\mathbf{R}-\mathbf{r}}) \cos \theta \frac{\cos \theta_d}{|\mathbf{r} - \mathbf{R}|^2} dA, \quad (3.10)$$

where $\cos \theta$ and $\cos \theta_d$ have replaced $\mathbf{b} \cdot \mathbf{u}_{\mathbf{R}-\mathbf{r}}$ and $\mathbf{m} \cdot \mathbf{u}_{\mathbf{R}-\mathbf{r}}$.

Since there is a direct correspondence between the emitted area dS at \mathbf{R} with the detector differential area at \mathbf{R}' the total power measured by a detector element (a CCD pixel, for example) due to the power emerging from the surface is given as:

$$P_S(\mathbf{R}') = \int_S \int_A I(\mathbf{R}, \mathbf{u}_{\mathbf{R}-\mathbf{r}}) \cos \theta \frac{\cos \theta_d}{|\mathbf{r} - \mathbf{R}|^2} dA dS. \quad (3.11)$$

For the case that the dependence of I on \mathbf{R} and \mathbf{r} is known, this surface integral can be solved explicitly and the total power at the detector can be calculated.

Let us now assume the limiting case where the distance of the surface from the camera is much bigger than the camera's aperture. In practice this can be achieved if we make the diameter of the camera aperture very small. Then the angular dependence in the integral of eq.[3.10] may be approximated to a constant as shown below:

$$P(\mathbf{R}) = dS I(\mathbf{R}, \mathbf{u}_{\mathbf{R}-\mathbf{r}}) \cos \theta \frac{\cos \theta_d}{|\mathbf{r} - \mathbf{R}|^2} dA. \quad (3.12)$$

With this assumption, Eq. [3.11] becomes:

$$P_S(\mathbf{R}') = \int_S I(\mathbf{R}, \mathbf{u}_{\mathbf{R}-\mathbf{r}}) \cos \theta \frac{\cos \theta_d}{|\mathbf{r} - \mathbf{R}|^2} dA dS. \quad (3.13)$$

So far, no assumption has been made for the expression of I . We should find an equation that relates the specific intensity I with the surface flux J_n . The surface flux J_n is given by the expression of eq.[3.5]. To find an expression for the specific intensity I we shall introduce the Lambertian approximation [7] which is frequently used to describe light emerging from a diffusive medium into free space. The Lambertian approximation states that the radiance from a certain surface point is isotropic, yielding a cosine dependence for the power. It should be stated say that there are studies that have proposed other more accurate approximations for the dependency of the specific Intensity from the diffuse field at the surface, however the Lambertian approximation is a simple approximation that has been shown to providing accurate results.

Let us assume that a surface S separates the diffusive medium from the air, then the flux through the surface to the free space is:

$$J^+(\mathbf{r}) = \int_{(2\pi)^+} I(\mathbf{r}) \hat{\mathbf{n}} \cdot \hat{\mathbf{s}} d\Omega. \quad (3.14)$$

For an isotropical source, we have $\mathbf{n} \cdot \hat{\mathbf{s}} = \cos \theta$, and eq.[3.14] gives $J^+(\mathbf{r}) \propto I(\mathbf{r})$. Making use of the boundary condition that arises from considering $J_n = J^+$ we obtain the following relation

between the specific Intensity and the flux at the boundary.

$$I(\mathbf{r}, \hat{\mathbf{s}}) = \frac{1}{\pi} J_n(\mathbf{r}) \quad (3.15)$$

If we introduce the eq.[3.15] to the eq.[3.13] we obtain for the total power at the detector \mathbf{R}' :

$$P_S(\mathbf{R}') = \frac{1}{\pi} \int_S J_n(\mathbf{r}) \cos \theta \frac{\cos \theta_d}{|\mathbf{r} - \mathbf{R}|^2} dA dS. \quad (3.16)$$

We can rewrite the eq.[3.16] as:

$$P_S(\mathbf{R}') = \frac{1}{\pi} \int_S J_n(\mathbf{r}) \Gamma(\mathbf{r}, \mathbf{r}_d) dS, \quad (3.17)$$

in terms of the function $\Gamma(\mathbf{r}, \mathbf{r}_d)$:

$$\Gamma(\mathbf{r}, \mathbf{r}_d) = \xi(\mathbf{r}, \mathbf{r}_d) f(NA, \cos \theta_d) \cos \theta \frac{\cos \theta_d}{|\mathbf{r} - \mathbf{R}|^2} dA. \quad (3.18)$$

Eq.[3.18] is the function that accounts for light propagation in free-space from the surface to the detector. In eq. [3.18] we have introduced ξ is a visibility factor that discards surface points not visible from the detector due to surface's geometry, and the function f which depends on the angle θ_d between the detector area and the line of sight, and on the numerical apperture, NA of the detector.

The eq.[3.17] expresses a practical thing: once we have the solution for the J_n at the boundary the free-space propagation of the diffuse light is accounted for and the values of J_n at the surface can be related to the camera measurements. If we recall the discussion of section(1.3), then with the analysis of this section, the solution to the forward problem has been completed. We have found the expressions that predict the measurements at the camera, $X_{prop}(\mathbf{r}, \mathbf{s}, t, \lambda_a, \lambda_b)$ given the source $X_{prop}(\mathbf{r}, \mathbf{s}, t, \lambda_a, \lambda_b)$ and the distribution of the fluorophores $N(\mathbf{r})$ inside the medium.

We will discuss now a practical parameter that plays an important role in tomographic imaging, and that is the efficiency in terms of the computational time. Although we included a lot of approximations for the derivation of a simple solution, we have to account for the computational cost when evaluating data from in-vivo measurements. With the implementation of CCD cameras for tomographic imaging, the size of data sets has significantly grown. CCD cameras chip sizes of 512×512 or 1024×1024 pixels yield measurement sets in the order of $10^6 - 10^8$ data.

From the analysis of section(3.1.2), we recall that the explicit modelling of the boundaries is needed in order to solve the integral of eq.[3.5] and thus to find $J_n(\mathbf{r})$ at the surface. The calculation of the surface integral results in great computational needs especially for the case

of camera measurements where $10^6 - 10^8$ different surface points need to be calculated. A method that significantly simplifies and accelerates calculations in the tomographic problem will be presented in the next section. This approach effectively removes the contribution of the boundaries and thus eliminates the need for explicitly modeling arbitrary geometries. The “boundary removal” approach transforms surface measurements to measurements which would be obtained if no boundary was present, i.e. if the diffuse volume was infinite and homogeneous.

3.3 From finite to infinite

The analysis of this section is based on the study of the ref.[92]. Let us consider the two dimensional case of the problem of figure (1.1). A diffusive medium is bounded by the surface S and contains a distribution of fluorescent sources denoted by $S(\mathbf{r})$. The CCD camera is measuring from a distance the light that is emerging from the medium (see figure(3.3a)).

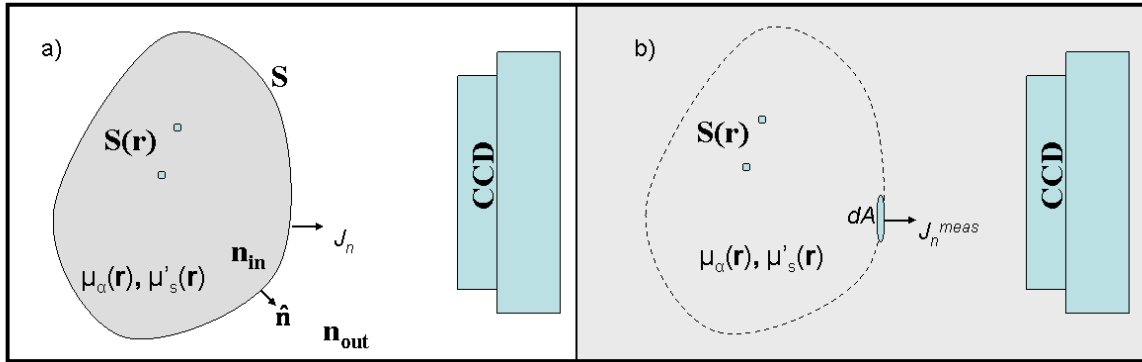


Figure 3.3: a) experimental configuration for non contact measurements b) transformation of the finite volume into infinite

In section (3.1.2) we showed that the effect of the boundaries was rigorously accounted for to obtain the complete expression for flux J_n at any surface point of the medium. We rewrite the eq. [3.5] here for convenience,

$$J_n(\mathbf{r}) = \frac{1}{C_{nd}} U^{(inc)}(\mathbf{r}) - \frac{1}{4\pi C_{nd} D} \int_s \left[C_{nd} D \frac{\partial g(\kappa |\mathbf{r}' - \mathbf{r}|)}{\partial \hat{\mathbf{n}}'} - g(\kappa |\mathbf{r}' - \mathbf{r}|) \right] J_n(\mathbf{r}') dS', \mathbf{r} \in S \quad (3.19)$$

and we recall that the expression for the incident field U^{inc} ,

$$U^{(inc)}(\mathbf{r}) = \frac{1}{4\pi D} \int_V S(\mathbf{r}') g(\kappa |\mathbf{r}' - \mathbf{r}|) dV \quad (3.20)$$

describes the infinite case solution of the given problem.

In eq.[3.20], we notice that the quantity $S(\mathbf{r})$ contains all the information for the spatial distribution of the source strength. The $S(\mathbf{r})$, for example may represent the spatial distribution of the fluorophores times the $U^{(inc)}$ (i.e. the fluorescent emission strength) inside a mouse’s body.

The Eq.[3.19], can be rewritten in a way that the “infinite case” average Intensity(eq.[3.20]) at any position \mathbf{r} on the surface is expressed as function of the flux $J_n(\mathbf{r})$:

$$U^{(inc)}(\mathbf{r}) = C_{nd}J_n(\mathbf{r}) + \frac{1}{4\pi D} \int_s \left[C_{nd}D \frac{\partial g(\kappa |\mathbf{r}' - \mathbf{r}|)}{\partial \hat{\mathbf{n}}'} - g(\kappa |\mathbf{r}' - \mathbf{r}|) \right] J_n(\mathbf{r}') dS', \quad \mathbf{r} \in S. \quad (3.21)$$

If the detector of the tomographic system can measure the surface flux $J_n(\mathbf{r})$ then we can provide the measured $J_n(\mathbf{r})$ to the right hand part of the equation 3.21 and we would have the values for the $U^{(inc)}(\mathbf{r})$ for the case that no boundary is separating the medium. The medium would then have the same optical properties everywhere in space while retaining the position and the strength of the light emitting sources (figure 3.3b). Measuring the $J_n(\mathbf{r})$ is feasible for an experimental setup like the one that is implemented in this work. In this system the CCD camera focuses on the surface of the medium and measures the energy density at the boundary. By applying the measured $J_n(\mathbf{r})$ to the eq.[3.21], we can derive “the infinite case” values of the intensity at the positions of a virtual surface lying at the same place where the real surface used to be. The infinite case expression (eq.[3.20]) then, is not representing the real geometry of the problem however it carries in a simple form all the information needed for distribution of the fluorescent sources.

We recall here that the primary aim of tomographic problem is not to correctly model light propagation for the given geometry of the medium but to reconstruct of the distribution of the fluorescent sources. The explicit modelling of the light propagation contains information for the fluorescent concentration. But, if this information is expressed in a more manageable form, that would be preferred in terms of computational efficiency. Since the source information is contained in the “infinite case” expressions, the benefits from simpler expressions are much more important. In an infinite homogeneous medium, given that we know the values of the intensity in one position(for example in the virtual boundary), the values of the intensity at any position in space can be easily retrieved. This allows geometries of arbitrary shape to be transformed into simple geometries such as a slab.

Let us now consider that the CCD is focusing on the medium surface. The CCD camera has the capacity to record the light that traverses the diffusive medium and therefore can provide values to the quantities J_n on the surface. We can imagine each pixel of the camera as separate detector. The surface of the medium is first discretized into a number of surface elements. Then, we attribute the values measured by the camera to the corresponding surface elements according to the method described in section (3.2).

The infinite-case-average intensity is becoming:

$$U_{meas}^{(inc)}(\mathbf{r}_i) = C_{nd}J_n^{meas}(\mathbf{r}_i) + \frac{1}{4\pi D} \sum_{j=1}^N \left[\frac{\partial g(\kappa |\mathbf{r}_j - \mathbf{r}_i|)}{\partial \hat{\mathbf{n}}_j} + g(\kappa |\mathbf{r}'_j - \mathbf{r}_i|) \right] J_n^{meas}(\mathbf{r}_j) dA_j, \quad \mathbf{r}_i \in S. \quad (3.22)$$

where each surface measurement of area dA_j at \mathbf{r}_j is represented as $J_n^{meas}(\mathbf{r}_j)$. This notation

is introduced in order to distinguish the measured quantities from the theoretical ones, $J_n(\mathbf{r}_j)$ and dS which give the rigorous solution to Eq.[3.21].

In the eq.[3.22], the terms $J_n^{meas}(\mathbf{r}_i)$ are given by the camera images. In order to solve the eq.[3.22], we follow the same process as for the finite boundary case discussed in section(3.1.2). The green's functions should be calculated given the source distribution and the optical properties of the medium. Furthermore, although the medium has been transformed to infinite, the extraction of its “finite case” surface is still necessary and the free space propagation formula is still needed. To explain this, we notice that the values $J_n^{meas}(\mathbf{r}_i)$ are given from projecting the camera measurements to the medium surface. The projection of the CCD measurements onto the surface is the inverse of what proposed in section(3.2), where the free-space propagation formula is presented to relate the outward flux measured at the interface to the measurements at the CCD. The surface information is necessary in order to corregister the measurements from the camera to the corresponding position of the animal body. For the surface extraction we apply surface reconstruction algorithms to shadowgrammetric measurments as discussed in section (3.1.2).

Eq.[3.22], imposes an important condition that needs to be met. We should have all values of the surface outward flux measured in order for the series in eq.[3.22] to be equivalent to a surface integral. Our first generation tomographic setup incorporating a rotation stage can measure the outward flux over 360^0 . In ref.[92] *Ripoll and Ntziachristos* studied the case where the surface of the subject is only partially covered. They performed numerical simulations on tissue like media and they calculated the deviations in correctly retrieving the surface integral when the number of the surface measurments is reduced. Their study showed that for the case where the fluorescent concentration is close to the surface errors in the order of 5% are induced if the camera is focusing on the area of the body where the targeted organ is expected to lie underneath. In all the experiments presented in this thesis, we had an a priori knowledge of the position of the fluorescent concentration since we wanted fast results for testing our technique. The subject was always placed in a position so that the sources of fluorescence were close to the focused part of the body. For the case that the region where the GFP cells are residing is not known a priori, the full angular coverage of the body scan is essential for correctly calculating the integral of eq.[3.22].

To conclude, the boundary removal method permits the use of the infinite case expression derived in Chapter two (eq.[2.49]) which we rewrite here for convenience:

$$U^{fluo}(\mathbf{r}) = \frac{\sigma^{fluo}\eta S_0}{16\pi^2 D_{fluo} D_{exc}} \int_V g_{exc}(\mathbf{r}_s, \mathbf{r}_1) N_t(\mathbf{r}_1) g_{fluo}(\mathbf{r}_1, \mathbf{r}) dV_1. \quad (3.23)$$

And the flux $J_n(\mathbf{r})$ at the virtual boundary is found in an analogous way with the finite case

after implying the boundary condition as expressed in eq.[3.4] to the above equation,

$$J_n^{fluo}(\mathbf{r}) = \frac{\sigma^{fluo}\eta S_0}{16\pi^2 D_{fluo} D_{exc} C_{nd}} \int_V g_{exc}(\mathbf{r}_s, \mathbf{r}_1) N_t(\mathbf{r}_1) g_{fluo}(\mathbf{r}_1, \mathbf{r}) dV_1, \mathbf{r} \in S. \quad (3.24)$$

Finally the infinite case values at the virtual boundary are given from the eq.[3.22] when applying the measurements of the CCD camera.

Chapter 4

Inverse problem

This chapter deals with the second step of our tomographic problem, i.e. the extraction of a fluorescent map inside the body from the camera measurements. In the previous chapter, we solved the Forward problem according to the geometry of our non-contact tomographic setup. We extracted the equations describing the fluorescent light emerging from a diffusive medium upon laser illumination and how surface flux is transformed into camera images.

A new method has been presented that effectively removes the contribution of the subject's boundary to the measurements. With this technique the bounded medium has become infinite covering the whole space. This technique permitted the description of the forward problem with the use of the simple infinite case.

This analysis will be used for solving the inverse problem as we will see in the following sections. We will start by introducing the Normalized Born expression and we will show its role in tissue tomography. It will be followed by an introduction to the inverse method which involves the discretization of the imaged volume in small elementary volumes called voxels. Based on the forward model we will formulate a set of linear equations with the contributions of each one of the voxels to the measured data as the unknowns. An algorithm which is called the Algebraic Reconstruction Technique (ART) will be used to give the solution to the above mathematical problem thus extracting the final tomographic image.

4.1 The Normalized Born algorithm

We will use an algorithm that has been proposed for reconstructing the distribution of the fluorescent concentration in diffuse media. Applying this algorithm offers great experimental simplicity in contrast with previous methods used for the reconstruction of the fluorescent distribution. The main idea behind this algorithm is that it is using the excitation measurement in order to account for the intrinsic properties of the medium.

Before moving to the introduction of the Normalized Born algorithm, we will summarize the steps of our analysis. In chapter 2 we derived the expression of the average Intensity for the case of an infinite medium that contains a distribution of fluorophores (eq.[2.51]). In chapter 3

we completed the forward problem by accounting for the contribution of the subject's surface to the expression of the Intensity inside a finite medium. We used a method that effectively removes the contribution of boundaries to the expression of the fluorescent light and permitted the use of the simpler “infinite case” expressions. So far the forward problem is solved, our model can predict the distribution of the light at the boundary of the subject, where the CCD camera is focusing. Let us go back to the equation that relates the light that is reaching the camera with the flux at the surface eq.[3.17]. In the previous chapter we mentioned that the inverse equation can be used to project the camera data to the surface. So far we assumed that we have an ideal detecting system. In order to fully simulate the power measured by a real CCD chip we have to account for the detector's characteristics like gain and attenuation factors:

$$P^{fluo}(\mathbf{r}_d) = QE_E^{\lambda_b}\Theta_f \frac{1}{\pi} \int_S \Theta_{det}(\mathbf{r}_d) J_n(\mathbf{r}) \Gamma(\mathbf{r}, \mathbf{r}_d) dS. \quad (4.1)$$

In eq.[4.1], QE_E represents the detector quantum efficiency, $\Theta_{det}(\mathbf{r}_d)$ accounts for the detector gains and Θ_f is the attenuation of the filter that measures the fluorescent light. The superscript *fluo* denotes that a band pass filter with a profile matching the emission peak of the fluorophores is adjusted in front of the camera. By applying the expression for the $J_n(\mathbf{r})$ from eq.[3.24] to eq.[4.1] we obtain:

$$P^{fluo}(\mathbf{r}_d) = QE_E^{\lambda_b}\Theta_f^{fluo} S_0 \frac{\sigma^{fluo}\eta}{16\pi^3 D_{fluo} D_{exc} C_{nd}} \int_V \int_S \Theta_{det}(\mathbf{r}_d) g_{exc}(\mathbf{r}_s, \mathbf{r}_1) N_t(\mathbf{r}_1) g_{fluo}(\mathbf{r}_1, \mathbf{r}) \Gamma(\mathbf{r}, \mathbf{r}_d) dS dV_1 \quad (4.2)$$

In eq.[4.2] all the position dependent factors $\Theta_{det}(\mathbf{r}_d)$ need to be calculated for each detector position.

In order to obtain a more manageable form to insert to the tomographic algorithms, let us assume that the measured subject does not contain fluorophores. We will refer to this as the excitation light whose expression has been derived in section (2.4.1). The Intrinsic light detected by the camera is obtained when placing a filter for the excitation wavelength λ_a in front of the camera:

$$P^{exc}(\mathbf{r}_d) = QE_E^{\lambda_a}\Theta_f^{exc} S_0 \frac{1}{4\pi^2 D_{exc} C_{nd}} \int_S \Theta_{det}(\mathbf{r}_d) g_{exc}(\mathbf{r}_s, \mathbf{r}_1) \Gamma(\mathbf{r}, \mathbf{r}_d) dS \quad (4.3)$$

Now, we will normalize the measurements for the subject for the fluorescence emission with the measurements for the case of the same subject for the excitation wavelength. The normalization method accounts for the Intrinsic properties of the medium.

$$P^{NB}(\mathbf{r}_d) = \frac{P^{fluo}(\mathbf{r}_d)}{P^{exc}(\mathbf{r}_d)} = a \frac{\sigma^{fluo}\eta}{4\pi D_{fluo}} \frac{\int_V \int_S g_{exc}(\mathbf{r}_s, \mathbf{r}_1) N_t(\mathbf{r}_1) g_{fluo}(\mathbf{r}_1, \mathbf{r}) \Gamma(\mathbf{r}, \mathbf{r}_d) dS dV_1}{\int_S g_{exc}(\mathbf{r}_s, \mathbf{r}_1) \Gamma(\mathbf{r}, \mathbf{r}_d) dS} \quad (4.4)$$

where,

$$a = \frac{QE_E^{\lambda_b} \Theta_f^{fluo}}{QE_E^{\lambda_a} \Theta_f^{exc}}, \quad (4.5)$$

is a calibration factor and can be calculated experimentally. This factor

The normalized Born expression normalizes the fluorescent intensity to the tissue heterogeneities. Another advantage of using the normalized Born expression is that position dependent factors are cancelled out.

In order to derive the Normalized Born expression the excitation measurement at the same medium where the fluorescent sources are residing should also be performed. The accuracy of the Born Approximation assuming homogeneous optical properties has been exhaustively studied in heterogeneous media in both phantom[86] and in-vivo experiments [41, 39], yielding excellent results.

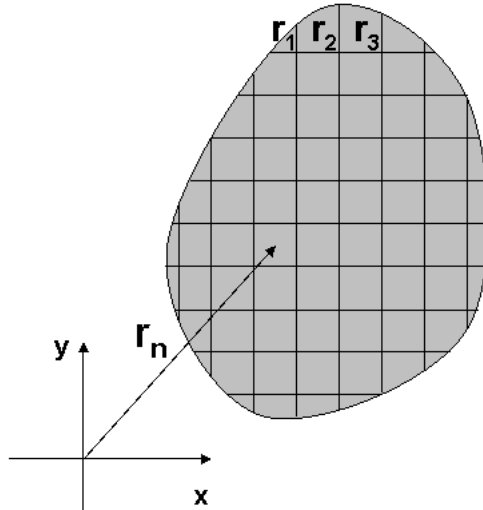


Figure 4.1: A square grid is discretizing the subject into N voxels

4.2 Discretization and the weight matrix

The Normalized Born expression is a way to normalize the measured data. In order to extract a tomographic image the medium can then be discretized into N volume elements, also known as voxels. To illustrate the discretization of the volume into small elements we will refer to the object of the figure (1.1). Although we will analyse the real case of a three dimensional subject in figure[4.1] we illustrate the two dimensional case.

The center of each voxel is given by \mathbf{r}_n . Within the Born approximation discretizing the volume we can represent the volume integrals as summations of N discrete volume elements. In each voxel the function $F(\mathbf{r}_n)$ is assumed to be constant. The discrete expression for the

Normalized Born intensity becomes:

$$P^{nborn}(\mathbf{r}_s, \mathbf{r}_d) = \frac{\eta\sigma^{fluo}\Delta V}{4\pi C_{nd} D^{fluo}} \sum_{n=1}^N \left[\frac{\int_S U^{exc}(\mathbf{r}_s, \mathbf{r}_n) \int_S G^{fluo}(\mathbf{r}_n, \mathbf{r}) \Gamma^{fluo}(\mathbf{r}, \mathbf{r}_d) dS}{\int_S J_n^{exc}(\mathbf{r}_s, \mathbf{r}) \Gamma^{exc}(\mathbf{r}, \mathbf{r}_d) dS} \right] F(\mathbf{r}_n) \quad (4.6)$$

Eq.(4.6) is written for a single measurement, i.e for a source at position \mathbf{r}_s and a detector at position \mathbf{r}_d . When using multiple source detector pairs a linear set of equations arises.

Let us assume p different source position and q different detector points, resulting in $m = p \times q$ different measurements, then the set of linear equations can be written in a form of matrices:

$$\begin{bmatrix} P^{nborn}(\mathbf{r}_{s1}, \mathbf{r}_{d1}) \\ P^{nborn}(\mathbf{r}_{s1}, \mathbf{r}_{d2}) \\ \vdots \\ P^{nborn}(\mathbf{r}_{sp}, \mathbf{r}_{dq}) \end{bmatrix} = \begin{bmatrix} W_{11} & W_{12} & \dots & \dots & W_{1n} \\ W_{21} & W_{22} & \dots & \dots & W_{2n} \\ \vdots & \vdots & \ddots & \ddots & \vdots \\ \vdots & \vdots & \ddots & \ddots & \vdots \\ W_{m1} & W_{m2} & \dots & \dots & W_{mn} \end{bmatrix} \times \begin{bmatrix} F(\mathbf{r}_1) \\ F(\mathbf{r}_2) \\ \vdots \\ \vdots \\ F(\mathbf{r}_n) \end{bmatrix} \quad (4.7)$$

the above equation can be written in a simple form as $\mathbf{P}_{M \times 1}^{nBorn} = \mathbf{W}_{M \times N} \times \mathbf{F}_{N \times 1}$. The \mathbf{W} matrix is called weight matrix. Each matrix element represents the contribution of each voxel to the fluorescent concentration based on the position of the source and the detector. A method to solve the above set of linear equations is to invert the weight matrix, and this task comprises the inverse problem (see section(1.3)).

4.3 The Algebraic Reconstruction Technique (ART)

In the previous section, we presented how the problem of extracting the fluorescent distribution can be transformed into a matrix inversion problem. Inverting the weight matrix can be performed in different ways depending on the size of the matrix. In our case where CCD camera measurements are involved the number of equations is in the order of 10^4 and the matrix cannot be directly inverted numerically.

We will use an iterative technique which is called Algebraic Reconstruction Technique (ART). Based on the method of projections, the ART method was originally developed for X-ray tomography. To illustrate better the steps of the technique we will consider a simpler case of the problem of eq.(4.7). We will consider a set of 2 linear equations with 2 unknowns:

$$\begin{aligned} W_{11}F_1 + W_{12}F_2 &= P_1 \\ W_{21}F_1 + W_{22}F_2 &= P_2 \end{aligned} \quad (4.8)$$

Each equation represents a line in the two dimensional (F_1, F_2) plane, as shown in the figure(4.2).

The solution (f_1, f_2) to the system of the two equations is given at the intersection of the two lines on the figure(4.2). The method of projections consists of starting with an initial guess (f_1^0, f_2^0) , projecting it to the first line then consequently projecting the resulting points from the one line to the other until the intersection point is reached. Projection from the one line to the other and back consists of one iteration.

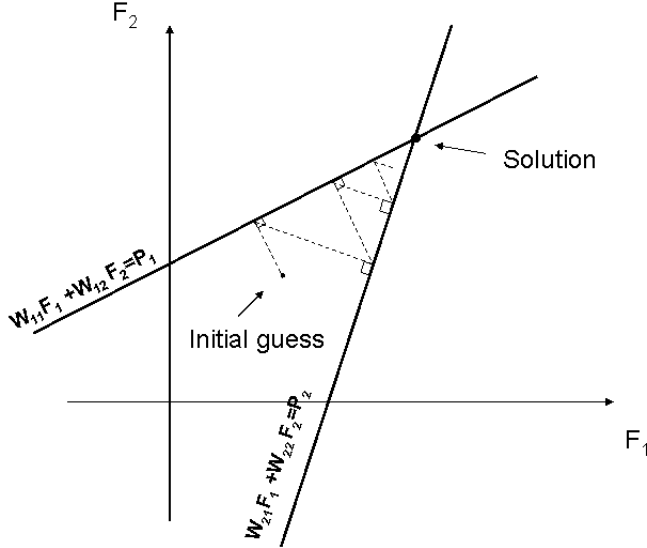


Figure 4.2: Graphical representation of the ART technique

We will correlate now the analysis presented above to the real general case of tomographic measurements expressed by the following set of equations (eq.[4.7]),

$$\begin{aligned} W_{11}f_1 + W_{12}f_2 + \dots + W_{1N}f_N &= p_1 \\ W_{21}f_1 + W_{22}f_2 + \dots + W_{2N}f_N &= p_2 \\ &\vdots \\ W_{M1}f_1 + W_{M2}f_2 + \dots + W_{MN}f_N &= p_M \end{aligned} \quad (4.9)$$

In the above set of linear equations, each equation represents a hyperplane in the N -dimensional space. The unique solution of the system is given at the point of the N -dimensional space where M hyperplanes are intersected. An initial guess is assumed, $(f_1^0, f_2^0, \dots, f_N^0)$ and the method of projections gives the convergence the solution to a unique point. An iteration for this case is defined as one full projection cycle over all the hyperplanes.

The extraction of a tomographic image with the inverse method proposed in this section is an ill posed problem and this means that there is not a unique solution. Below we present an analysis for the case of a well defined problem in order to demonstrates the role of the numbers M and N .

We can distinguish three cases depending the numbers of M and N in a well defined problem. For the case that $M = N$ the system has a unique solution. For the case that $M > N$ we

say that the system is overdetermined and for the case that $M < N$ we say that the system is underdetermined. The first case represents the 2×2 system of eq.(4.8) used for illustrating the ART method. In order to illustrate the other two cases, we will refer again to the simplified problem of eq.(4.8). When $M > N$ that means that there are more equations than unknowns and that can be illustrated by adding a third line to the figure(4.2) in order to obtain the figure (4.3a).

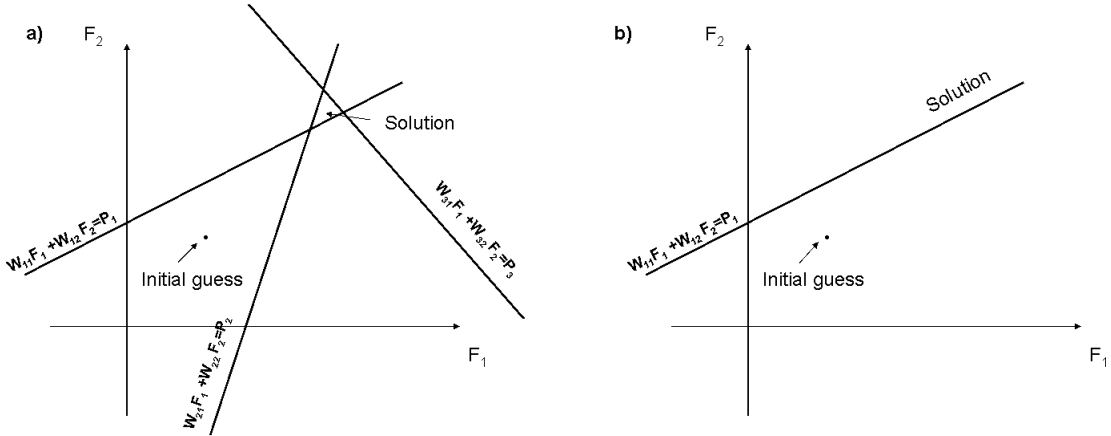


Figure 4.3: Schematic illustration of a) an overdetermined problem and b) an underdetermined problem

In the overdetermined case the solution does not converge to a single point but rather to the area formed by the intersections of the three lines. That means that the system cannot give a unique solution. On the other hand the case that the problem is underdetermined is when the equations are less than the unknowns. The graphic illustration of the underdetermined case is presented in figure(4.3b). At this case the system can have infinite number of solutions. For the case of a tomographic experiment the number of equations is given by the number of the voxels N comprising the mesh volume. The choice for the number of voxel is mainly governed by the desired resolution for the tomographic reconstructed image. The number of equations M is obtained by the number of tomographic projections. As we will see in chapter 6, in all case the number of projections was always greater than the number of the mesh voxels.

Chapter 5

Materials and Methods

This chapter gives an overview of the instrumentation implemented and the subjects measured on the experiments of this thesis. As subjects were used both mice and tissue-like phantom media. In this chapter we describe the mouse models that we measured as well as the fluorescent probes for labelling specific molecules. The biologic function related to each of the labelled proteins is also presented. Specifically T cells and microtubules, stained with the Green Fluorescent Protein comprised the two types of our targets inside the animal body. On the other hand, the tissue like phantom samples whose geometry and fluorescent properties can be controlled were used for the calibration of the system.

In this chapter, we will also give an overview of the instrumentation developed for performing optical tomographic measurements. A new tomographer was developed that tomographically images fluorescence activity inside living systems. The major innovation of the system is that it works in a non contact geometry resulting in simple experimental procedures while providing high resolution tomographic images. The experimental setup underwent multiple changes and improvements throughout this work. The first generation system incorporates a motorized rotation for the angular movement of the subject. Implementation of the rotation stage permits the full angular coverage of the animal body by the camera and the recording of angular projections for the tomographic algorithms. In the second generation system the subject is lying down on a plate while the camera is focusing from the top. The second generation setup was developed in order to improve issues like ease of use, animal comfort, information content and versatility in examining a great palette of subjects. For the validation purposes we choose to compare tomographic reconstructed signal against the actual number of fluorescent cells present in the targeted organ as provided by the cell sorting ex-vivo method of flow cytometry.

5.1 Transgenic mice

Transgenic mice expressing GFP under control of CD2 promoter in all T-cells (CD2-GFP) were generated as described in ref.[93]. Transgenic mice were backcrossed for at least ten generations in the C57Bl/10 (B10) genetic background. All mice were bred in the Institute

of Molecular Biology and Biotechnology animal facility under barrier conditions in accordance with established guidelines. Experiments were carried out with four- to six- weeks old male CD2-GFP transgenic and B10 control mice.

In collaboration of the Erasmus Medical Center Rotterdam (EMCR) we performed tomographic measurements on the testis of GFP CLIP-170 mice. It is known that the CLIP-170 protein is resides in spermatogonia. The CLIP-170 is a microtubule plus-end-tracking protein that has been implicated to the male germ-cell development from initial studies showing that male CLIP-170 knock-out mice are subfertile. Along with the knock-out mice, GFP CLIP-170 knock-in mouse models have been generated to study the function of the CLIP-170 protein. Recent studies involving the GFP CLIP-170 knock-in mice showed that CLIP-170 protein has a structural function in the spermatogenesis process, in particular in spermatid differentiation and sperm head shaping. Although, GFP-CLIP170 is expressed most abundantly in testis tubules, there is a localized staining of CLIP-170 in other tissues like in skeletal muscle. In skin, the protein is expressed to keratinocytes and in lymphnodes is expressed in dendritic cells. The generation of the transgenic mice expressing the GFP-CLIP170 fusion protein in all microtubules is described in ref. [[94]]. All mice were bred in the Erasmus Molecular Center in Rotterdam, Nederland animal facility. Experiments were carried out with twenty - week old male CLIP170GFPki transgenic mice and seventeen week old C57BL6 control mice.

5.2 Tissue-like phantoms

Tissue phantoms have been widely used for validating models of light propagation [95]. The material of the phantom should mimic the optical properties of tissue in terms of the scattering coefficient, the anisotropy factor, the absorption coefficient and the index of refraction. For fluorescent imaging studies a tissue phantom should also host a known concentration of fluorophore with well-known spectral properties.

Aqueous solutions made of Intralipid and Ink are widely used for simulating the optical properties of tissue. Intralipid based phantoms can be used either in liquid or solid form, in the latter case when adding a hardener to the solution. Intralipid is an emulsion of water and soy bean fat used for intravenous feeding of hospitalized patients. It is a polydisperse suspension of particles with an average diameter of $\sim 0.4 \mu\text{m}$, but a relatively wide range of sizes (i.e. from $\sim 0.1 \mu\text{m}$ to $\sim 1.1 \mu\text{m}$). Ink is used to simulate the absorption of tissue. Following the recipe of ref.[95], the optical properties can be controlled by varying the concentration of Intralipid and Ink. For the fluorescenct concentrations inside the medium we used CFSE¹ that excibits a fluorescence peak at 525nm and is widely used for simulating the emission of the GFP molecule.

A highly purified agar powder (A-7049, Sigma, USA) is dissolved in distilled water in the appropriate concentration (1%) and heated up to the melting temperature of 95 °C. We bring the mixture to a boil using a microwave oven. The agar solution alone has negligible absorption

¹

and very low turbidity. Thus, the desired scattering coefficient of the phantom are reached by adding appropriate amounts of Intralipid (IL) (Pharmacia, Italy), as a scattering medium. With this recipe the absorption coefficient of the phantom can also be adjusted by adding Ink to the solution. Borosilicate micro capillary tubes(Blaubrand, intraMARK) with an outer diameter of 1.6 mm and an inner diameter of 1.2 mm containing CFSE are embedded in the phantom material in order to induce a fluorescent concentration in a desired position inside the medium.

5.3 Experimental setup

The implementation and development of a noncontact system for imaging living subjects of arbitrary geometry was the main aim of the work presented in this thesis. The continuous development resulted in the materialization of two different experimental setups. In both setups, the basic idea is driven by the need of a versatile system for performing non contact measurments according to the basic experimental scheme shown in the introduction chapter of this thesis. In the following sections the technical characteristics of the two systems are presented.

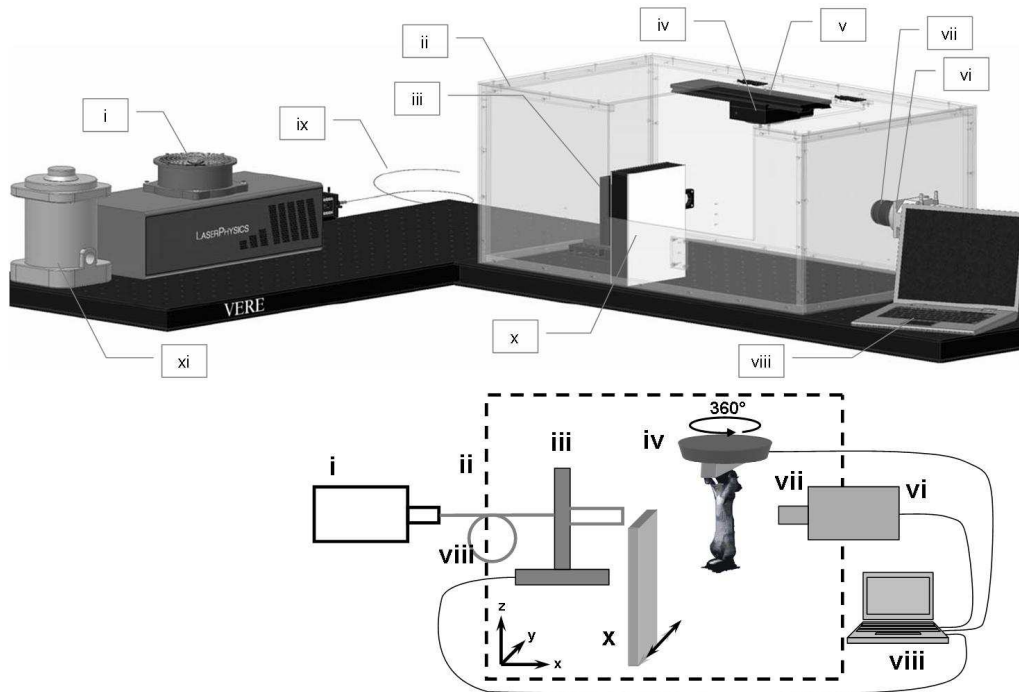


Figure 5.1: System setup for 3D in-vivo small animal imaging with all the main components numbered: (i) cw Ar+ Laser, imaging chamber (ii) shown here transparent for illustration purposes, (iii) x-z-translation stage with fiber, collimation optics and laser line filters, (iv) custom made diffuse light source for back illumination, (v) rotation stage with custom made specimen holder, (vi) CCD camera, (vii) 50mm f/2.8 objective lens, (viii, ix) multi mode fiber with mount, (x) rail for rotation stage, (xi) Isoflurane vaporizer, (xii) custom made chamber for deduction, (xiii) camera power supply.

5.3.1 First generation setup

The first generation system developed for performing non-contact Fluorescence Molecular Tomography is shown in fig. [5.1]. For the excitation of the fluorescent probes a cw Argon-Ion Laser (LaserPhysics, Reliant 1000m, West Jordan, UT 84088 USA) (*i.*) was used. The laser emits at several wavelengths through the visible spectrum. The main laser lines are at 458 nm , at 488 nm and at 514.5 nm . By placing filters in front of the laser source we choose the wavelength depending the excitation spectrum of the fluorescent probe. For all the experiments presented in this thesis we used the 488 nm laser line for exciting either the CFSE fluorophore or the GFP fluorescent protein. Protection against ambient light sources was provided by a custom-made 5mm-thick aluminum chamber (*ii.*) (shown transparent in fig.[5.1]).

A motorized X-Y translation system (model 8MT167-100, Standa, Vilnius, Lithuania) (*iii.*) provided the scanning of the illumination points on the surface of the target. The rotation stage (model 8MR180, Standa, Vilnius, Lithuania) (*iv.*), where the subject was placed, was fixed in an upside-down position on a frame, which can be moved on a rail (*v.*) along the optical axis of the camera. The signal acquisition was provided by a thermoelectrically cooled 16bit CCD camera cooled down to -70 C^0 , with a chip size of 1024×1024 pixels (Andor Corp., DV434, Belfast, Northern Ireland) (*vi.*). The CCD camera is equipped with a SIGMA 50mm $f/2.8$ objective (Sigma Corporation, Tokyo, Japan) (*vii.*), which was focused onto the subjects area closest to the camera. The CCD was mounted on one of the side plates of the chamber. In this particular setup, for the recording of the different projections, both the laser source and the sample can move while the camera is fixed on one side plate of the aluminum imaging box.

The system can be operated in either reflection or transmission geometries depending on the relative positioning of the translation stages with the beam collimating optics for the scan. The translation stages can be mounted either on the camera side (in reflection geometry) or in the optical axis of the camera (in transmission geometry) for performing a wide range of experiments for superficial or deep tissue probing, respectively. Data acquisition was performed on a 3.0 GHz PC with 512 MB RAM (*viii.*). Anti reflection coated emission band pass interference filters (55mm diameter) were used for signal detection of the various probes (Chroma Technology Corp., Bellows Falls, VT, 05101 US). For the excitation of the GFP molecule we applied a $488 \pm 1.5\text{ nm}$ bandpass filter(488FS03-25, Andover, USA) in front of the laser. For the recording of the GFP emission a 10 nm bandwidth filter (centered on 510 nm) was used. The excitation measurements were performed with a 55mm narrow-band filter for 488nm in front of the camera. The laser was coupled with a $600\mu\text{m}$ UVAN multimode fiber, NA=0.22, l=1.5m (FiberTech GmbH, 12459, Berlin, Germany) (*ix.*), and mounted on a 25mm x-y stage on a micro bank rail system (Linos, Germany). The beam was then aligned with a beam collimator to produce a 2mm diameter beam at the target. The whole system was mounted with a custom made holder to the X-Y translation stage. For the reconstruction of the three dimensional shape of the mouse a custom-made homogeneously illuminating source was constructed using an array of white

LEDs and two flat highly scattering white sheets of PMMA (*x*.). A Tec-3 Isoflurane vaporizer (*xi.*) (Lumic International, 21220 Baltimore MD) was used for induction and anesthetization of the subject. The output of the vaporizer could be directed either into the imaging chamber to a mask on the rotation stage for maintaining anesthesia throughout the measurements or into a separate chamber (see (*xii.*) in fig.[5.1]).

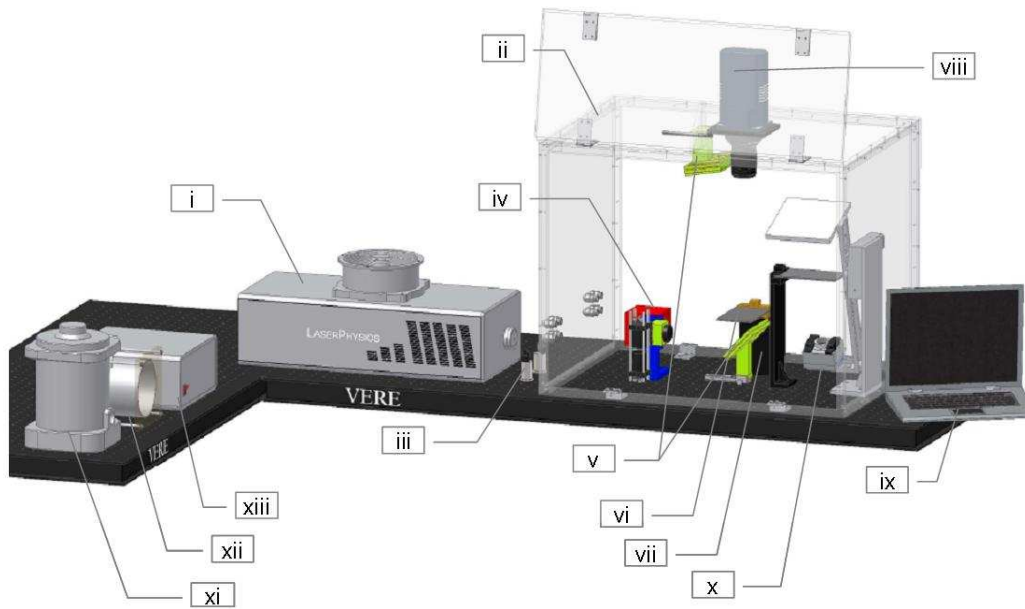


Figure 5.2: The second generation setup for non-contact in vivo imaging : (i) cw Ar+ Laser, (ii) imaging chamber, (iii) mirrors, (iv) scan head, (v) large mirrors, (vi) transparent plate, (viii) CCD camera, (ix) computer, (x) geometry extraction setup, (xi) Isoflurane vaporizer, (xii) custom made chamber for deduction, (xiii) camera power supply.

5.3.2 Second generation setup

The setup used for the measurements is shown on figure[5.2]. In respect with the first setup, the main difference is that the subject is lying down on a horizontal stage instead of being fixed in an upright position. The horizontal geometry was preferred because of its simplicity and also in terms of comfort for the mouse. In the new setup the positioning of the illumination source and the camera was changed accordingly.

In the second generation system, beam from the laser (*i.*) is guided inside the imaging box (*ii.*) with the aid of 2 mirrors(*iii*). The beam is entering a laser scanning device (Scancube 7, ScanLab)(*iv.*) which incorporates a system of mirrors mounted on miniaturized galvanometer motors (see figure[5.3]). The motors are controlled to move the mirrors and thus guide the laser beam into two directions. The above mentioned system is used to perform a scanning on the sample under study. The laser light is guided to the sample with the use of two large rectangular mirrors (mirror 4-6 Wave,73mm × 116mm, first surface mirror, Edmund Optics)(*v.*). The one is permanently mounted on the top plate of the aluminum box while the second lies on the

optical table and moves on a rail between two fixed positions (position 1 or 2) depending the geometry of the scanning. For measurements in the reflection geometry the bottom mirror is moved forth, in position 1 so light is illuminating the sample from the side of the camera after being reflected initially by the bottom mirror and then by the top mirror. For transmission measurements the bottom mirror is placed in position 2(see figure[5.4]).



Figure 5.3: Scan head and the route of the laser beam

The sample is placed on a transparent glass plate with an anti-reflection coating (Glassplate, High AR coated 96-99%(400-700nm),5" × 7",Edmund Optics)(vi.). The dimensions of the glass plate are 5" × 7" and is mounted on a X-Y-Z translation stage (Standa, Vilnius, Lithuania) (vii.). Depending the resolution demands the height can be adjusted with the movement on the Z axis. The X-Y movement aligns the subject in respect with the camera axis. The plate is mounted to the stages with a simple custom made clip system so that it can be easily removed and put back in the setup for the case of repetitive measurements. The CCD with the objective lens adjusted on (viii.) is mounted on the upper plate of the imaging box. Data acquisition was performed on a 3.0 GHz PC with 512 MB RAM (ix.).

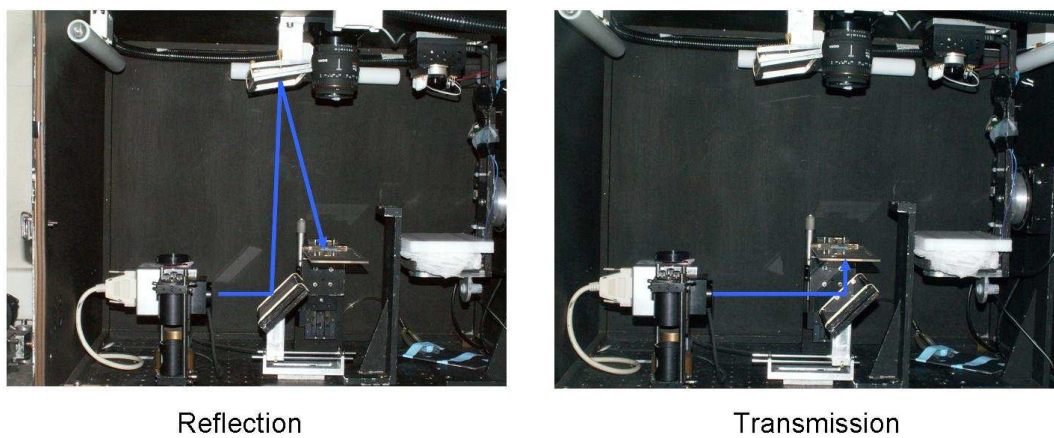


Figure 5.4: White light image that shows the major components of the second generation setup. The bottom mirror can move back and forth enabling measurements on both the reflection and the transmission geometry

The geometry of the subject is extracted by using a white homogeneous white light source that rotates around the subject (x .). A small CCD camera is positioned on the opposite side of the circle from the white light source. An aluminum arm holds the source and the detector and is mounted on a rotation stage. The circular movement is driven by a motorized rotation stage so that shadow projections are recorded for each angle of the arm.

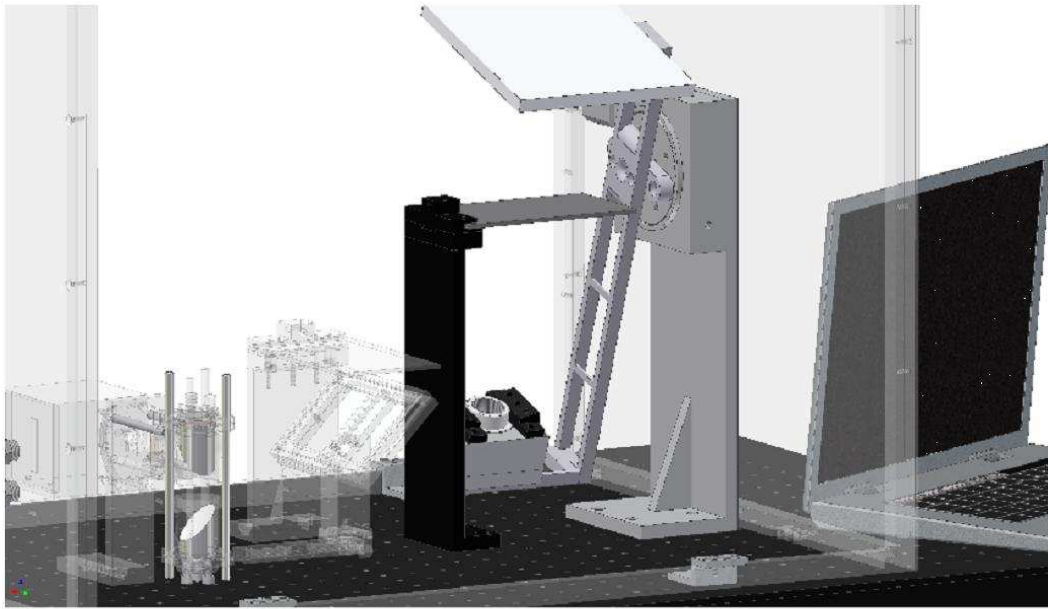


Figure 5.5: The setup for the geometry extraction. The plate of the stage is removed from the clip system of the main setup and placed on the surface extraction setup.

5.3.2.1 Fast laser scanning

The two motors can be controlled to move continuously in contrast with the step-by-step movement for the recording of the various projections. The exposure time of the camera is then controlled to record light as long as the movement lasts. This one projection measurement cannot be used in the tomographic algorithms, however it is a fast means to view the fluorescence activity in one image. These images are similar with those recorded by planar fluorescence setups [31]. A dense illumination pattern can be also applied for performing full coverage of the area. This type of measurement can be used to provide information of the origin of fluorescence signal before placing the sources for the tomographic scanning.

5.3.3 Synchronization of the devices

Measurements are performed via a custom made Labview program which controls the synchronous operation of the different components of the setup. The Labview sets and maintain a desired temperature of the camera chip throughout the experiment. The Labview program

initializes and controls the movement of the motorized components like the motorized stages or the galvanometer of the laser scanning device. Moreover it sets the exposure time of each camera shot. For the recording of the different projections the control program triggers the camera to record whenever the source or the subject has changed position.

5.3.4 Comparison between the two systems

The implementation of the rotation stage in the first setup permitted the movement of the subject in parallel with the movement of the illumination source. Additional recording of angular projections adds to the total number of projections enhancing the information content of the tomographic measurements. Another usefull feature of the rotation stage is that different body areas can be measured by turning the body area of interest in the field of view of the camera. In contrast, in the second generation system recording of different angular projections is not feasible. The horizontal positioning of the subject allows measurements only for two projections, at 0^0 and at 180^0 . The tomographic projections are only provided by scanning the laser source. The lack of angular projections could be balanced by recording large projection sets occuring from dense illumination patterns comprised of many source positions. Furthermore, access to different body areas is feasible with the new system by manually exposing the region of interest to the camera.

In comparison with the first generation system the second imaging system offers significant advantages in terms of simplicity and ease of use. The animal is simply placed on the plate and the only concern is to secure that the anesthesia gas is flowing into the animal's nose. In contrast in the first generation system the greater effort is needed to mount the animal on the rotation stage and to adjust the mask in its head. In addition the new system offers comfort to the animal when compared with the uncomfortable upright position of the subject on a rotation stage. In the new system, the animal lies on the stage in a physically relaxed position. In this thesis measurements performed in both systems are presented. Another important feature of the second generation setup is that shifting between the transmission and the reflection geometry is greatly simplified. In the new system the geometry of the illumination is chosen by simply shifting the bottom mirror back and forth. Performing measurements in both geometries can enhance the information content of the measurements.

5.4 Multi-subject Tomography

In the second generation system it is possible to place more than one subject under the field of view and thus multi-subject imaging is feasible. The field of view of the camera permits high throughput measurements. Within this work multisubject imaging has been performed for the case of two mice placed on the stage. However given the size of the subjects is relatively small tomographic measurements can be performed on even bigger number of subjects. In this

configuration the laser grid is adjusted to scan all the subjects.

The number of mice that can be placed is restricted by the field of view of the camera and the resolution requirements. Higher fields of view permit the imaging of many mice at the same time. On the other hand, greater fields of view result in lower resolution limits. Therefore the choice for the optimal configuration depends on the resolution requirements and the field of view of the camera. In the work presented here multi-subject measurements were performed on both adult and newborn mice. The anesthesia flow was modified to provide anesthesia in all subjects imaged.

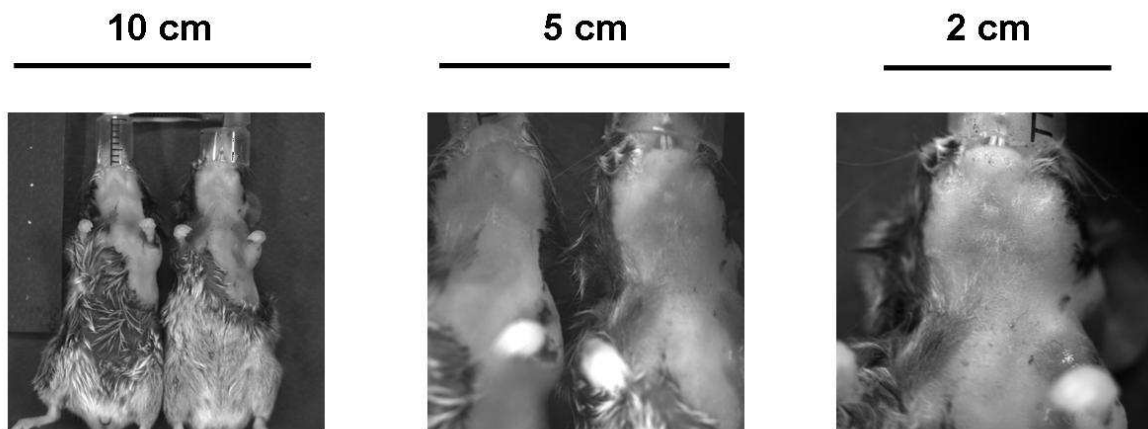


Figure 5.6: The field of view of the camera permits the performance of high throughput measurements. The motorized stage provides different levels of magnification

Multi subject tomography, is the most efficient way of achieving the same experimental conditions when comparing two living subjects. In particular it offers direct comparison of GFP positive against control animals since both are measured under the same experimental conditions. The laser source can irradiate the subjects with identical source grids and direct comparison is feasible. Finally we should state that the magnification of the camera images depends on the resolution requirements. Magnification is increased by moving the subject closer to the camera. In the first setup this is achieved by shifting the rotation stage on the rail while in the second setup the mouse holder is adjusted on a motorized stage that can move along the camera axis (see figure[7.6]).

5.5 Flow cytometry

The flow cytometry method was used to validate the FMT results and correlate them with the actual levels of expression inside the targeted organs. GFP cells from the targeted organs were analyzed after sacrificing the animal at the end of the FMT measurements.

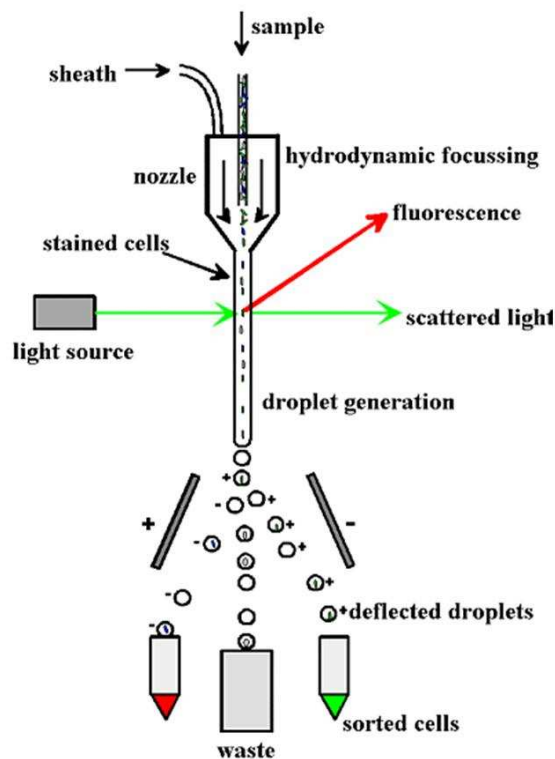


Figure 5.7: A simplified illustration of the flow cytometry principle

Flow cytometry analysis is a means to sort cells according to their fluorescence. In a flow cytometer individual cells traveling single file in a fine stream pass through a laser beam and the fluorescence of each cell is rapidly measured (figure[5.7]). A vibrating nozzle generates tiny droplets, most containing either one cell or no cells. The droplets containing a single cell are automatically given a positive or negative charge at the moment of formation, depending on whether the cell they contain is fluorescent; they are then deflected by a strong electric field into an appropriate container. Occasional clumps or cells, detected by their increased light scattering, are left unchanged and are discarded into a waste container. The facs analysis distinguishes and counts the GFP positive from the non fluorescent cells. The flow cytometry techniques allows large numbers of cells to be analyzed rapidly and automatically. For the experiments of this work, single cell suspensions were prepared from the targeted organs, after sacrificing the animal. Total number of cells were counted and the percentage of GFP expressing cells was determined by flow cytometry on a FACS (Fluorescence-Activated Cell Sorter) Calibur flow cytometer (BD Biosciences, San Jose, CA) and analyzed with CellQuest software.

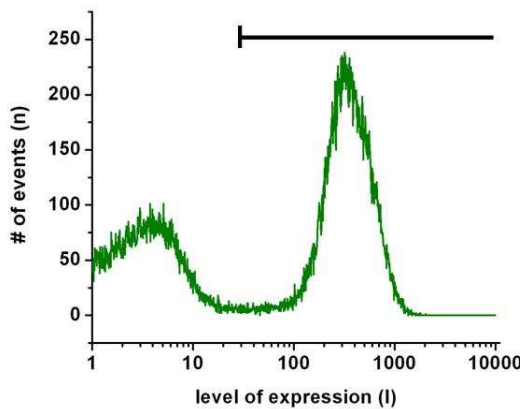


Figure 5.8: Flow cytometry data displayed as a histogram. The fluorescence intensity (x-axis) is plotted against the frequency at which this type of event occurs (y-axis)

A typical FACS analysis is shown in figure[5.8] as a histogram. The y axis represents the number of cell counts and the x axis represents the levels of expression. The histogram shows the distribution of the fluorescent cells over the various levels of expression. Since the fluorescence tomography reconstructs the number of fluorophores the FMT results were correlated with the normalized average of the distribution of the number of cells at the different levels of expression. This is given with the following expression:

$$\text{Normalized Average} = \frac{\sum_1^N n(l) \times l}{\sum_1^N n(l)} \quad (5.1)$$

In expression (5.1), $n(l)$ is the number of events as a distribution over the levels of expressions l .

Chapter 6

Experimental protocol

In this chapter we will describe all the steps followed for performing an experiment. The procedure starts by properly treating and anesthetizing the animal before placing it into the setup. We will deal with the levels of anesthetic gas and the oxygen as well as with the shaving process to remove the strongly absorbing fur. Next we describe the experimental steps until we have the complete set for measurements. The data processing follows in order to obtaining a tomographic image.

6.1 Mouse treatment

The adult mouse models of our study had a black fur covering their body. When performing optical measurements, the black fur causes attenuation on both the illumination light entering the body and on the light emerging from the body. For this reason, shaving of the mouse fur is necessary, in order to expose the skin at the region of interest.

Whether involving the shaving of the fur or the immobilization of the animal during the measurements, subject treatment is strongly correlated with the anesthesia process. Anesthesia of the subject is necessary for the immobilization and the manipulation of the animal. We could anesthetize the animal in two ways, either by an intravenous injection of a liquid anesthetic or the inhalation of a gas anesthetic. Treatment demands strongly depend on mouse age, as is the anesthesia of choice as well as the corresponding doses. Thus, according to the ages of our subjects we classified the mice into two groups. Newborns of age up to two weeks old are included in the first category and from this age up to 4 months in the other.

Avertin is a liquid anesthetic and is administrated via intravenous injection. Avertin doses depend on the weight of the mouse and on the time you maintain the animal under anesthesia. In particular, $13 \mu\text{L/g}$ for mice of weight below 10 g ¹ is enough to maintain the animal anesthetized for at least 30 minutes. Exceeding the above limits may become fatal for the subject. Recovery of the mouse may take tenths of minutes and is strongly suggested to avoid

¹Typical mouse weights are in the order of 10 g for mice of 1 month old, 20 g for mice of 2 months old and 30 g for mice of 3 months old

the use of gas anesthesia immediately after due to possible interaction between Isoflurane and Avertin. In cases when both types of anesthesia were used, Isoflurane anesthesia was provided at least 16 hours after the Avertin anesthesia. The main advantage of Avertin is that it offers flexibility in manipulating the mouse, i.e. when shaving of the hair is needed, in contrast to the gas anesthesia which requires the adjustment of a mask and the continuous delivery of gas. On the other hand, the maximum time under anesthesia by using Avertin cannot exceed 30 minutes and this limits its use for short experiments or for just shaving the mouse. Furthermore Avertin cannot be administrated to newborns since it is a strong anesthetic.

weight (gr)	8-16	16-20	20-28	>28
Avertin doses ($\mu L/gr$)	13	14	15	16

Table 6.1: Typical Avertin doses for maintaining the subject under anesthesia for ~ 30 min

Gas anesthesia is the method of choice for long experiments or for newborn mouse treatment. New born mice need special treatment since they are very sensitive and dependent on their mother. The anesthesia begins by setting the Isoflurane flow to 4 L/min and the Oxygen flow to 1 L/min . After two to three minutes, we set the level for the oxygen to 2 L/min and the Isofluorane to 2 L/min and we maintain these conditions throughout the measurements. Once the data collection is over we set the isoflurane to zero while leaving the oxygen flow for a couple of minutes. Mice of greater age also exhibit greater mobility and thus they were inititally placed into a chamber where the Isoflurane can be delivered. The output of the vaporizer could be directed either into the imaging setup for maintaining anesthesia throughout the measurements or into a custom chamber necessary for pre-tranquilization when attaching a mouse to the holder. Then the subject could be easily placed inside the imaging setup, with a mask adjusted to his face for the delivery of Isoflurane. The flows of the Isoflurane and the Oxygen were adjusted to 3 L/min and 2 L/min for the case of the chamber. When the mask is adjusted oxygen and Isoflurane flows should be set to 4 L/min and 1.5 L/min respectively. The above values are not general and each mouse may have a different response to gas anesthesia so for each different subject the flows should be specifically adjusted until normal breathing frequency was acquired. Normal breathing is also important in order to minimize movement due to muscle contraction. However the flows shold not vary a lot from the ones presented above. The main advantage of the Isoflurane is that it offers the possibility of keeping the animal under anesthesia for longer times, although the need of a mask compromises further treatment in terms of flexibility. However, during measurements the mouse should stay still and thus we chose to anesthetize the subject with Isoflurane.

The shaving process lasts from 10 to 30 minutes depending on the area of the skin that you want to expose. When using Avertin the doses should be adjusted to cover the time needed for completing the shaving. Regarding the shaving procedure, we first trim the hair with an

ordinary hair cutting machine. The remaining hair is then removed by using hair removing cream (Nair). We smooth on a thick, even layer to cover the hair. We leave the cream, initially, for a maximum of two minutes. Great care should be taken not to exceed two minutes to avoid burning of the animal skin, which is quite sensitive. Then, we gently wipe off the cream and hair with a pad and we rinse skin thoroughly with lukewarm water and we pat dry. One week old mice have not grown fur yet, so no shaving is needed. Fur growth on their back starts one week after their birth while in their front side it starts after two weeks. All the newborns measured had not grown fur yet.

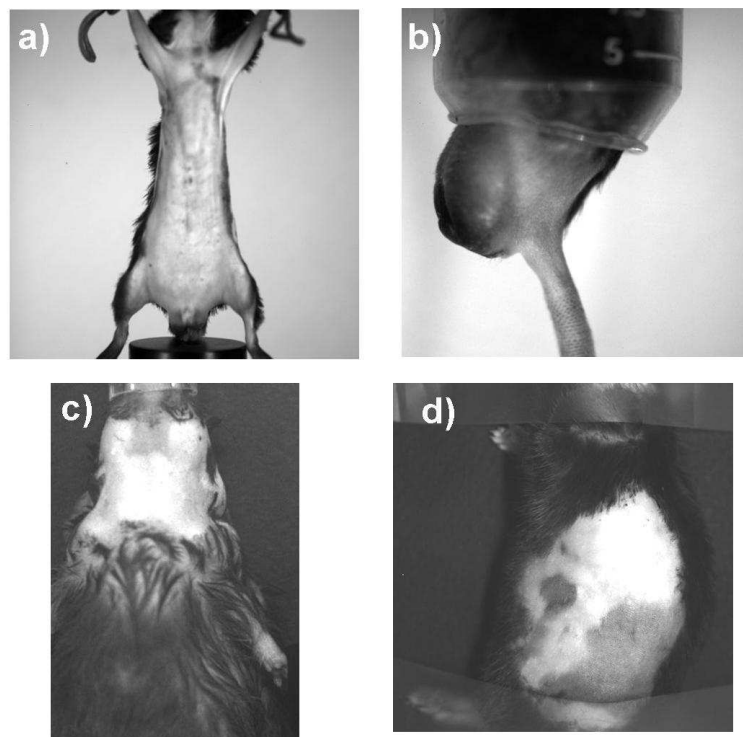


Figure 6.1: White light images showing different positions of the subject depending on the geometry of the targeted organ and the experimental setup used. a) the mouse is fixed on the rotation stage of the first setup and his whole body is captured by the camera. b) the testis of the mouse are bulging out while the mouse body is inserted into a hollow cylindrical tube. c) the neck area of the mouse is imaged from the top by the camera, in the second generation setup. d) the mouse is lying down on the stage of the new setup with its side facing the camera.

6.2 Experimental protocol

Initially, the subject is placed and fixed on the holder of the system. The way the subject is fixed depends of the position of the organ imaged and the resolution demands. In the experiments of this work we used two setups. Figure[6.1] shows different white light images of several of the geometries used for *in vivo* imaging depending the targeted organ. In the upper row, images of the first generation setup are shown while the second row has images of the horizontal setup.

In figure 6.1a the mouse is fixed in the upright position while a custom made base is supporting the body from below. We see that the magnitude of the objective is adjusted to cover the whole mouse body and thus whole body measurements can be performed. The configuration of figure 6.1b involves the imaging of fluorescence activity inside the testis of the mouse. We see that the mouse body is inserted into an plastic falcon tube whose bottom is open. The testis and the tail are exposed to the field of view of the camera. In this experiment the camera objective is adjusted to high magnification since we target the testis area of the mouse. In the first generation setup the subject can move at different angle positions and multiple angular projections can be recorded.

Regarding the second generation setup, figure 6.1c shows the mouse lying down on the plate of the setup while his ventral side is facing the camera. The camera is focusing on the neck area. The mask providing the gas anesthesia is adjusted to the mouse head. Finally figure[6.1d] we focus on the side part of the animal body. In the second setup different angular projections of the body can be visualized after turning the mouse body manually. In contrast the first setup incorporates a motorized stage that offers the angular movement of the subject for the complete coverage of the mouse body. However, the new setup offers significant advantages in terms of comfort as can be seen from these images, since the mouse is simply lying down instead of being stretched on the rotation stage of the first setup (see figure(6.1a)).

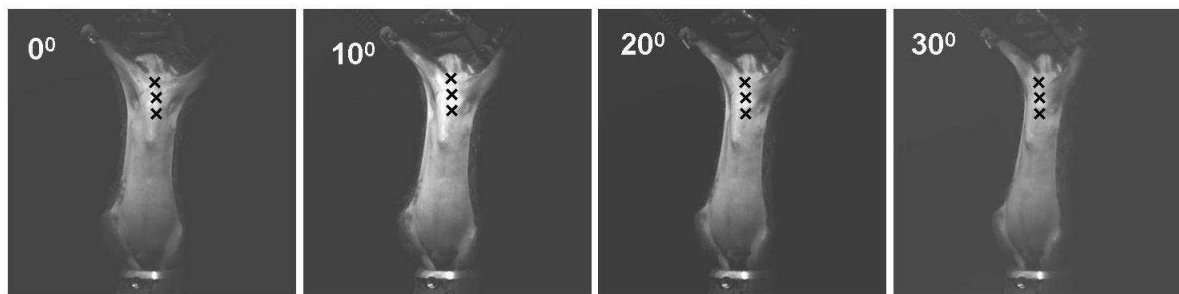


Figure 6.2: The arrangement of sources at 4 angle positions

6.2.1 Data collection

Once the subject is fixed the sources and/or and the angle steps are set using the LabViewTM software. The arrangement of sources is chosen according to the size and the shape of the targeted organ while the number of sources is based on the resolution requirements and the duration of the measurements. Since we wanted to test our technique in a fast way, we chose to point the sources directly to the area of the body where the targeted organ is expected to lie underneath. However, in case that the place of the fluorescent concentration is not known a priori, a full body scan can be performed, given that the time for the measurements does not exceed the limit of keeping an animal under anesthesia. We will present at this point an example of the steps followed for performing an experiment. Without loss of generality, the example concerns an experiment performed in the first generation setup(see figure[6.1a]). Let

us assume a transgenic mouse whose T cells in all the lymphoid organs are expressing GFP. Our target organ is the thymus, which is located in the chest area of the body $\sim 6\text{mm}$ below the skin above the heart. The reflection geometry is chosen and the illumination is performed from the same side with the camera. The laser beam irradiated the subject at the upper anterior torso where the thymus is located a few millimeters below the surface. In the second experiment, the scanning was performed on a vertical line employing 3 sources with the step size being 2.5 mm . In this case the subject was measured at 4 angular positions in steps of 10 degrees. Figure[6.2] shows the arrangement of the sources and the different angle projections for this particular experiment.

Once the source positions have been set, then the fluorescence and excitation signals are acquired with the corresponding filters. For the case of the GFP molecule we choose to illuminate with the 488 nm laser line. Figure[6.3] shows the profiles of the filters used for the collection of the excitation and fluorescence intensity with respect to the excitation and the emission spectra of the GFP. In this figure we also present an autofluorescence measurement obtained exciting with the 457 nm laser line and recording with the fluorescence filter ($510\pm 5\text{ nm}$). The autofluorescence measurements accounts for the autofluorescence of tissue, which is high in the visible range of the light spectrum. The idea behind the autofluorescence measurement is to illuminate at a wavelength far from the excitation peak of the GFP in order to mostly record the autofluorescence emitted by the tissue. The autofluorescence measurement is not inserted into the tomographic calculations, however it can be used by subtracting it from the fluorescence measurement. This method is used to enhance the contrast between the fluorescence and the autofluorescence background noise. An example of the autofluorescence subtraction is given in the results chapter for the visualization of the lymph node's position.

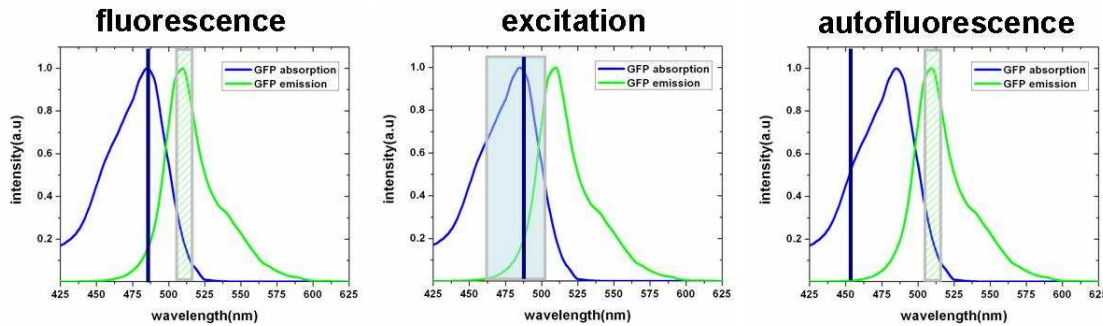


Figure 6.3: Three combinations of filter profiles and laser lines for the recording of the fluorescence, the excitation or the autofluorescence intensity

The laser power being delivered depends on the geometry used, whether it is in reflection or in transmission. For the fluorescence measurements, for both reflection and transmission geometry the laser power was in the order of tenths of milliwatts. For the excitation measurements laser power was in the order of tenths of milliwatts for the transmission mode and in the order of tenths of microwatts for the reflection mode. In order to form the Normalized Born

image for each projection two measurements were taken: one corresponding to the fluorescence emission, and one corresponding to the excitation wavelength. Thus, two images are recorded for each source position and/or rotation angle resulting in a $N_x \times N_y \times N_s \times N_r$ array of images for each type measurements, where N_x and N_y are the number of pixels in x and y direction respectively (1024×1024 or 512×512 for the case where a 2×2 binning is applied to the camera), N_s is the number of sources and N_r the number of angle steps.

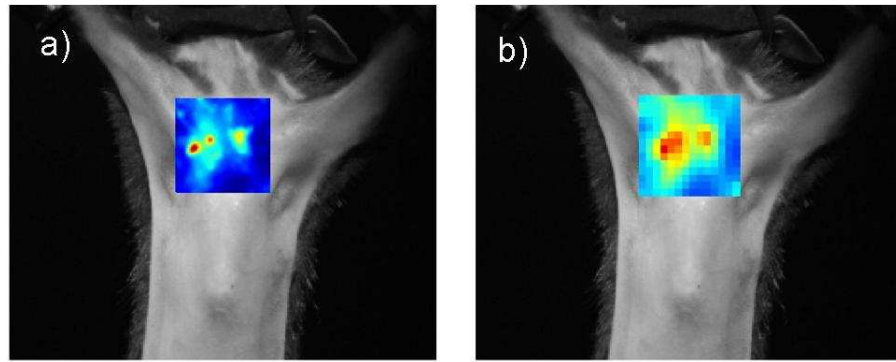


Figure 6.4: a) normalized Born averaged over all the source positions for one angular projection.
b) the selected detector grid for the reconstruction process

Finally, for the geometry extraction, 72 shadow images are recorded. The homogeneous light source illuminates the subject and the camera records one image for each 5 degrees angle step. The whole experimental procedure for each of the mice as described above took about 45 minutes, the fluorescence, excitation and the geometry measurements included.

6.3 Data treatment

Once the experiment is done, data is processed for the extraction of the tomographic image. The normalized Born approximation is calculated by dividing the fluorescence measurements with the excitation measurements.

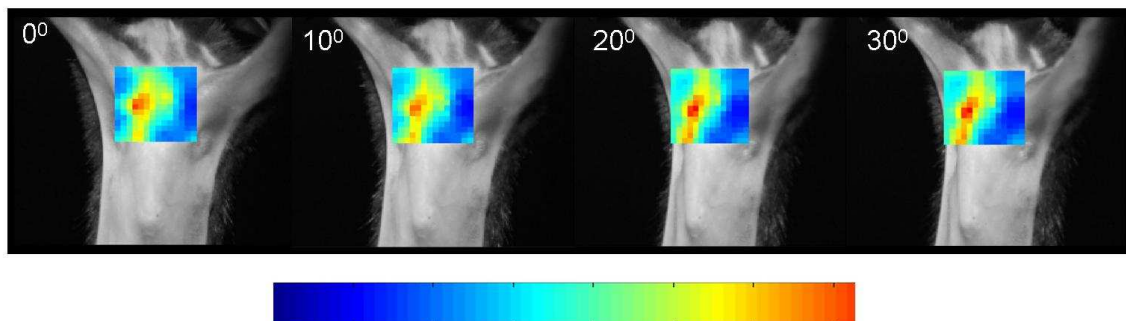


Figure 6.5: Normalized Born data of a transgenic mouse expressing GFP cells in the thymus

Each pixel in the camera can serve as a single detector, resulting in a detector array of thousands of single detectors. In a means similar to the pixel binning, combining the signal of adjacent pixels can make them one effective superpixel. Depending on the position of the targeted organ we choose the detector area and then we apply a detector grid. Detectors may overlap although in all the experiments presented here the detectors were chosen to be separate. In the experiment presented the detection area used was a 14×14 detector grid covering an area of $14 \times 8.5 \text{ mm}^2$. Typical surface areas for detector elements are in the order of 0.1 mm. In figure[6.5] we present Normalized Born detector data at four angular projections.

Once the surface of the subject is extracted the Normalized Born image is mapped onto the 3D surface. Before describing the procedure of mapping the Normalized Born image onto the surface area, we present in the following section the geometry extraction process.

6.3.1 Surface geometry extraction

A series of shadow and white light images of the subject in each rotation angle was acquired in order to reconstruct the 3D surface. For the 3D surface measurement 71 rotational steps with an increment of 5° and an integration time of 50 msec for each projection were required for a 3D map of the subject reliable enough to perform optical Tomography. Due to the fact that this technique deals with diffuse light, variations on the order of the mean free path (which is typically in the order of $\sim 1 \text{ mm}$), do not have an impact on the reconstructed image. This means that while the surface may change during the surface acquisition due to breathing, an average surface is retrieved which is accurate enough for Fluorescence Molecular Tomography.

6.3.1.1 Surface Reconstruction Algorithm

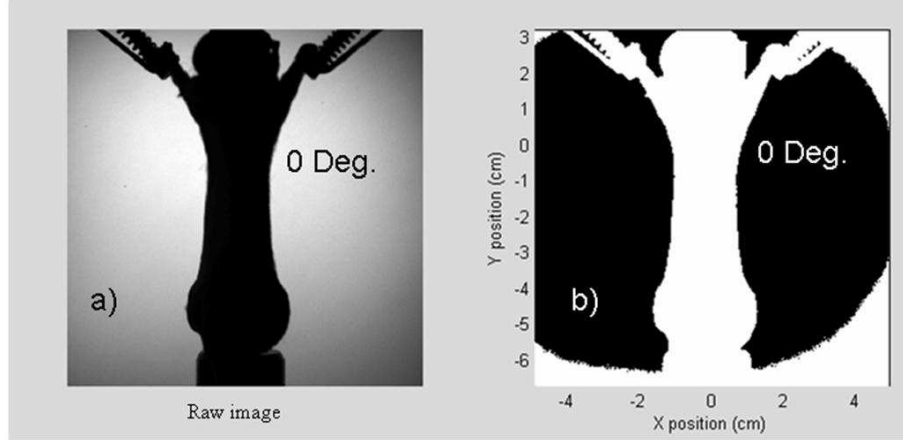
The surface information was obtained, by using the simple approach of adding all the projections (shadows) of the specimen, equivalent to the Radon transform method [47] with a constant filter. Before doing so, each image I for each projection angle θ_i was thresholded converting it into a binary image \bar{I} ,

$$\bar{I}(x, y, \theta_i) = \begin{cases} 1 & \forall I(x, y, \theta_i) > I_{th}^{(i)} \\ 0 & \forall I(x, y, \theta_i) \leq I_{th}^{(i)} \end{cases} \quad (6.1)$$

where x and y correspond to the pixels in the x and y directions, respectively, and I_{th} is the threshold value, which we set to 50 % of the maximum value of the image, i.e. $I_{th}^{(i)} = 0.5 \times \text{Max}\{I(x, y, \theta_i)\}$, which we have found to be the most robust approach for several signal to noise cases, ensuring proportional application of the thresholds to the existing illumination intensity, instead of using, for example, a fixed number of counts. Results for the geometry extraction algorithm are shown in figures[6.3.1.1a] and [6.3.1.1b] where we present the raw and the thresholded data, respectively, for a single projection.

Once all images have been thresholded, the axis of rotation has to be determined. One

way of finding the position of the axis of rotation when dealing with the radon transform is to find where the variance in the reconstructed image is maximum vs. the center of rotation [96]. This technique, however, does not yield good results when dealing with binary images as in our case, and especially with specimens subject to small changes in position due to breathing, for example.



a) shadow image as acquired from the system, b) shadow image thresholded to 50% of maximum intensity

We have found that the most reliable approach for finding the position of the axis of rotation is to determine the position as the one that minimizes the error between each projection and its mirrored 180° counterpart, using the following formula:

$$x_{center}^{(i)} = \text{Min} \left\{ \left| \bar{I} \left(x - x_{center}^{(i)}, y, \theta_i \right) - \bar{I} \left(- \left(x - x_{center}^{(i)} \right), y, \theta_i + \pi \right) \right| \right\} \quad (6.2)$$

Eq. (6.2) is used for each $(\theta_i, \theta_i + \pi)$ pair, and the final axial position is found as the average. We emphasize that Eq. (6.2) has proven to be very useful in-vivo where slight changes in position over time are observed. Once the axis of rotation has been determined, each angular projection is added up, forming the 3D volume occupied by the specimen. Then the surface can be easily extracted by finding those values slightly under unity (which would correspond to those pixels that appear in all projections) and using Matlab's (The Mathworks, Inc.) edge-based isosurface extraction algorithm. We have found that selecting the surface as the boundary of those pixel values that are over 0.8 consistently yields good results. Results for the subject presented in figure[6.3.1.1] are shown in figure[6.6a] and [6.6b] for the raw and thresholded reconstructed slices, respectively. A coarse surface mesh is shown in figure[6.6c], for 9033 triangular mesh vertices (typical numbers of vertices used are 90000). The final result for the case under study is shown in figure[6.6d] were the surface was rendered giving each triangular mesh a grayscale color related to the intensity obtained for a white light image for representation purposes and in order to accurately identify anatomical landmarks.

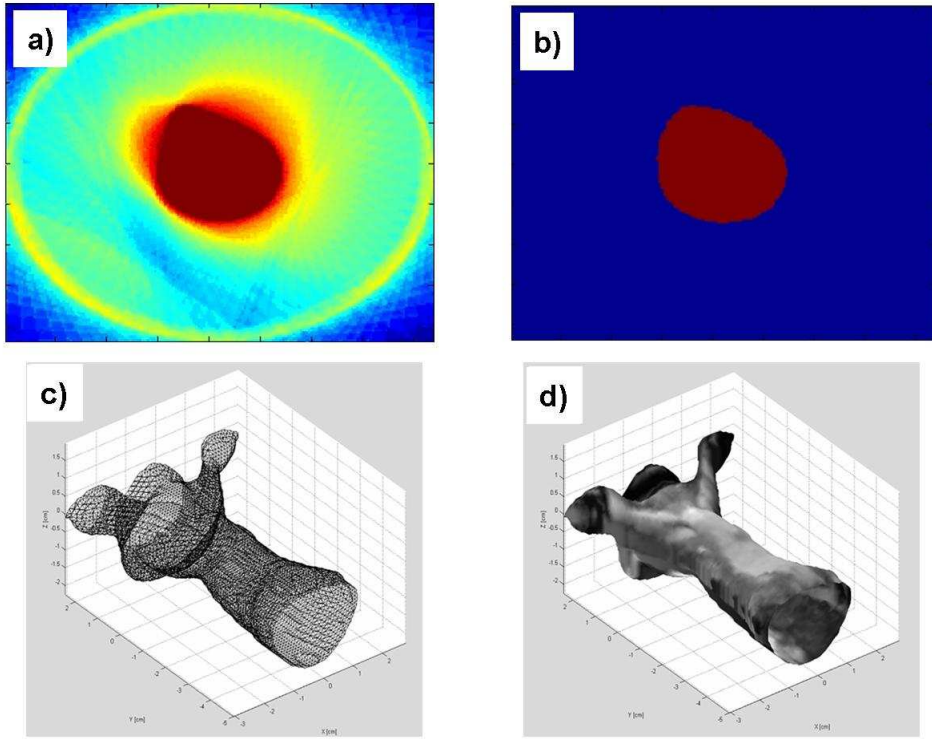


Figure 6.6: Backprojected data for one slice (each slice corresponds to one pixel line of the CCD) obtained with 72 projections, b) thresholded data, c) reconstructed surface mesh, d) rendered reconstruction

One of the main drawbacks when using this type of approach is the fact that convex surfaces cannot be reconstructed. However, to our benefit very few regions of the small animals used for imaging actually present convexity. Amongst them would be for example the regions under the fore and hind legs. When the complete (convex and concave) surface areas are needed, more advanced surface extraction approaches should be used such as 3D surface cameras [45, 46] or spatially modulated illumination patterns [97].

6.3.2 Data projection

The procedure followed for mapping the data onto the 3D surface is described in detail in section[3.2]. In order to project the camera images on the surface geometry we have used the non-contact equations that model free-space propagation of diffuse waves. The camera images are then projected on the surface of the animal body (see figure[6.7]). Figure[a] shows the flat image with the marked detector area of detectors while in [b] the camera images are rendered in the upper part of the reconstructed surface.

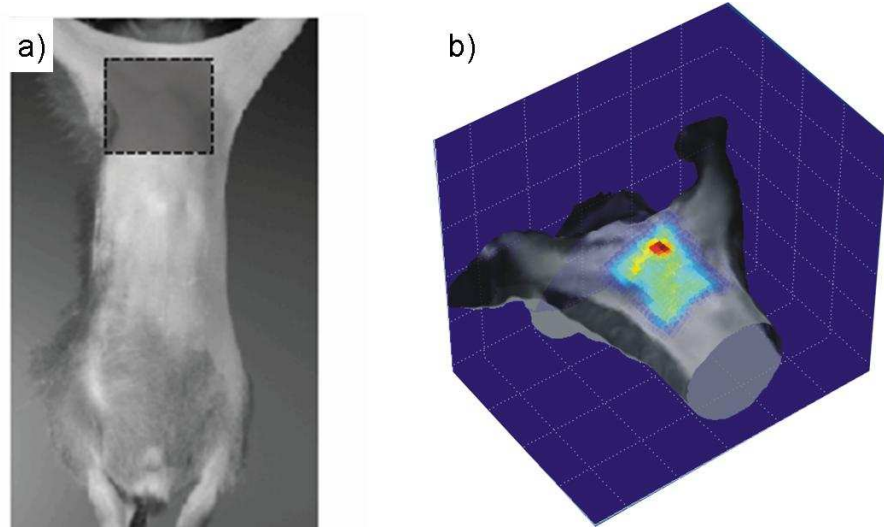


Figure 6.7: . a) flat image with marked detector area of 10×10 detectors c) mapping of the Normalized Born image onto the 3D surface of the body

The next step in the data treatment is the transformation of the finite case data into “infinite case” data according to the procedure described in section[3.3].

6.3.3 Inversion

The mesh is chosen with respect to the position of the targeted organ. The thymus is located in the upper anterior torso area so the corresponding region of interest is chosen and the volume is discretized into voxels for the formation of the mesh volume(see figure[6.8]). For our case the number of mesh voxels was chosen to be 4000 voxel elements.

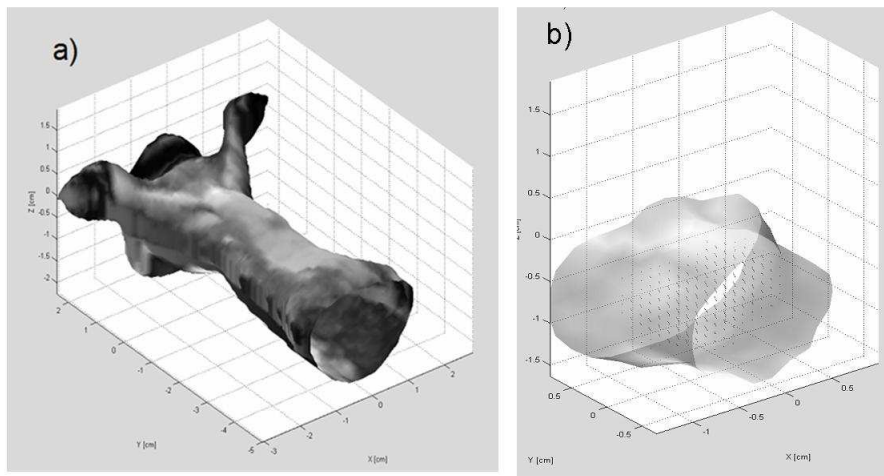
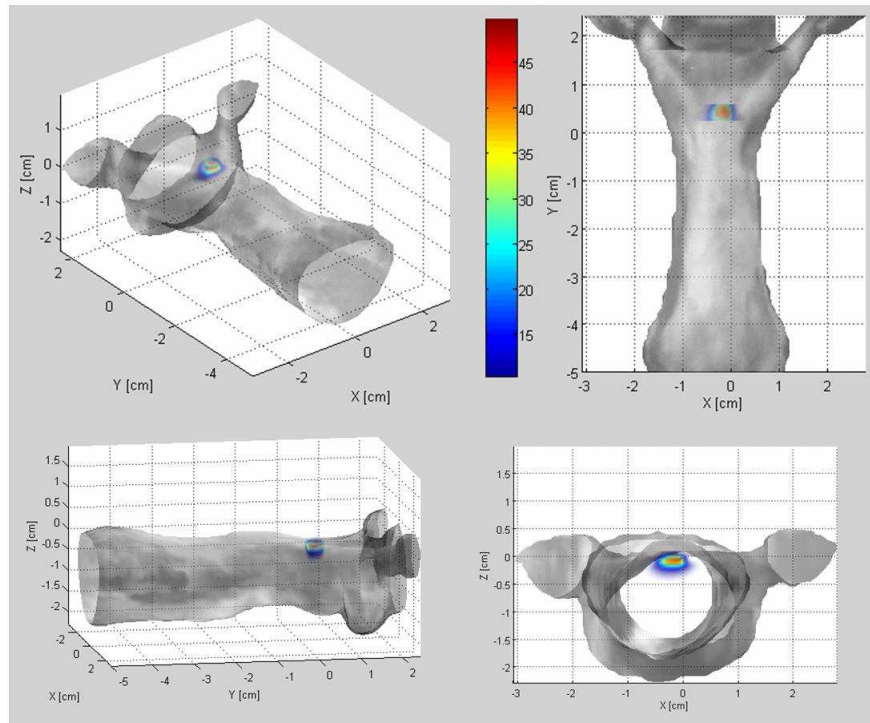


Figure 6.8: a) the three dimensional surface of the mouse b) the mesh volume that corresponds to the chest area

The normalized measurements from multiple projection are inverted with the Algebraic

Reconstruction Technique with positive restriction² in order to retrieve the spatial distribution of the fluorescent concentration. Typical inversion times for 10 iterations were in the order of 1 minute on a 3 GHz Pentium 4 Processor with mesh values ranging from 2600 to 4000 voxels.



Different views of the reconstructed concentration rendered together with the three dimensional geometry of the mouse body

Different views of the reconstructed concentration rendered together with the three dimensional geometry of the mouse body are shown in figure[6.3.3]. The shape of the reconstructed fluorescence map and its location inside the body strongly match with the anatomic characteristics of the thymus.

²positive restriction is introduced to secure no negative reconstructed values are obtained

Chapter 7

In vivo experiments and results

A variety of experiments were performed in both tissue like phantoms and mice. The methodology described in the previous chapter was applied to reconstructing the fluorescence signal either from CFSE filled tubes immersed in phantom media or GFP expressing T-lymphocytes in the case of CD2-GFP transgenic mice or GFP CLIP-170 microtubule “plus-end tracking” proteins in the case of the GFP CLIP-170 mice.

In the first section of this chapter, we present measurements on cylindrical high scattering phantom media containing fluorophores. The aim is to demonstrate the capacity of the system to quantify fluorescent signal from tubes containing different fluorophore concentrations inside scattering media. Next we present measurements on the lymphoid organs of both newborn and adult CD2-GFP mouse models. The cervical lymph nodes and the thymus were the primary targets. Fluorescence signal was also detected from the armpit lymph node in the case of the newborn mice. We also demonstrate the implications arising due to the strong autofluorescence when attempting to image the spleen. In another experiment we followed the fluorescence activity of the thymus over a period of the 5 first days of the life of a newborn mouse and we also monitored the cervical lymphnode at different time points.

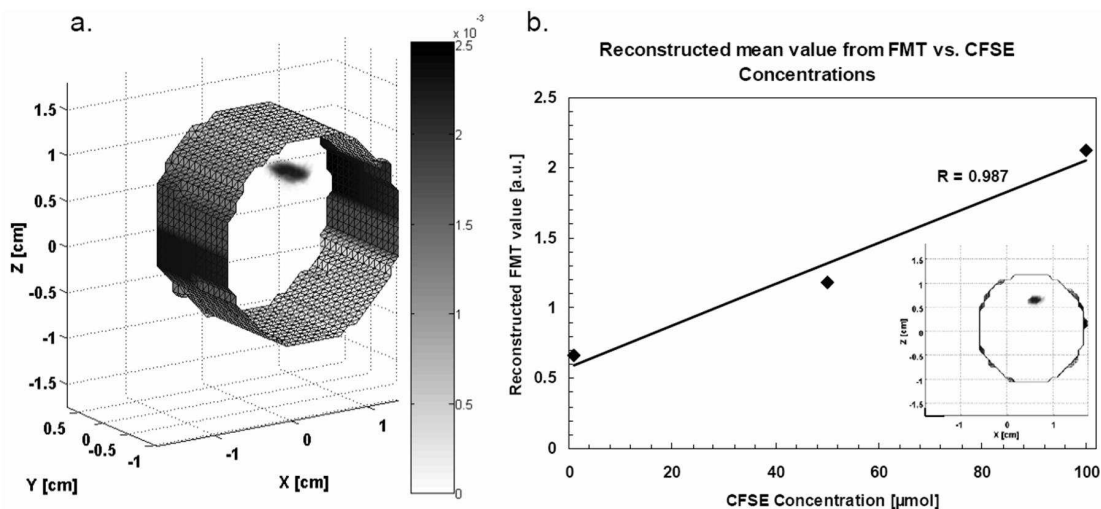
Finally, we present a study on measuring the fluorescent activity related to spermatogenesis by targeting the testes of GFP CLIP-170 mice. Tomographic imaging of fluorescence from the whole volume was peformed with measurements over a period of 10 days.

7.1 Calibration

In this experiment we studied phantom data as a means of calibrating our setup. To that end, measurements were performed on a hollow 20 mm Teflon cylinder with a wall thickness of 0.5 mm filled with an agarous solution with a reduced scattering coefficient $\mu'_s = 15 \text{ cm}^{-1}$ and an absorption coefficient $\mu_a = 1.4 \text{ cm}^{-1}$ in order to test the quality of the reconstructed surface and its impact in the 3D reconstruction of fluorophore concentration. Quantification measurements have been performed using borosilicate micro capillary tubes of 1.6 mm outer and 1.2 mm inner diameter containing different CFSE concentrations (1 μmol , 50 μmol and

$100 \mu\text{mol}$ solved in $1\times\text{PBS}$ solution with pH of 12) embedded in the phantom at a center to center distance from the capillary to the cylinder of 5 mm . The total number of projections were 4 at 0, 10, 20 and 30 degrees with respect to the incident sample position where the tube is in the closest position to the camera, for a source grid of 9 sources spanning from -8.5 mm to 8.5 mm in the x direction and -5.9 mm to 5.9 mm in the y direction in respect to the center of the image. The detection area used 18×12 detector grid covering an area of 2.00 cm^2 .

Results for the reconstructions are shown in Figure [7.1]. Fig. [7.1a] presents the 3D reconstructed surface of an agarous phantom with reconstructed fluorescence for the reflection mode. As can be seen in this figure, both the radius of the cylinder and the position of the capillary tube containing CFSE are retrieved with an accuracy of approximately 5% (please note that the center of rotation is not necessarily located at the origin). A cross section in the x-z plane is shown in the inset of Figure [7.1b].



a) 3D reconstructed surface of an agarous phantom with reconstructed fluorescence using a $50 \mu\text{mol}$ concentration of CFSE in $1\times\text{PBS}$ with a pH of 12. The micro capillary was placed in a center to center distance of $5 \pm 0.05\text{mm}$ in respect to the center of the phantom, b) reconstructed mean fluorescence intensity values achieved with the FMT system vs. CFSE concentration in the micro capillary tube of the agarous phantom ($1\mu\text{mol}$, $50\mu\text{mol}$, $100\mu\text{mol}$). (inset shows cross section of the reconstructed fluorescence according to the values given in a).

The results for the quantification are shown in Fig. [7.1b] where reconstructed mean fluorescence intensity values achieved with the FMT system vs. CFSE concentration in the micro capillary tube of the agarous phantom are presented. As can be inferred from this figure, the FMT reconstructed values can be calibrated to reflect actual concentration of CFSE. It must be noted that this type of calibration has to be performed for each fluorophore under study if one intends to represent the measurements in terms of fluorophore concentration. Also, even though this quantification study has been performed in a homogeneous phantom with optical properties similar to those of mice in the GFP excitation range, we would like to state that

thorough studies of the effect of inhomogeneities present have been presented [86] proving that the “normalized Born” approach used here is extremely robust, even in highly heterogeneous media.

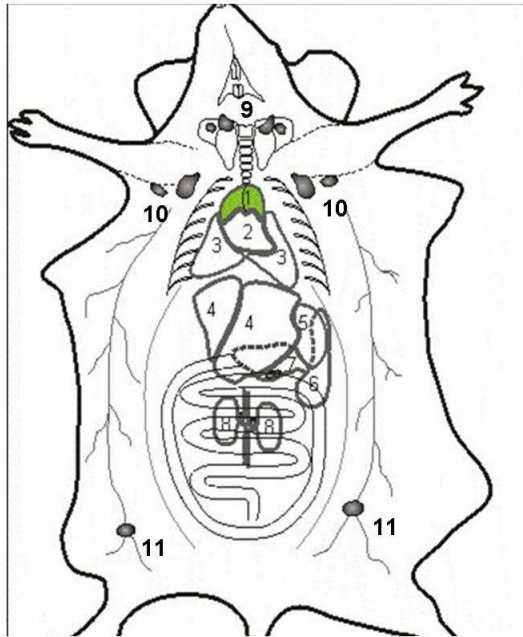


Figure 7.1: Picture of an opened mouse showing some of the lymphoid organs along with some of the main body organs. 1) thymus, 2) heart, 3) lung, 4) liver, 5) stomach, 6) spleen, 7) pancreas, 8) kidneys, 9) cervical lymph nodes, 10) axillary lymph nodes, 11) inguinal lymph nodes.

7.2 Imaging of the lymphoid organs

We chose to classify the T-cell imaging experiments into two categories depending the age of the subject. Apart from the treatment requirements, the main difference between the two kinds of subjects is that newborn mice exhibit less tissue absorption. In newborns, their small size and the absence of a thick fat layer beneath the skin results in less absorption and thus the signal to background ratios are bigger. It should be also stated that imaging in the visible range of spectrum results in large autofluorescence signal in the background. There are cases such as the thymus and the lymph nodes where the fluorescent signal originating from the targeted organ is greater than the background autofluorescence. However in the case of the spleen the levels of GFP fluorescence and autofluorescence limit the ability in reconstructing the targeted organ. Figure 7.1 is a picture of an opened mouse where the positions of the some lymphoid organs together with some of the main body organs are shown.

7.2.1 Adult mouse imaging

Since our mouse models contain GFP-expressing T cells we focused our study in imaging the organs on which the T-cells are residing, the thymus, the lymph nodes and the spleen in an

initial attempt to assess the systems ability in measuring fluorescence activity from cells in the lymphatic system. The measurements were performed in reflection mode with the ventral side of the mouse facing the camera. This geometry was found to be more suitable for detecting signals originating from shallow regions, as in the case of the targeted organs (thymus, lymphnodes, spleen). The number of sources were chosen during each experiment by estimating where the organ/organs under study were expected to be, taking into account the anatomy changes due to the subjects positioning. The desirable resolution and the duration of the whole procedure while the subject is under anesthesia were also taken into account.

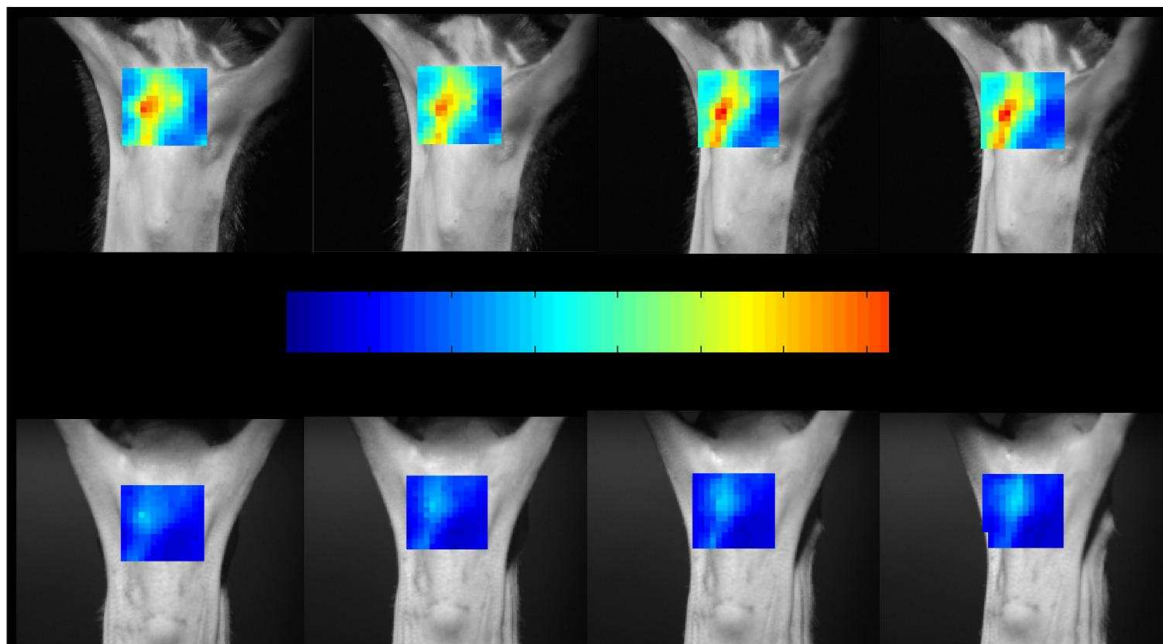


Figure 7.2: Normalized Born data of a CD2-GFP mouse expressing GFP in the T cells vs. a b10 control mouse for four different angle steps overlaid on the corresponding white light images

7.2.1.1 Thymus imaging: comparison with a control mouse

Taking into account the strong absorption of light in the visible spectrum, the thymus of 4 – 6 week old mouse containing $\sim 10^8$ T cells and located 4 mm deep beneath the skin was our primary target. A tomographic image of the thymus was presented in the previous chapter as an example to following the steps of the reconstruction process. In all the cases presented here the measurements from the GFP animals are compared with the measurements on a control mouse. For the case of the example of the previous chapter, measurements with the same settings were performed in a control mouse and the comparison in terms of the signal strength are shown in figure[7.2]. The signal at the thymus in the GFP-positive mouse is high when compared with the one of the control mouse. The origin of the signal for the case of the control mouse is tissue autofluorescence.

While in the example of the previous chapter, the measurements included angular projections, we show here fluorescence reconstruction when projections are provided by a two dimensional laser scanning. The measurements were performed 4 week old male mice. For both the transgenic and the control mouse the thymus scan comprised of 5×5 sources in steps of 2 mm . The body area scanned was the front part of the mouse body at the level of the thymus. For the reconstruction, 20×20 detectors were used covering an area of $12 \times 12\text{ mm}^2$. Typical Normalized Born data obtained from the thymus of a transgenic and a control mouse are shown in Figures a and b respectively. The figures show Normalized Born data averaged over all sources overlaid on a white light image of the mouse. The dimensions of the overlaid frame match those of the selected detection area.

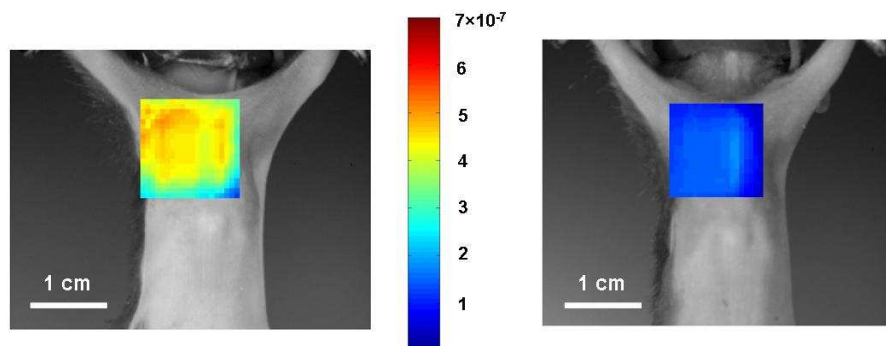


Figure 7.3: Normalized Born data from the thymic area overlaid on the white light image of a) CD2-GFP transgenic mouse and b) a B10 control mouse obtained after averaging all sources for an x-y source scanning

Typical Normalized Born data such as those presented in Figures 2 serve as forward data for the reconstruction of the 3D maps of the fluorescence activity according to the procedure of Chapter 6. In figure[7.4] the 3D reconstruction of a thymus is presented for the case of a laser scan.

In the chest area, apart of the thymus there are also two lymph nodes located in contact with the thymus. These nodes which are also known as “Mediastenial nodes” have a very small size compared with the thymus and they contain two orders of magnitude less T cells. Although the resolution of the setup is not enough for the visualization of these nodes, however their signal is added to the reconstructed intensity. In figure (7.4), the reconstructed object located on the left side of the thymus is an artifact caused by the concave shape of the mouses chest wall on that area, which we present to exemplify the type of artifacts expected in non-contact measurements. Artifacts do not always arise but are very common in all optical tomography approaches.

While running the reconstruction algorithms for the case of the control mouse and applying the same parameters as for the case of the GFP mouse, we obtained 4 times lower signal, corresponding to the skin autofluorescence. At the end of the measurements the mouse was

sacrificed and the exact number of T cells present in the targeted organ was determined with flow cytometry analysis and correlated with the FMT results. The thymus of this mouse was found to have 3.2×10^7 GFP positive cells.

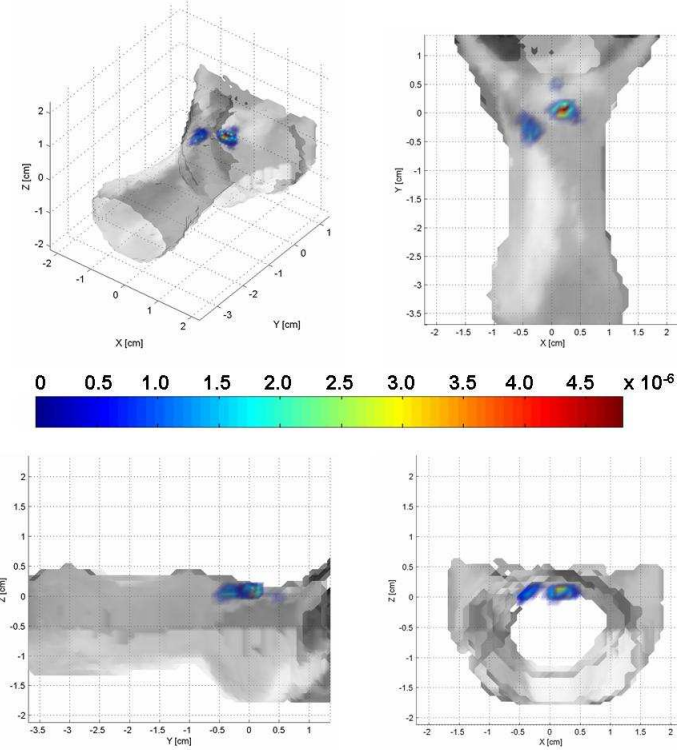


Figure 7.4: Different views of a 3D reconstruction of GFP activity in the thymus of a CD2-GFP transgenic mouse *in vivo*. The reconstructed signal is rendered to the 3 dimensional surface of the animal. An orthographic view of the tomographic image is shown in a). b) c) d) show the coronial, the axial and the sagittal view of the reconstructed thymus rendered to the 3D surface.

7.2.1.2 Cervical lymph nodes

The cervical lymph nodes (see figure[7.1]) are located in the neck, symmetrically placed with respect with the head tail axis of the mouse body. The cervical lymph nodes are excellent targets due to their superficial position. We present here an experiment on a female 4 week old transgenic mouse. Figure[7.5a] shows the white light image of the mouse placed horizontally with its ventral side facing the camera on the stage. The measurements were performed in the horizontal setup in reflection geometry. For laser scanning we used a 4×9 source grid in steps of 1 mm in the x direction and in steps of 2.5 mm in the y direction. The average of the Normalized Born data of the mouse is shown overlaid on the zoomed area of the neck of the mouse(see figure[7.5b]).

The normalized Born data show, that the signal is originating from three lymph node regions. The number of the cervical lymph nodes generally varies between subjects. We have reported cases of mice exhibiting different numbers of nodes at each side of the neck. Similar to the case of the “Mediastenial nodes” discussed in the previous section, when the nodes of each side are closely placed the tomographic reconstruction cannot resolve the structure of each individual node. However the fluorescence signal from all the nodes residing in the targeted area is added and reconstructed by the tomographic algorithm, and can be correlated with the results of the FACS analysis. The number of the nodes present at each mouse is derived after sacrificing the animal at the end of the tomographic measurements.

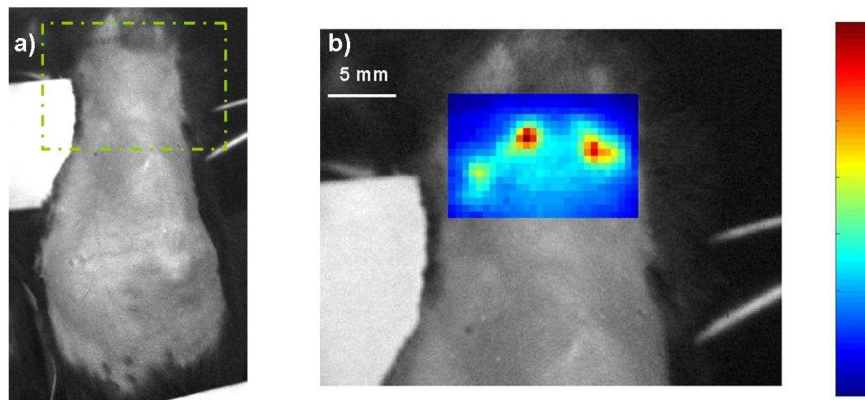


Figure 7.5: a) white light image of the animal with his ventral side facing the camera. The dashed frame shows the targeted body area for imaging the cervical lymph nodes. b) Normalized Born image of the targeted organ averaged in all source positions.

For the reconstruction process example the detector area is comprised of 28×18 detectors covering an area of $14 \times 9 \text{ mm}^2$. Finally a $14 \times 9 \times 3 \text{ mm}^3$ mesh volume was chosen discretized into 27000 voxels. The tomographic images of the lymph nodes of two mice rendered to the white light image are presented in figure [7.6].

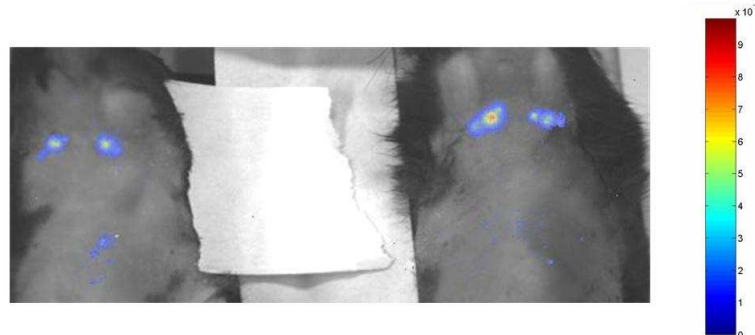


Figure 7.6: Reconstructed fluorescent signal from the GFP expressing T cells inside the cervical lymph nodes rendered into the white light image of two mice

Figure[7.6] presents an example of monitoring the fluorescence activity in two mice simulta-

neously portraying the capacity of the horizontal setup for the performance of high throughput measurements.

7.2.1.3 Spleen imaging

Spleen is a potential target for fluorescence measurements, given the large number of T cells that it contains ($\sim 10^7$ cells) and its superficial position. However, imaging of the spleen is limited due to its high content of blood and its location among organs that exhibit strong autofluorescence.

The positioning of the mouse for performing measurements on the spleen is shown in figure[7.7a]. The mouse is lying on the stage with its side in the field of view of the camera. From figure[7.7b] showing the normalized Born measurement overlaid on the white light image of the mouse, we see that the signal detected is high. However, when measuring a control mouse under the same experimental parameters, we detected similar signal levels due to the autofluorescence of the tissue. We then performed a measurement on an open transgenic mouse in order to locate the origin of the fluorescence signal. The measurements showed that the fluorescent light is not originating only from the spleen, but the surrounding organs exhibit strong fluorescence as well (see figure[7.7c]).

Tissue autofluorescence is one of the main problems when imaging in the visible spectrum. Tissue autofluorescence appears as a uniform background signal on the recorded images, especially in the reflection geometry, and compromises the resolution and detection limit of the tomographic method.

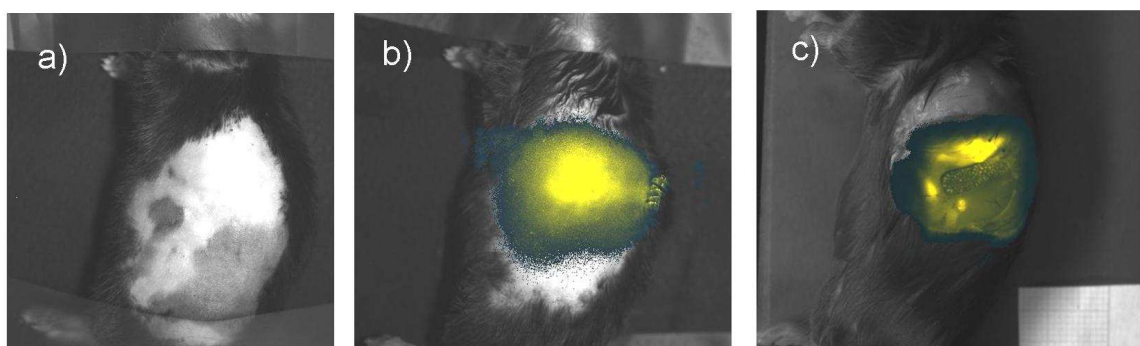


Figure 7.7: a) the white light of the mouse position for targeting the spleen area, b) the normalized born measurement at the spleen area, c) normalized Born measurement of the spleen area in an open mouse

It should be stated that in the results of the above sections (thymus and lymph node imaging), even though autofluorescence was present, the fluorescent signal emitted from the targeted organs was higher and the tomographic images were not significantly affected, reconstructing the GFP concentration.

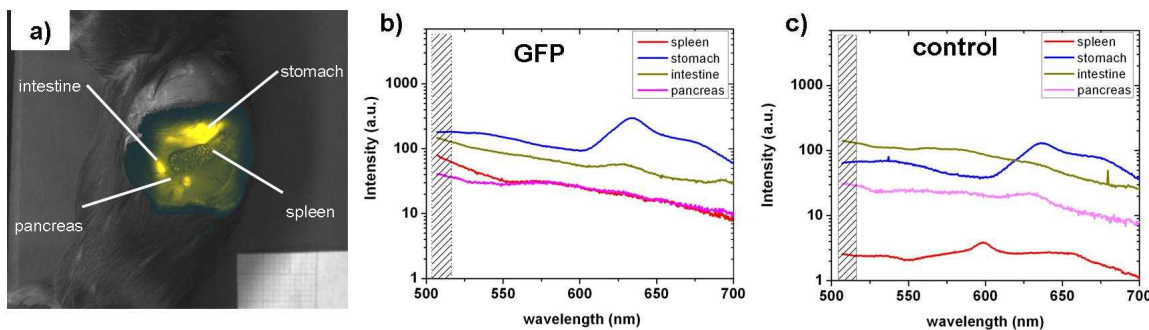


Figure 7.8: a) normalized Born measurement of the spleen area in an open mouse. Spectra of several of the organs surrounding the spleen after exciting with the 458 nm line for the case of a GFP b) and a control c) animal. The frames on the graphs correspond to the profile of the fluorescence filter used for the tomographic measurements

In figure[7.8a] the different organs surrounding the spleen are indicated. We see that the T cells areas inside the spleen exhibit strong signal fluorescence appearing as small bright dots among a high absorbing blood background. The surrounding tissue exhibits strong autofluorescence, as can be seen in figure[7.8a].

We thoroughly examined the spleen area by opening the mouse and measuring a spectrum of each organ of the spleen area and the results are presented in figures[7.8b] and [7.8c]. In order to quantify the fluorescence of the organs of the spleen area, we measured their emission spectra. Measurements were performed in an open mouse in-vivo and apart from the spleen, we measured the stomach, the intestine and the pancreas. The results are presented in figures[7.8b] and [7.8c] for the case of a GFP transgenic and a control mouse respectively. We notice that the signal from the spleen of the GFP mouse is bigger than the signal from the control, as expected. However the autofluorescence of the surrounding organs is high and comparable with the GFP fluorescence of the T cell areas (see figure[7.8b]).

The presence of the autofluorescence of the surrounding tissue results in small contrast in imaging the spleen. In addition the autofluorescence also adds to the autofluorescence noise.

7.3 Newborn imaging

Measurements on newborn mice offer advantages in terms of the signal strength detected. In mice of few days old, tissue absorption is small and thus the signal to noise ratios achieved are greater than in the case of the adult mice. By performing tomographic measurements in different time points we can monitor the growth of the population of the residing cells over time.

7.3.1 Thymus monitoring

In this experiment we monitored the progression of the T cell population of the thymus. Figure [7.9a] shows a white light image of the mouse stage with two 4 days old male mice (the GFP positive mouse is on the left, the control mouse is on the right).

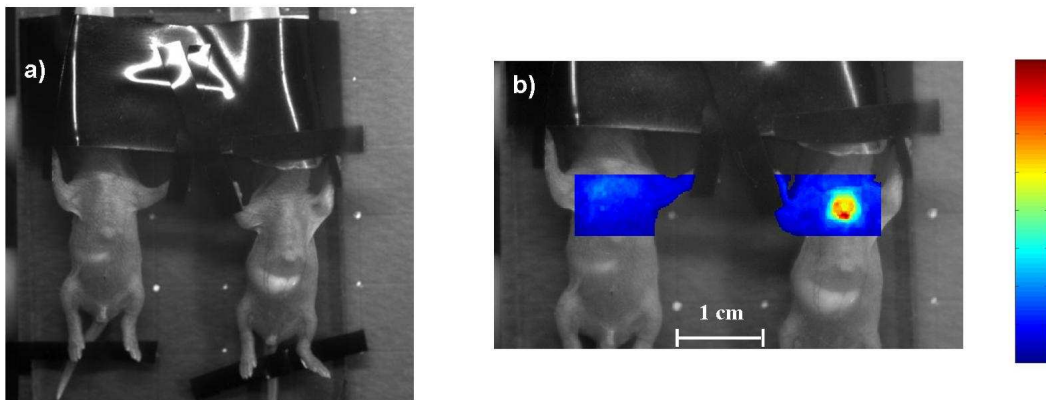


Figure 7.9: a) White light image of the setup stage with two newborn mice. b) Direct comparison of the normalized Born intensity between a control (left) and a GFP transgenic(left) mouse

The advantages of multisubject tomographic imaging have been analyzed in the instrumentation chapter; apart from the capacity to perform high throughput measurements, multisubject imaging minimizes the differences in the experimental conditions when comparing different subjects. Since the size of newborn mice is much smaller than that of the adult, the stage was raised to a higher position (see figure[7.6] and compare with figure[7.5a]). We targeted the upper body area in order to measure the GFP signal originating from the thymus.

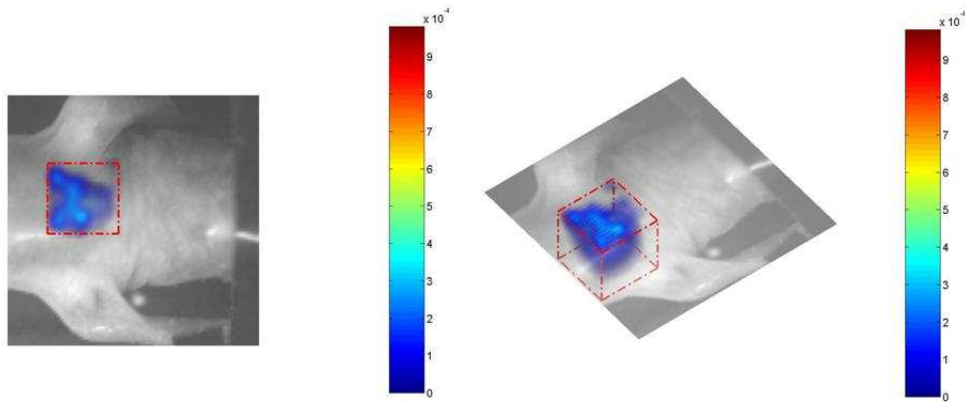


Figure 7.10: Reconstructed thymus rendered into the white light image of the mouse

A scanning grid of 3×8 sources in steps of 1 mm in the x axis and 2 mm in the y axis was applied on each mouse. The Normalized Born data averaged in all source positions are shown in figure[7.9b]. Strong fluorescense signal is emerging from the thymus area of the transgenic mouse while the signal of the control is due to tissue autofluorescence. For the reconstruction

we chose a 14×20 detector grid covering an area of $7 \times 10 \text{ mm}^2$ while the mesh had a volume of $7 \times 10 \times 5 \text{ mm}^3$ discretized into 36000 voxels. Figure[7.10] shows the reconstruction of the thymus rendered to the white light image of the mouse. The shape of the thymus is reconstructed while reconstruction artifacts are located mainly in the edges of the mesh volume.

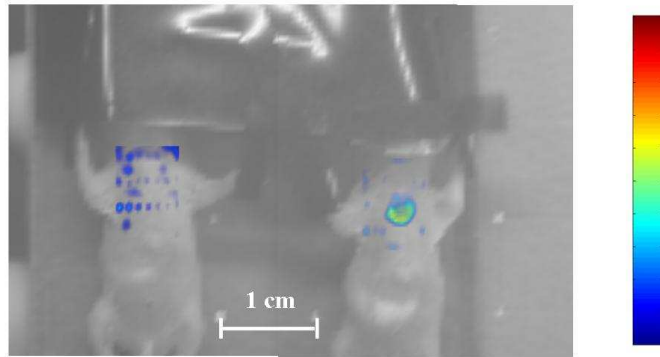


Figure 7.11: Tomographic image of the fluorescence signal originating from the thymic area for the case of a control(left) and a GFP mouse(right) .

Multi subject tomography offers the ability to compare the fluorescence signal at the level of the reconstructed data. When running the tomographic algorithms with the identical parameters direct comparison of between different subjects can be performed. In the experiment presented here we chose to compare a transgenic animal against a control one. Note that tomographic images of different transgenic animals can also be extracted and compared. In figure[7.11] the reconstructed data from the control mouse are artifacts. By calculating the mean value of the reconstructed signal for each mouse of this experiment we can quantify the difference in fluorescence activity originating from both mice. We found that the GFP signal is one order of magnitude greater than the control when selecting the same regions of interest.

We performed repetitive measurements to monitor the thymus growth over the first 5 days after the birth of the mouse. Monitoring of the number of T cell residing inside thymus is performed by calculating the mean value of the reconstructed values at every time point. In order to account only for the reconstructed values of the thymus volume a region of interest is selected with respect to the thymus positioning inside the body. The calculation of the mean reconstructed value is performed within the region of interest selected. The values corresponding to the reconstructions of each day are plotted against the time points as shown in figure[7.12]. Figure[7.12] also shows images of the reconstructed thymus for each day rendered to the white light images of the subject. The white light images are calibrated to the same dimensions and present the growth of the animal body.

From the histogram we see that the fluorescence activity of the thymus is increasing the first 3 days of the life of the mouse. In mice, the thymus continues to develop for 3 to 4 weeks after birth [98]. By performing repetitive measurements over a period of many days monitoring

of thymus growth is feasible.

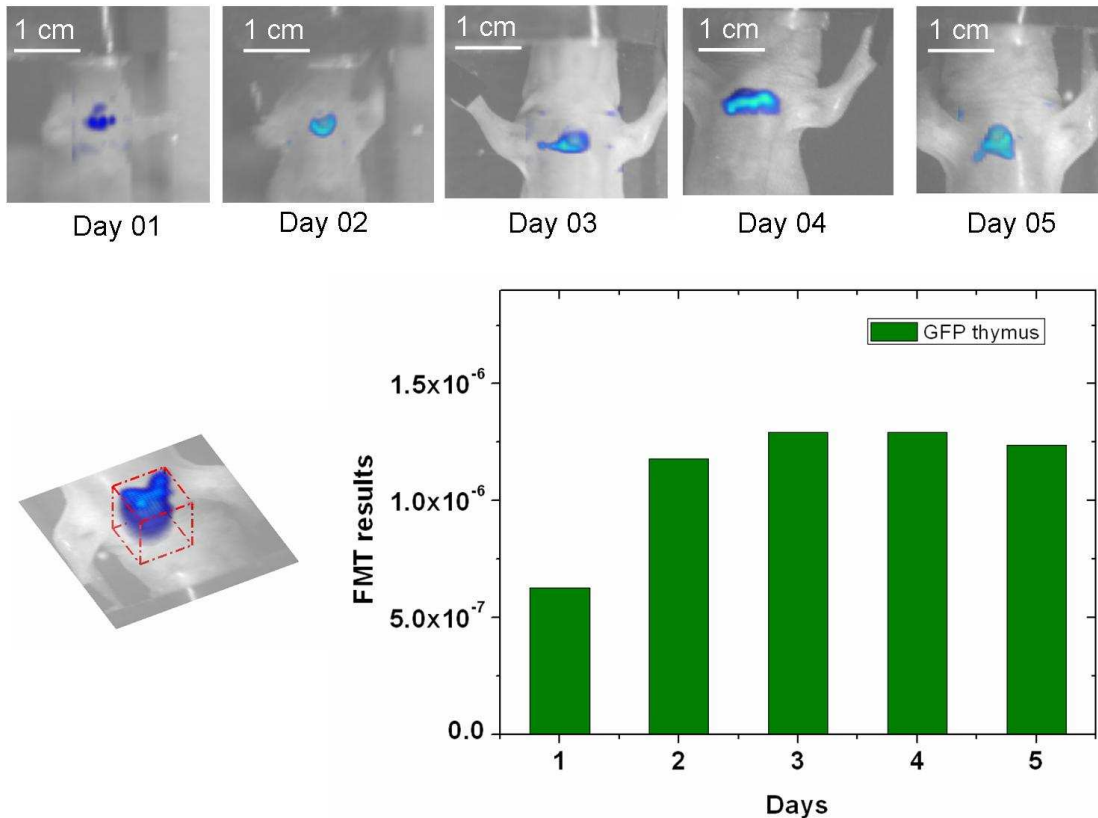


Figure 7.12: Repetitive measurements of the fluorescence signal from the thymus of a newborn mouse over a period of 5 days.

7.3.2 Cervical lymph nodes

The cervical lymph nodes were tomographically imaged in an attempt to explore the potential of monitoring the development of the lymph nodes in the first days of a mouse's life. The cervical nodes have small size and are closely placed in the neck area. We raised the stage to a height close to the camera so that the neck area is covering almost the whole field of view of the camera (see figure 7.13).

The effect of raising the stage higher greatly enhances the resolution by focusing only on the area where the cervical nodes are located. As stated earlier, the exact number of the cervical lymph nodes varies among different subjects. Generally, the cervical nodes are symmetrically placed with respect to the head-tail axis of the mouse body. We performed a 10×10 scan (in steps of 0.07 mm in both axis) at the neck area of a 15 days old GFP transgenic animal. Figure [7.14a] shows the Normalized Born averaged in all source positions. In the image, signal is originating from two main lymph node areas. The exact number of the nodes of each area cannot be resolved from the camera image, although it seems that each area contains at least 2 lymph nodes. The dissection analysis of this particular mouse showed that each of the large

lymph node areas consisted of 3 closely placed nodes. We detected one more lymphnode located low and left with respect to the left large lymph node area which is also visible in the camera image, although it exhibits much lower signal.

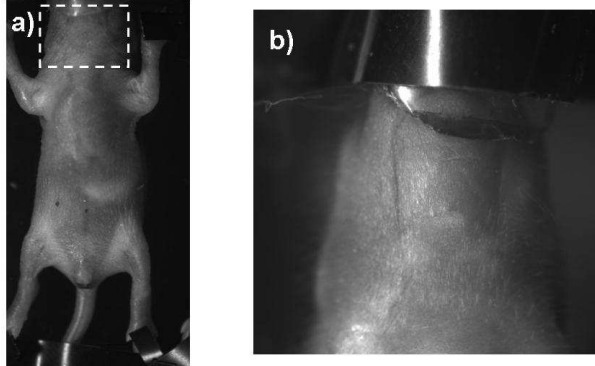


Figure 7.13: White light images of the mouse at different stage levels. The frame on a) indicates the neck area. In b) the neck area of the mouse is under the field of view of the camera

To quantify the fluorescence signal, we tomographically imaged the fluorescence activity of the neck area. For the reconstructions, a detector area comprised of 28×14 detectors and covering an area of $7 \times 14 \text{ mm}^2$ was used. The normalized Born image corresponding to the selected detector area is shown on figure[7.14]. The resolution of this image deteriorates the visualization of single nodes and the signal seems to originate from two large areas. The far left node is faintly visible. The reconstruction of the lymph nodes was performed after discretizing a volume of $7 \times 14 \times 3 \text{ mm}^3$ into a mesh volume of 27000 voxels. The tomographic image of the lymph nodes is presented in figure[7.14c]. The resolution of the tomographic technique cannot distinguish between closely placed nodes which is the case for the cervical lymph nodes. However the total fluorescence can be quantified within the resolution limits of the method.

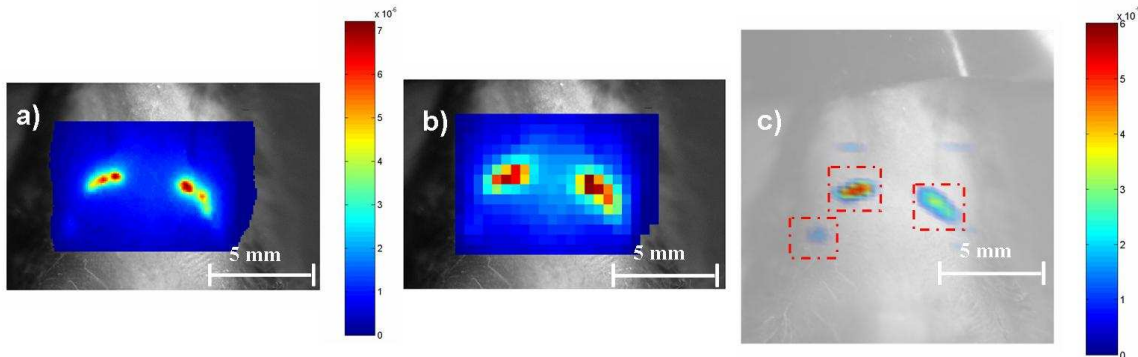


Figure 7.14: a)normalized Born image of the neck area of a GFP transgenic mouse. b) normalized born image of the detector grid used for the reconstructions. c) reconstructed image of the neck area. The small red dashed frames denote the reconstructed lymph node areas

We performed tomographic measurements on a mouse on the 8th, 10th and 15th day after its birth. The scanning grid and the detector area of the above mentioned experiment was applied

on all of the measurements. The results are shown in figure[7.15].

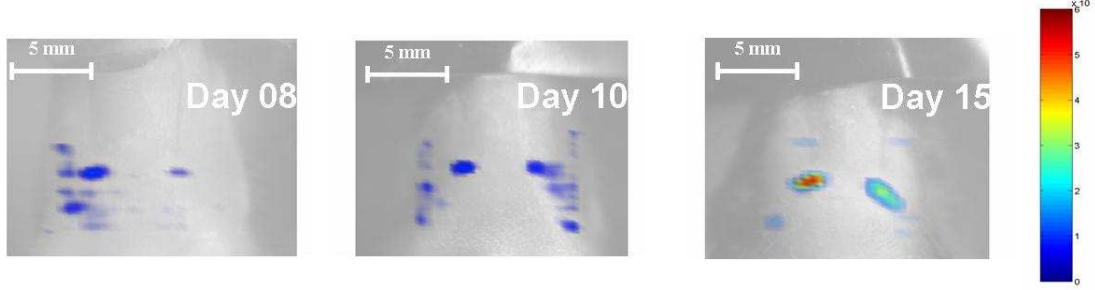


Figure 7.15: Tomographic images of the cervical lymph nodes of a mouse on various days.

The tomographic approach allows the quantitative monitoring of T cell population. We selected one region-of-interest corresponding to each lymph node area based on the resolution of the tomographic images. Then the mean value of the reconstructed values was calculated for each region and for each day and the results are plotted against time. The data show that the population of the T cells in the cervical nodes is increasing between day 8 and day 10.

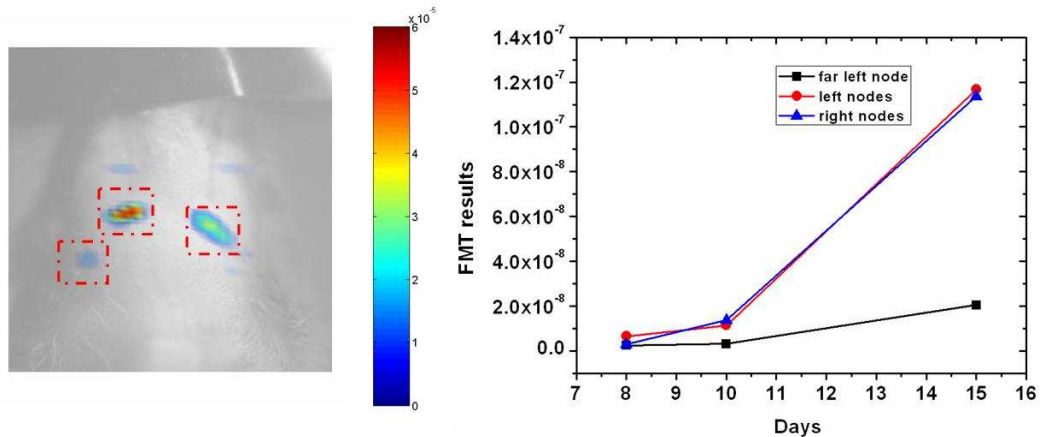


Figure 7.16: Selected regions of interest for the three node areas. Lymph node growth at various time points

The number of T cells in the cervical lymph nodes exhibit rapid changes in the first days of animal's life. Changes are induced from the immigration of T cells from the Thymus to the nodes, the homeostatic proliferation in the lymph node, the migration of T cells outside the lymph node and cell death. Tomographic imaging offers the capacity to quantify some of these biologic processes. For example, the migration of the cells from the thymus to the lymph nodes can be simultaneously imaged by scanning the upper body area of the mouse to cover both organs. Then parallel monitoring of the cell populations in the thymus and the lymph nodes the migration process can be quantified.

7.3.3 Armpit lymph node

Imaging of the armpit lymph nodes is an example of demonstrating the potential to use the “autofluorescence field” as described in section[6.2.1] in order to enhance the contrast between the targeted organ and the background autofluorescence. An example of the autofluorescence subtraction is shown in figure[7.17].

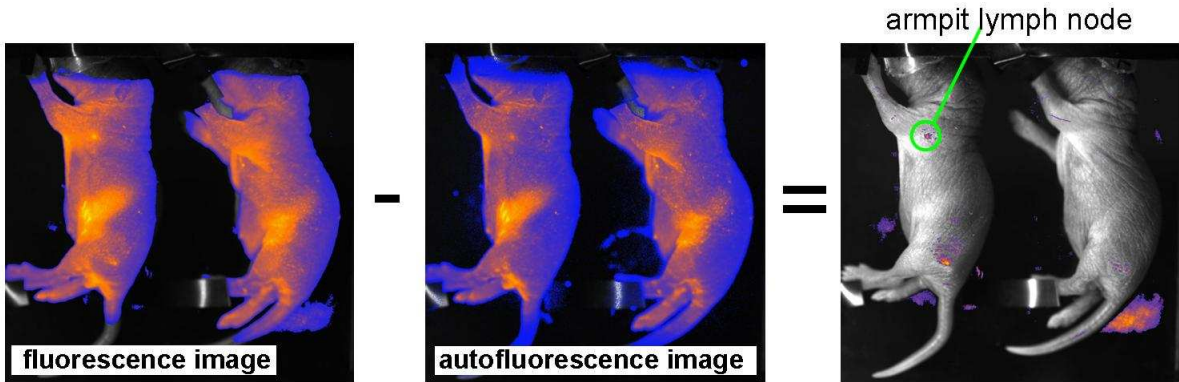


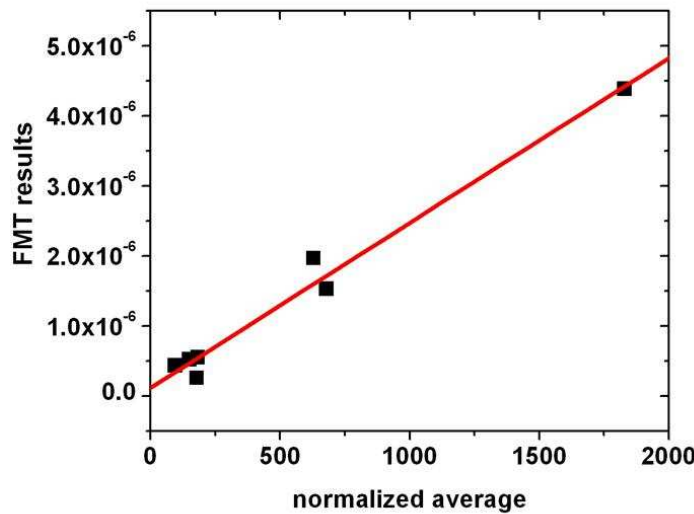
Figure 7.17: Subtraction of the autofluorescence measurement from the fluorescence measurement. The subtraction of the autofluorescence enhances the signal-to-noise ratio for the detection of the armpit lymph node

In this experiment 3 days old mice were placed with their side facing the camera and we performed a fast scanning over a large area in order to cover both mice. The fluorescence image corresponds to exciting with the 488 nm laser line and recording with the fluorescence filter ($510 \pm 5\text{ nm}$). The autofluorescence image was recorded with the same emission filter in front of the camera and exciting with the 458 nm laser line. Once the fluorescence and the autofluorescence image are recorded, the autofluorescence image is subtracted from the fluorescence image. The subtraction of the autofluorescence measurement permitted the clear visualization of the armpit lymph node.

With fast scanning information of the origin of the fluorescence signal is obtained in a fast manner. Then by extracting the autofluorescence measurement according with the method shown in figure[7.17] the region of pointing the source scan for the tomographic measurements revealed.

7.4 Quantification

Data obtained from both the FMT reconstructions and the FACS analysis were used to assess the quantification accuracy and the sensitivity of the system. From measurements performed on several subjects we correlated the values extracted by the tomographic method with the results of the FACS analysis. The FACS analysis is a cell sorting method for measuring the numbers of the fluorescing cells in terms of their fluorescence. The approach to correlate the FACS results with the FMT results was described in section[5.5].



Quantification data demonstrating the accuracy and sensitivity of the method. The data were obtained from tomographic measurements on the cervical lymph nodes of GFP mice. In the graph, the fluorescence molecular tomography reconstructed values are plotted against the numbers obtained from (FACS) analysis. The system was able to measure as low as 8×10^5 cells

In brief, we calculated the normalized average of the distribution of the positive events on the different levels of fluorescence expression. The data are presented in figure[7.4], where the FMT reconstructed values are plotted against the corresponding FACS values based on the analysis of section[7.4]. The x axis represents the normalized average of the distribution of the number of cells on their fluorescent strength. The FMT results strongly match the FACS results. In terms of sensitivity the smaller number of cells detected was found to be 8×10^5 cells which also represents the smaller normalized average value calculated.

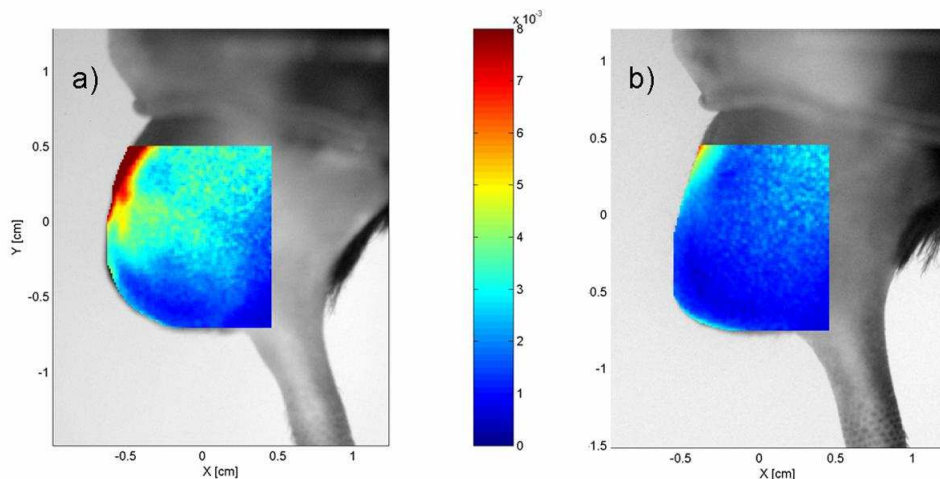
7.5 Testis Imaging

We performed tomographic measurements on the testis of GFP CLIP-170 mice in order to explore the potential of the optical tomographer to image the levels of expressions of the CLIP-170 protein.

Experiments were carried out with twenty - week old male CLIP170GFPki transgenic mice and seventeen week old C57BL6 control mice. In order to expose the testis area of the body we placed the mouse in a plastic falcon tube whose bottom was open. The testicles were exposed as the hind region of the mouse extrudes and pushes downward (see figure[6.1b]). In order to expose only the testis area, the urine and the two hind legs were left within the hollow falcon tube. The GFP signal is expected to originate from the whole testis area and thus the transmission geometry was chosen. In transmission geometry fluorophore concentrations deeply seated inside tissue can be imaged which is the case of the CLIP-170 protein since it is located

in broad regions inside the testis. The measurements were performed with the first generation setup in a number of times in the course of several days (1 image per day for nine days). We reconstructed one image of fluorophore concentration per day.

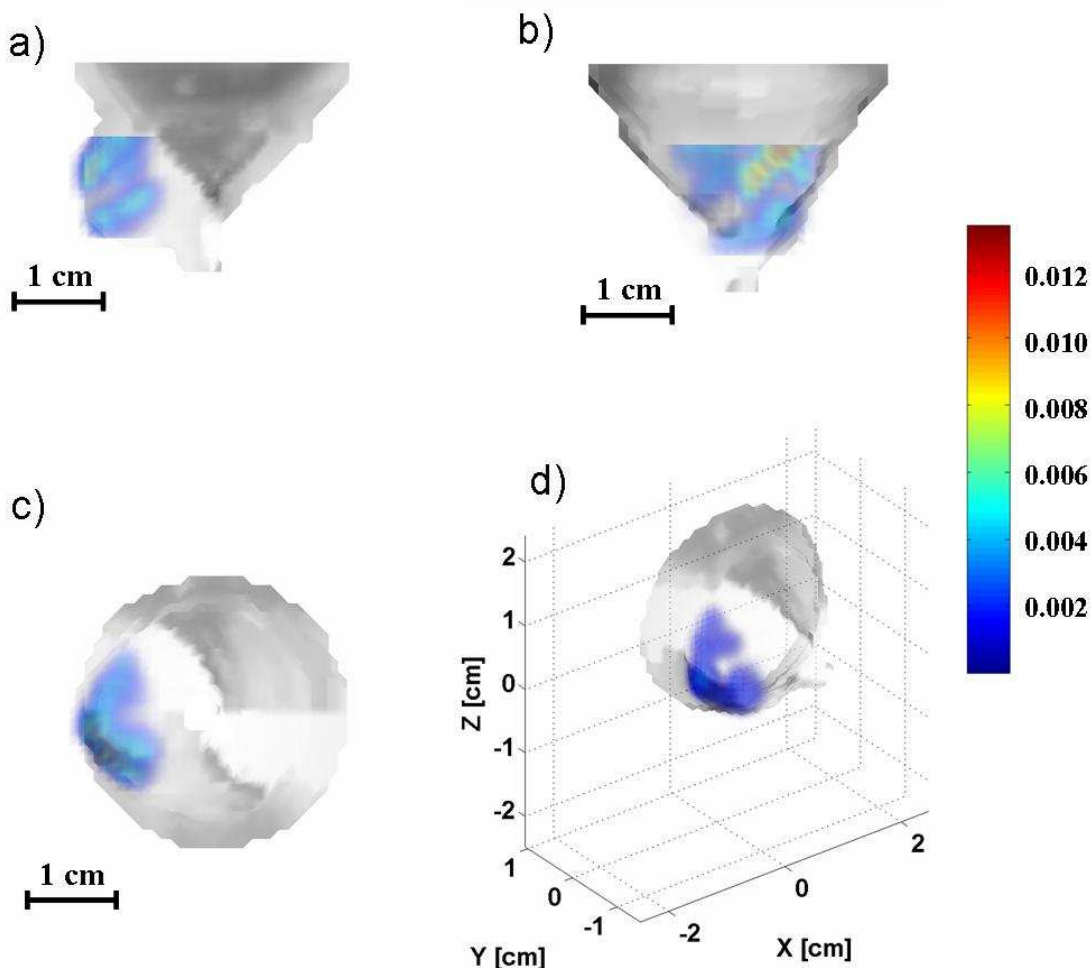
The first objective of this experiment was to detect fluorescence from the testis area. A C57BL6 mouse was used as a control. Typical Normalized Born data obtained from the testis of a transgenic and a control mouse are shown in figures[7.5a] and [7.5b] respectively. The sources were arranged in 5×5 grid with 1 mm step size. The figures show Normalized Born data averaged over all sources overlaid on a white light image of the mouse. The dimensions of the overlaid frame match those of the selected detection area. For the reconstruction of the fluorescence concentration the detector grid comprised of 18×24 detectors covering an area of $9 \times 12 \text{ mm}^2$.



Normalized Born data projected on the white light picture of a) clip170 GFP transgenic mouse and b) a C57BL6 control mouse obtained after averaging over all sources for an x-y source-scan.

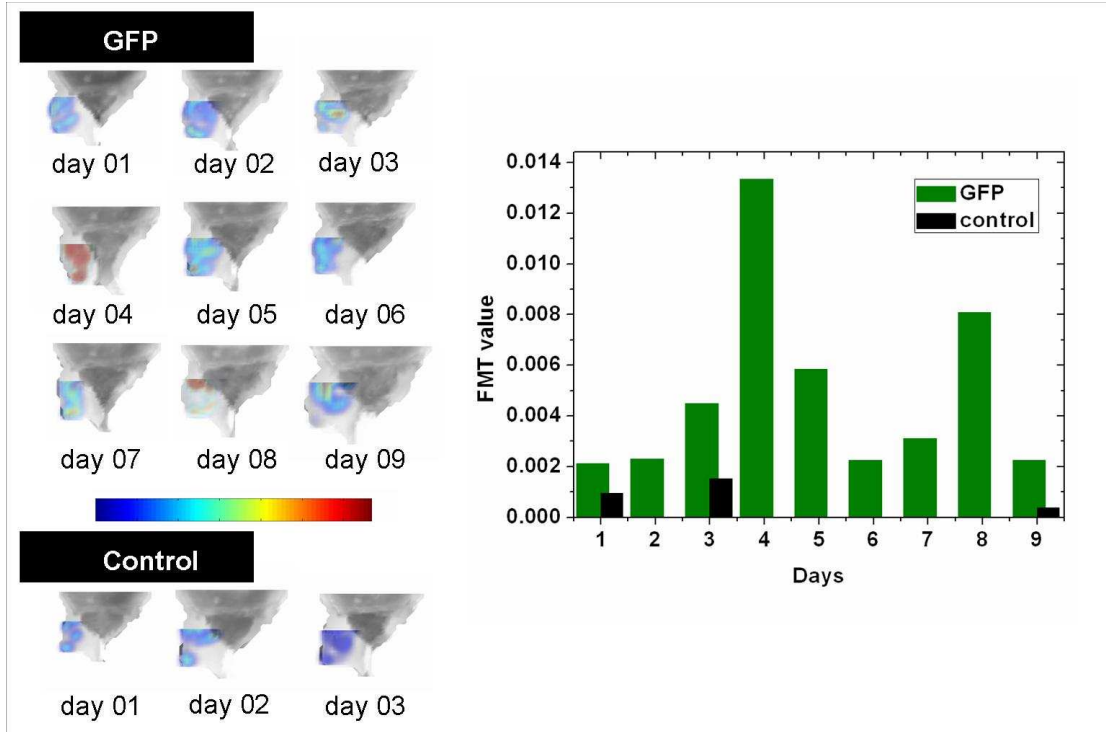
In Figure 7.5 a 3D reconstruction of GFP concentration located in the testis of a transgenic mouse is presented. Different views of the reconstructed concentration rendered together with the three dimensional geometry of the mouse body are shown. The tomographic reconstructions show that signal is originating form the whole testis area as expected. However, there are regions where the signal is stronger.

We followed the fluorescence activity of the GFP CLIP-170 protein over a period of nine days. The FMT value appearing in the figure 7.5 represents the mean reconstructed value from the tomographic images.



Different views of a 3D reconstruction of GFP activity in the testis of a clip170 GFP transgenic mouse *in vivo*. The reconstructed signal is rendered to the 3 dimensional surface of the testis region of the animal. a), b) and c) show the sagittal, coronal and axial views respectively. A general view of the reconstructed signal is shown in d)

Measurements on the control mouse were performed in days one, three and nine and in all cases the control mouse showed less signal than the transgenic mouse. The total expression of GFP molecule in the testes volume is varying during a period of 9 days. The tomographic images showed that the fluorescence activity inside the testis area is varying in waves and on days 4 and 8 the levels of expression are reaching maximum values. Not only the total expression levels vary through time but also the regions of the protein expression inside the testis, as can be seen from the tomographic images.



Monitoring of the GFP fluorescence activity over a period of 9 days. Tomographic reconstructions of the fluorescence activity for each day are shown. Control measurements are shown for the days 1,3 and 9.

The tomographic in-vivo results emphasize a role for CLIP-170 in formation of the spermatid manchette in accordance with published microscopic studies [94]. The results show that the expression of the GFP-CLIP-170 protein can be viewed with optical tomographic measurements and the progression of the total fluorescence activity can be monitored over time.

Chapter 8

Conclusions and future outlook

In this thesis the design, implementation and initial testing of a novel 3D imaging system suitable for in vivo non-contact fluorescence molecular tomography was presented. The system has been tested to tomographically image different fluorescence concentrations residing inside small animals. Experiments were performed on live transgenic mice that express the Green Fluorescent Protein (GFP) on various organs.

The unique versatility of the system lies in the fact that it operates in a non-contact geometry and thus it is highly advantageous in comparison to fiber-based systems or fixed geometry setups, since it provides the ability to acquire large data sets and number of projections as well as the ability to image arbitrary shapes without the need of “matching fluids” or imaging chambers. The non-contact approach is a significant step forward in terms of experimental simplicity and provides comfort to the targeted animal. The implementation of a non-contact experimental setup for imaging arbitrary geometries has been driven by theoretical advances in the modelling of the free space propagation of the diffuse light. The non-contact approach allowed the incorporation of a CCD camera as a detector for the collection of the signal. Thus, the recording of large data sets results in tomographic images of higher information content for probing fluorophores. In combination with an algorithm developed for modeling the free space light propagation, extracting the 3D surface of the targeted subject and inverting the data, as well as a user friendly interface, the system offers the non-contact experimental simplicity of common clinical tomographic approaches, such as X-Ray Computed Tomography. The system has the capacity to operate in both the reflection and the transmission geometry allowing measurements that cover a wide range of experimental requirements and models. Finally, the system can extract the three dimensional surface of the subject under study, which is essential for the correct modelling of the light propagation in order to solve the forward problem. The surface extraction allows the rendering of the reconstructed signal inside the geometry of the subject and its correlation with the anatomical characteristics of the specific subject.

The horizontal setup permits the simultaneous imaging of more than one subject as long as its size of those does not exceed the dimensions of the field of view of the camera. With this setup high throughput measurements for the simultaneous tomographic imaging of multiple subjects

is feasible. This allows the direct comparison of two subjects under identical experimental parameters. In this sense the multisubject tomography allowed the comparison of a GFP positive and a control mouse as well as the direct comparison of the strength of the fluorescent intensity originating from two transgenic mice.

A new theoretical approach was presented that simplifies the calculation of the forward problem of the tomographic algorithm. The method incorporates the camera images in order to transform the data at the boundary medium into data that would be obtained if no boundary was present. This permitted the use of the simple “infinite case” expressions resulting in faster computational times. For large data arrays (being this the case of CCD camera measurements) the use of the infinite case expressions offers advantages in terms of computational cost when reconstructing tomographic images. All the analyses for the extraction of tomographic images on this thesis were performed using this approach, and thus results were derived in fast manner.

The setup has been tested for the detection of fluorescence in transgenic mouse models in order to explore its capacity for the study of molecular processes in-vivo. Two mouse models have been measured. The first model was the CD2-GFP mouse line, in which all the T cells are expressing the GFP protein. Tomographic measurements were performed on several of the lymphoid organs such as the thymus, the lymph nodes and the spleen. The ages of the subjects varied, covering a range from few days up to few months. In particular, measurements on newborn mice have been performed aiming to monitor the seeding of T cells from the thymus to peripheral lymphoid organs during the first days of the mouse’s life. In the adult mice the measurements on the lymphoid organs were performed to explore the potential of applying the tomographic approach for Immunological studies. The second was the GFP CLIP-170 mouse model expressing GFP in the testis. In this model the aim was to study the GFP expression over time and correlate it with the spermatogenesis process.

For the case of the GFP-tagged T cell imaging, experiments were performed in the reflection geometry due to the superficial position of the targeted organs. We reconstructed fluorescence activity from the thymus and the cervical lymph nodes. Measurements were also taken in the spleen area, but the high content of blood resulted in poor contrast between the signal from the spleen and the autofluorescence signal of the surrounding organs. The quantification of this method has also been performed, by first imaging the fluorescence activity from the targeted organ and then correlating the reconstructed intensities with values obtained after sacrificing the animal and measuring the actual number of fluorescent cells by flow cytometry. Flow cytometry is a precise technique that differentiates cells according to their fluorescent intensity and thus was used to validate the tomographic results. The relation between the reconstructed data and the number of cells present in the cervical lymph nodes follows a linear curve and the minimum number of cells reconstructed was 9×10^5 cells.

Optical tomography has the capacity to follow biological processes during time. With repetitive imaging, following of the protein activity within its biological context is feasible. Monitoring of the fluorescence intensity has been performed for the case of the newborn mice. We

followed the thymus growth over the period of the first 5 days after the birth of the mouse. The results show that the cell population is increasing during the first 3 postnatal days. Repetitive measurements performed from day 8 to day 15 on the cervical lymph nodes showed growth in terms of cell population.

In the case of the GFP CLIP-170 imaging in the testis, measurements were performed in the transmission geometry. Fluorescence from the testis of the transgenic mouse has been detected when compared with measurements on a control mouse. We monitored the fluorescence activity from the testis of the same animal over a period of nine days and we reported changes on the total fluorescence intensity from the whole testis volume.

Imaging in the visible spectrum is limited to large cell populations or in superficial or subcutaneously seated organs. Imaging at longer wavelengths, where tissue absorption is smaller would expand the capacity of the optical tomographic method in terms of signal-to-noise ratios and detection limit. We have performed preliminary measurements with CD2-DsRed transgenic animals and future work would include validating and expanding the findings of this work with further experiments on mice expressing DsRed in their T cells. Great efforts are being made in the area of biotechnology for the engineering of red-shifted proteins [99, 100, 101]. Recently, a monomeric far-red fluorescent protein named mPlum that fluoresces at 649 nm was created on the basis of the natural red fluorescent protein DsRed [102]. This would also allow the use the transillumination as the standard illumination geometry, further minimizing the excitation of the skin autofluorescence compared to the reflection mode. This fact can be altered by the expansion of the fluorescent protein palette to the red and the near infrared by developing new fluorescent probes.

One of the main problems of reflection imaging in the visible spectrum, besides strong absorption, is tissue autofluorescence. Tissue autofluorescence appears as a uniform background signal on the recorded images, especially in reflection measurements, and compromises the resolution and the detection limit of the tomographic method. Thus, the autofluorescence of tissue should be taken into account and several methods have been proposed for eliminating this effect [103, 104]. These include capturing images at different spectral windows using a multispectral approach and applying unmixing algorithms for the extraction of the targeted fluorescent signal [104, 105]. Adaptation of these methods would increase issues like the detection limit, the resolution and the contrast of our technique.

The setup could be improved by minimizing the time required for one full experiment by designing and automating a system for filter swapping and auto-focus zoom objectives as well as an x-y-positioning system that could enable the observation of various areas of interest. Furthermore, an improved system would incorporate a second imaging modality, with CT being the strongest candidate, for providing anatomical maps of the subject.

The system and method described are capable of operating at different excitation and emission wavelengths using the appropriate filters, making the detection of multiple fluorophores and fluorescing proteins feasible, thus increasing the number of biological processes that can be

targeted. Currently, we are implementing algorithms for unmixing the fluorescence obtained from multiple fluorophores and reconstructing the fluorescence data.

The non-contact optical tomographer implemented provides an invaluable experimental tool for biomedical research in several areas such as immunological studies, monitor of cancer growth after transplantation, etc. The system presented can be used in vast numbers of different experimental models, targeting different important biological processes and functions, as well as different types of diseases. Future studies may include real-time imaging of cell interactions and preferential migration or distribution of cells within the immune system as well as behavior of lymphocyte cells during the immune response. These experimental results show that the system is suitable for three-dimensional free space *in vivo* imaging of organs of the immune system and can be used to monitor processes that will reveal hidden aspects of the function of several important diseases. Non-contact imaging as described here is not limited to small animals. The utilization of non-contact technologies could facilitate more generic use of the technique with tissues of arbitrary boundaries. Therefore, the same instrument could be used for different target organs and imaging applications, although the technique today seems to be applicable only to instances where bodyhair does not obstruct measurements. The translation of non-contact optical tomography to clinical applications is straight-forward, opening new pathways of imaging disease and drug response *in vivo*.

Bibliography

- [1] V. Ntziachristos, J. Ripoll, L. Wang, and R. Weissleder. Looking and listening to light: the evolution of whole-body photonic imaging. *Nat. Biotechnol.*, 23:313 – 320, 2005.
- [2] R. Weissleder and U. Mahmood. Molecular imaging. *Radiology*, 219:316–333, 2001.
- [3] T. F. Massoud and S. S. Wang, Gambhir. Molecular imaging in living subjects: seeing fundamental biological processes in a new light. *Genes and Development*, 17:545 – 580, 2003.
- [4] R. Weissleder and V. Ntziachristos. Shedding light into live molecular targets. *Nat. Med.*, 9(1):123–128, 2003.
- [5] V. Ntziachristos, Yodh A. G., and B. Chance. Concurrent mri and diffuse optical tomography of breast after indocyanine green enhancement. *Proc. Natl. Acad. Sci.*, 97:2767–2772, 2000.
- [6] B. Pogue, S. Poplack, T. McBride, W. Wells, K. Osterman, and U. Osterberg. Hemoglobin imaging of breast tumors with near-infrared tomography. *Radiology*, 214:G05H, 2000.
- [7] A. Ishimaru. *Wave Propagation and Scattering in Random Media*, volume 1. Academic, New York, 1978.
- [8] M. S. Patterson, B. Chance, and B. C. Wilson. Time resolved reflectance and transmittance for the non-invasive measurement of tissue optical properties. *Appl. Opt.*, 28:2331–2336, 1989.
- [9] A. Yodh and B. Chance. Spectroscopy and imaging with diffusing light. *Phys. Today*, 48:38–40, March 1995.
- [10] B. Chance. Optical methods. *Annual Review of Biophysics and Biophysical Chemistry*, 20:1–28, 1991.
- [11] D. Boas, D. H. Brooks, E. L. Miller, C. A. DiMarzio, M. Kilmer, R. J. Gaudette, and Q. Zhang. Imaging the body with diffuse optical tomography. *IEEE Signal Processing Magazine*, 18:57–75, 2001.

- [12] J. P. Culver, T. Durduran, D. Furuya, C. Cheung, J. H. Greenberg, and A. G. Yodh. Diffuse optical tomography of cerebral blood flow, oxygenation and metabolism in rat during focal ischemia. *J. Cereb. Blood Flow Metab.*, 23:911 – 924, 2003.
- [13] V. Ntziachristos and B. Chance. Probing physiology and molecular function using optical imaging: applications to breast cancer. *Breast Cancer Res. Treat.*, 3:41–46, 2001.
- [14] D. J. Hawrysz and E. M. Sevick-Muraca. Developments toward diagnostic breast cancer imaging using near-infrared optical measurements and fluorescent contrast agents. *Neoplasia*, 2:388–417, 2000.
- [15] D. A. Benaron, S. R. Hintz, A. Villringer, D. Boas, A. Kleinschmidt, J. Frahm, C. Hirth, H. Obrig, J. C. van Houten, E. L. Kermit, W. F. Cheong, and D. K. Stevenson. Non-invasive functional imaging of human brain using light. *J Cereb Blood Flow Metab*, 20(3):469–77, 2000.
- [16] J. P. Culver, A. M. Siegel, J. J. Stott, and D. A. Boas. Volumetric diffuse optical tomography of brain activity. *OPt. Lett*, 28:2061 – 2063, 2003.
- [17] D. Axelrod. Total internal reflection fluorescence microscopy in cell biology. *Methods Enzymol*, 361:1–33, 2003.
- [18] F. R. Wouters, P. J. Verveer, and P. I. H. Bastiaens. Imaging biochemistry inside cells. *Trends in Cell Biol*, 11:203–211, 2001.
- [19] E. B. Brown, R. B. Campell, Y. Tsuzuki, L. Xu, P. Carmeliet, D. Fukumura, and R. K. Jain. In vivo measurement of gene expression, angiogenesis and physiological function in tumors using multiphoton laser scanning microscopy. *Nat. Med*, 7(7):864–868, 2001.
- [20] JM. Arbeit and R. Hirose. Murine mentors: transgenic and knockout models of surgical disease. *Ann Surg*, 229:21–40, 1999.
- [21] M. Bader. Transgenic animal models for neuropharmacology. *Rev Neurosci*, 11:27–36, 2000.
- [22] S.S. Thorgeirsson, V.M. Factor, and E.G. Snyderwine. Transgenic mouse models in carcinogenesis research and testing. *Toxicol Lett*, 112-113:553–555, 2000.
- [23] P.R. Contag, I.N. Olomu, D.K. Stevenson, and C.H. Contag. Bioluminescent indicators in living mammals. *Nat. Med*, 4:245–247, 1998.
- [24] T. J. Sweeney, V. Mailander, A. A. Tucker, A. B. Olomu, W. Zhang, Ya Cao, R. S. Negrin, and C. H. Contag. Visualizing the kinetics of tumor-cell clearance in living animals. *Proc Natl Acad Sci*, 96(21):12044–12049, 1999.

- [25] C.H. Contag and M.H. Bacmann. Advances in in-vivo bioluminescence imaging of gene expression. *Annu. Rev. Biomed. Eng.*, 4:235–260, 2002.
- [26] G. Alexandrakis, F.R. Rannou, and A.F. Chatzioannou. Tomographic bioluminescence imaging by use of a combined optical-pet (opet)system: a computer simulation feasibility. *Phys. Med. Biol.*, 50:4225–4241, 2005.
- [27] A.J. Chaudhari, F. Darvas, J.R. Badling, R.A. Moats, P.S. Conti, D.J. Smith, S.R. Cherry, and R.M. Leahy. Hyperspectral and multispectral bioluminescence optical tomography for small animal imaging. *Phys. Med. Biol.*, 50:5421–5441, 2005.
- [28] X. Gu, L. Zhang, L. Larcom, and H. Jiang. Three dimensional bioluminescence tomography with model-based reconstruction. *Opt. Exp.*, 12(17):3996–4000, 2004.
- [29] M. Yang, E. Baranov, P. Jiang, F. Sun, X. Li, L. Li, S. Hasegawa, M. Bouvet, M. Al-Tuwaijri, T. Chishima, H. Shimada, A.R. Moossa, S. Penman, and R.M. Hoffman. Whole-body optical imaging of green fluorescent protein-expressing tumors and metastases. *Proc. Natl. Acad. Sci.*, 97:1206–1211, 2000.
- [30] R. M. Hoffman. Green fluorescent protein imaging of tumour growth, metastasis, and angiogenesis in mouse models. *Lancet Oncol.*, 3:546–556, 2002.
- [31] M. Yang, E. Baranov, A. R. Moossa, S. Penman, and R.M. Hoffman. Visualizing gene expression by whole-body fluorescence imaging. *Proc. Natl. Acad. Sci.*, 97:12278–12282, 2000.
- [32] R. Weissleder, C. H. Tung, U. Mahmood, and A. Bogdanov. In vivo imaging of tumors with protease-activated near-infrared fluorescent probes. *Nat. Biotechnol.*, 17:375–378, 1999.
- [33] C. Bremer, C. Tung, and R. Weissleder. In vivo molecular target assessment of matrix metalloproteinase. *Nature Med.*, 7:743–748, 2001.
- [34] C.H. Tung, U Mahmood, S Bredow, and R Weissleder. In vivo imaging of proteolytic enzyme activity using a novel molecular reporter. *Cancer Research*, 60:4953–4958.
- [35] M. Chalfie, Y Tu, G. Euskirchen, W.W. Wrd, and D.C. Prasher. Green fluorescent protein as a marker for gene expression. *Science*, 263:802–805, 1994.
- [36] X. Ma V. Ntziachristos and B. Chance. Time-correlated single photon counting imager for simultaneous magnetic resonance and near-infrared mammography. *Rev. of Sci. Instr.*, 69:4221–4233, 1998.
- [37] B. Chance V. Ntziachristos and A. G. Yodh. Differential diffuse optical tomography. *Opt. Exp.*, 5:230–242, 1999.

- [38] S. R. Arridge. Optical tomography in medical imaging. *Topical review in Inverse Problems*, 15:R41–R93, 1999.
- [39] V. Ntziachristos, C. Tung, C. Bremer, and R. Weissleder. "Fluorescence molecular tomography resolves protease activity *in vivo*". *Nature Med*, 18:757–760, 2002.
- [40] V. Ntziachristos, C. Bremer, E. E. Graves, J. Ripoll, and R. Weissleder. In vivo tomographic imaging of near-infrared fluorescent probes. *Molecular Imaging*, 1:82 – 88, 2002.
- [41] G. Zacharakis, H. Kambara, H. Shih, J. Ripoll, J. Grimm, Y. Saeki, R. Weissleder, and V. Ntziachristos. Volumetric tomography of fluorescent proteins through small animals *in vivo*. *Proc. Natl. Ac. Sc*, 102(51):18252–18257, 2005.
- [42] J. Ripoll, R. B. Schulz, and V. Ntziachristos. Free-space propagation of diffuse light: Theory and experiments. *Phys. Rev. Lett*, 10:103901–1 – 103901–4, 2003.
- [43] E. E. Graves, J. P. Culver, J. Ripoll, R. Weissleder, and V. Ntziachristos. Singular-value analysis and optimization of experimental parameters in fluorescence molecular tomography. *J. Opt. Soc. Am. A*, 21:231 – 241, 2004.
- [44] J. Culver, V. Ntziachristos, M. Holboke, and A.G. Yodh. Optimization of optode arrangements for diffuse optical tomography: A singular value analysis. *Optics Letters*, 26(10):701–703, 2001.
- [45] R. B. Schulz, J. Ripoll, and V. Ntziachristos. Experimental fluorescence tomography of tissues with noncontact measurements. *IEEE Transactions on Medical Imaging*, 23(4), 2004.
- [46] R. B. Schulz, J. Ripoll, and V. Ntziachristos. Noncontact optical tomography of turbid media. *Opt. Lett*, 28(18):1701–1703, 2003.
- [47] AC Kak and M. Slaney. *Principles of Computerized tomographic imaging*. IEEE Press, New York, 1988.
- [48] S. Chandrasekhar. *Radiative transfer*. Oxford University Press, New York, 1960.
- [49] K. M. Case and P. F. Zweifel. *Linear Transport Theory*. Addison-Wesley, MA, 1967.
- [50] L. G. Henyey and J. L. Greenstein. Diffuse radiation in the galaxy. *AstroPhys. J*, 99:70–83, 1941.
- [51] B. J. Tromberg, N. Shah, R. Lanning, A. Cerussi, J. Espinoza, T. Phain, L. Svaasand, and J Butler. Non-invasive *in vivo* characterization of breast tumors using photon migration spectroscopy. *Neoplasia*, 2:26–40, 2000.

- [52] U. L. Osterberg B. W. Pogue H. Jiang, K. D. Paulsen and M. S. Patterson. Simultaneous reconstruction of optical absorption and scattering maps in turbid media from near-infrared frequency-domain data. *Opt. Lett.*, 20:2128–2130, 1995.
- [53] T. L. Troy, D. L. Page, and E. Sevick-Muraca. Optical properties of normal and diseased breast tissue: prognosis for optical mammography. *J. Biomed. Opt.*, 1:342–355, 1996.
- [54] K. Furutsu and Y. Yamada. Diffusion approximation for a dissipative random medium and the applications. *Phys. Rev. E*, 50, 1994.
- [55] R. Elaloui, R. Carminati, and J. J. Greffet. "Time-dependent transport through scattering media: from radiative transfer to diffusion". *J. Opt. A: Pure Appl. Opt.*, 4:S103–S108, 2002.
- [56] M. Xu, W. Cai, M. Lax, and R. R. Alfano. "Photon migration in turbid media using a cumulant approximation to radiative transfer". *Phys. Rev. E*, 65, 2002.
- [57] A. Ishimaru. Difference between Ishimaru's and Furutsu's theories on pulse propagation in discrete random media. *J. Opt. Soc. Am. A*, 1:506–509, 1984.
- [58] S. Ito. Comparison of diffusion theories for optical pulse waves propagated in discrete random media. *J. Opt. Soc. Am. A*, 1:502–505, 1984.
- [59] I. Freund, M. Kaveh, and M. Rosenbluh. Dynamic multiple scattering: ballistic photons and the breakdown of the photon-diffusion approximation. *Phys. Rev. Lett.*, 60:1130–1133, 1988.
- [60] K. M. Yoo, F. Liu, and R. R. Alfano. When does the diffusion approximation fail to describe photon transport in random media? *Phys. Rev. Lett.*, 64:2647–2650, 1990.
- [61] T. G. Papazoglou, W. Q. Liu, A. Vasiliou, R. Grassmel, R. Papagiannakis, and C Fotakis. "Limitations of diffusion approximation in describing femtosecond laser transillumination of highly scattering media of biological significance". *Appl. Phys. Lett.*, 67:3712–3714, 1995.
- [62] A. H. Hielscher, R. E. Alcouffe, and R. L. Barbour. "Comparison of finite-difference transport and diffusion calculations for photon migration in homogeneous and heterogeneous tissues". *Phys. Med. Biol.*, 43:1285–1302, 1998.
- [63] N. G. Chen and J. Bai. Monte carlo approach to modeling of boundary conditions for the diffusion equation. *Phys. Rev. Lett.*, 80:5321–4324, 1998.
- [64] A. D. Kim and A. Ishimaru. Optical diffusion of continuous-wave, pulsed, and density waves in scattering media and comparisons with radiative transfer. *Appl. Opt.*, 37:5313–5319, 1998.

- [65] R. Aronson. Photon diffusion coefficient in an absorbing medium. *J. Opt. Soc. Am. A*, 16:1066–1071, 1999.
- [66] W. Cai, M. Xu, M. Lax, and R. R. Alfano. "Diffusion coefficient depends on time, not on absorption". *Optics Letters*, 27:731–733, 2002.
- [67] R. Elaloufi, R. Carminati, and J.-J. Grefet. "Definition of the diffusion coefficient in scattering and absorbing media". *J. Opt. Soc. Am. A*, 20:678–685, 2003.
- [68] T. Durduran and D. A. Boas A. G. Yodh, B. Chance. "Does the diffusion coefficient depend on absorption?". *J. Opt. Soc. Am. A*, 14:3358–3365, 1997.
- [69] D. J. Durian. The diffusion coefficient depends on absorption. *Opt. Lett.*, 23:1502–1504, 1998.
- [70] G. Zaccanti M. Bassani, F. Martelli and D. Contini. Independence of the diffusion coefficient from absorption: experimental and numerical evidence. *Opt. Lett.*, 22:853–855, 1997.
- [71] J. Ripoll, D. Yessayan, G. Zacharakis, and V. Ntziachristos. Experimental determination of photon propagation in highly absorbing and scattering media. *J. Opt. Soc. Am. A*, 22(3), 2004.
- [72] R. Aronson and N. Corngold. Photon diffusion coefficient in an absorbing medium. *J. Opt. Soc. Am. A*, 16:1066–1071, 1999.
- [73] G. Holte. On a method of calculating the density of neutrons emitted from a point source in an infinite medium. *Ark. Mat. Astron. Fys.*, 35A:1–9, 1948.
- [74] C. Garofalakis, G. Zacharakis, G. Filippidis, E. Sanidas, D.D. Tsiftsis, E. Stathopoulos, M. Kafousi, J. Ripoll, and T.G. Papazoglou. Characterization of the reduced scattering coefficient for optically thin samples: theory and experiments. *J. Opt. A: Pure Appl.*, 6(7).
- [75] E. E. Graves, J. Ripoll, R. Weissleder, and V. Ntziachristos. A submillimeter resolution fluorescence molecular imaging system for small animal imaging". *Medical Physics*, 30:901–911, 2003.
- [76] M. Born and E. Wolf. *Principles of Optics*. University Press, Cambridge, 7 edition, 1999.
- [77] B. Chance D. A. Boas, M. A. O'Leary and A. G. Yodh. Scattering of diffusive photon density waves by spherical inhomogeneities within turbid media: Analytic solution and applications. *Proc. Natl. Acad. Sci.*, 19:4887–4891, 1994.

- [78] B. Chance D. A. Boas, M. A. O'Leary and A. G. Yodh. Scattering and wavelength transduction of diffuse photon density waves. *Phys. Rev. E*, 47:R2999–R3002, 1993.
- [79] B. Chance D. A. Boas, M. A. O'Leary and A. G. Yodh. Detection and characterization of optical inhomogeneities with diffuse photon density waves: a signal-to-noise analysis. *Appl. Opt.*, 36:75–92, 1997.
- [80] B. Chance M. A. O'Leary, D. A. Boas and A. G. Yodh. Experimental images of heterogeneous turbid media by frequency-domain diffusing-photon tomography. *Opt. Lett.*, 20:426–428, 1995.
- [81] M.A. O'Leary, D.A. Boas, X.D. Li, B. Chance, and A.G. Yodh. Fluorescence lifetime imaging in turbid media. *Opt. Lett.*, 21(2):158–160, 1996.
- [82] J. Ripoll and M. Nieto-Vesperinas. Scattering integral equations for diffusive waves. detection of objects buried in diffusive media in the presence of rough interfaces. *J. Opt. Soc. Am. A*, 16:1453–1465, 1999.
- [83] M. Born and E. Wolf. *Principles of Optics*. Pergamon Press, New York, 6th edition, 1993.
- [84] R. Aronson. Boundary conditions for diffusion of light. *J. Opt. Soc. Am. A*, 12:2532–2539, 1995.
- [85] R. C. Haskell, L. O. Svaasand, and B. J. Tromberg. Boundary conditions for the diffusion equation in radiative transfer. *J. Opt. Soc. Am. A*, 11:2727–2741, 1994.
- [86] A. Soubret and V. Ntziachristos. Fluorescence molecular tomography in the presence of background fluorescence. *Phys. Med. Biol.*, 51:3983–4001, 2006.
- [87] R. Schulze, D. D. Bruellmann, F. Roeder, and B. d'Hoedt. Determination of projection geometry from quantitative assessment of the distortion of spherical references in single-view projection radiography. *Med. Phys.*, 31(10):2849–54, 2004.
- [88] H. Meyer, A. Garofalakis, G. Zacharakis, S. Pscharakis, C. Mamalali, D. Kioussis, E.N. Economou, V. Ntziachristos, and J. Ripoll. A multi projection non contact fluorescence tomography setup for imaging arbitrary geometries. *Appl. Opt.*, in press, 2007.
- [89] J. Sikora, A. Zacharopoulos, A. Douiri, M. Schweiger, L. Horesh, S. Arridge, and J. Ripoll. Diffuse photon propagation in multilayered geometries. *Phys. Med. Biol.*, 51:2849–2854, 2006.
- [90] J. Ripoll and M. Nieto-Vesperinas. Scattering integral equations for diffusive waves. detection of objects buried in diffusive media in the presence of rough interfaces. *J. Opt. Soc. Am. A.*, 16:1453–1465, 1999.

- [91] J. Ripoll, V. Ntziachristos, R. Carminati, and M. Nieto-Vesperinas. The kirchhoff approximation for diffusive waves. *Phys. Rev. E*, 64:051917, 2001.
- [92] J. Ripoll and V. Ntziachristos. From finite to infinite volumes: Removal of boundaries in diffuse wave imaging. *Phys. Rev. Lett.*, 96(17):173903, 2006.
- [93] J. De Boer, A. Williams, G. Skavdis, N. Harker, M. Coles, M. Tolaini, T. Norton, K. Williams, K. Roderick, A. J. Potocnik, and D. Kioussis. Transgenic mice with hematopoietic and lymphoid specific expression of cre. *Eur. J. Immunol.*, 33:314–325, 2003.
- [94] A. Akhmanova, A.L. Mausset-Bonnefont, W. van Cappellen, N. Keijizer, C.C. Hoogenraad, T. Stepanova, K. Drabek, J. van der Wees, M. Mommaas, J. Onderwater, H. van der Meulen, M.E. Tanenbaum, R.H. Medema, J. Hoogerbrugge, J. Vreeburg, E.J. Uringa, J.A. Grootegoed, F. Grosveld, and N. Galjart. The microtubule plus-end-tracking protein clip-170 associates with the spermatid manchette and is essential for spermatogenesis. *Genes and Development*, 19:2501–2515, 2005.
- [95] R. Cubeddu, A. Pifferi, P. Taroni, A. Torricelli, and G. Valentini. "A solid tissue phantom for photon migration studies". *Phys. Med. Biol.*, 42:1971–1979, 1997.
- [96] J.R. Walls, J.G. Sled, J. Sharpe, and R.M. Hankelman. Correction of artefacts in optical projection tomography. *Phys. Med. Biol.*, 50:4645–4665, 2005.
- [97] XENOGEN. http://www.xenogen.com/wt/page/ivis_200.
- [98] C.A. Janeway, P. Travers, M. Walport, and M. Shlomchik, editors. *Immunobiology*. Garland Publ., New York, 2001.
- [99] N. C. Shaner, R. E. Cambell, P. A. Steinbach, B. N. G. Giepmans, A. E. Palmer, and R. Y. Tsien. Improved monomeric red, orange and yellow fluorescent proteins derived from discosoma sp. red fluorescent protein. *Nat. Biotechnol.*, 22(12):1567–1572, 2004.
- [100] J. Zhang, R. E. Cambell, A. Y. Ting, and R. Y. Tsien. Creating new fluorescent probes for cell biology. *Nat. Biotechnol.*, 3:906–918, 2002.
- [101] B. J. Bevis and B. S. Glick. Biochemistry, mutagenesis, and oligomerization of dsred, a red fluorescent protein from coral. *Nat. Biotechnol.*, 20:83–87, 2002.
- [102] L. et al Wang. Evolution of new antibody proteins via iterative somatic hypermutation. *Proc. Natl. Acad. Sci.*, 101:16745–16749, 2004.
- [103] X. Gao, Y. Cui, R.M. Levenson, W.K. Chung, and S. Nie. In vivo cancer targeting and imaging with semiconductor quantum dots. *Nat. Biotechnol.*, 22:969–976, 2004.

- [104] R.M. Levenson. Spectral imaging and pathology: seeing more. *Lab. Med.*, 35:244–251, 2004.
- [105] T. Zimmermann, J. Rietdorf, and R. Pepperkok. Spectral imaging and its applications in live cell microscopy. *FEBS Lett.*, 546:87–92, 2003.

Appendix A Related biological terms¹

DNA: The entire body of genetic information required to form and sustain life is contained in the DNA molecule. Most living entities, including viruses and bacteria, fungi, plants, animals, and humans use this universal instruction language. DNA is composed of four chemical bases: adenine, thymine, cytosine and guanine. Strands of these bases pair with each other (adenine and thymine, cytosine and guanine) to form a structure that resembles a ladder (see figure[8.1]). The entire ladder is compacted around other proteins (involved in maintaining structure and regulating gene expression) and is referred to as a chromosome. Collectively the 23 chromosome pairs in human cell are referred to as the human genome.

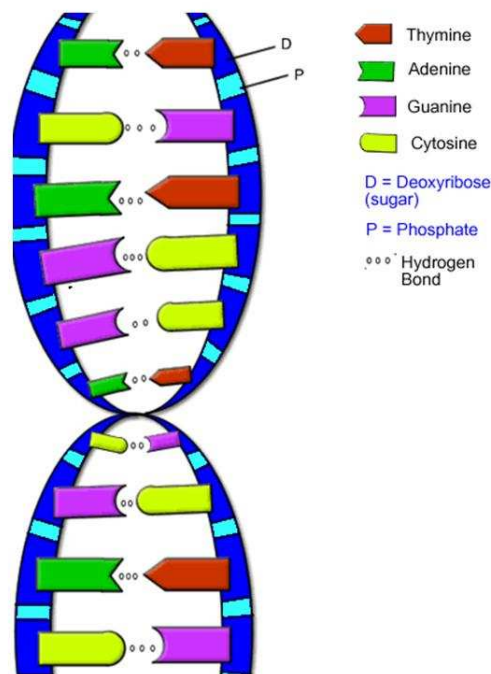


Figure 8.1: the DNA double strand

Gene expression: A single gene typically consists of several thousand base pairs. There are

¹sources: a)"Fluorescent proteins as a toolkit for in vivo imaging", Chudakov D.M., Lukyanov S., Lukyanov K.A., Trends in Biotechnology, **23**, p. 605-613,(2005), "Molecular imaging in living subjects: seeing fundamental biological processes in a new light", Massoud T.F., Gambhir S.S., Genes and development **17**, p. 545-580(2003), "Molecular Biology of the Cell", Alberts B., Johnson A., Lewis J., Raff M., Roberts K., Walter, P. Garland Science, New York (2002), "Molecular Imaging" Weissleder R., Mahmood U., Radiology, **219**, p.316-333(2001)

an estimated 60000-100000 genes in the human genome. Gene expression is the process by which a gene's DNA sequence is converted (encoded) into the functional proteins of the cell. Gene expression is a multi-step process that begins with *transcription* of DNA into messenger RNA (mRNA)(see figure[8.2]). The DNA strands separate, and the mRNA molecule is synthesized by using the DNA as a template. After this, mRNA leaves the cell through the cytoplasm. The second main process of Gene expression is *translation*. In *translation*, mRNA is decoded to produce a specific amino acid chain (protein). In other words, the mRNA molecule acts as a template for the final products: proteins. The estimated 80000 proteins perform all functions of life inside and outside cells.

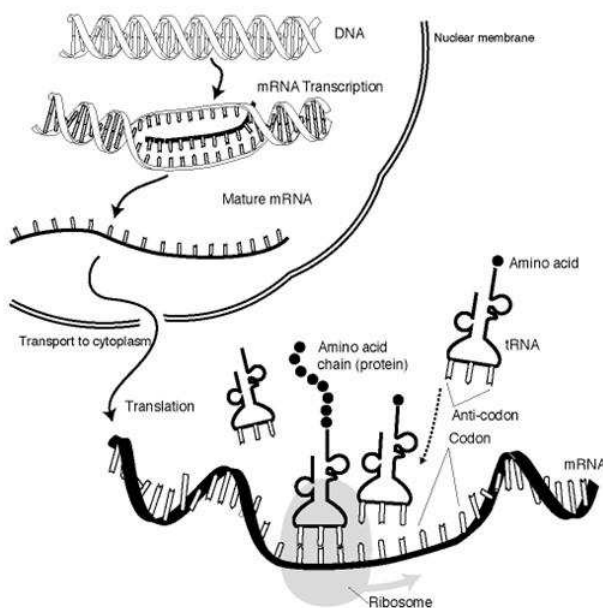


Figure 8.2: the steps of the gene expression process

Knowledge of the sequence of the human genome allows the identification and understanding of the function of all human genes. The Human Genome Project is an effort to decipher the specific sequence of all human genes. Apart for the human genome project, the decoding of many genomes has already completed (*Escherichia coli*, *Mycoplasma pneumoniae*, *Haemophilus influenzae*, *Saccharomyces cerevisiae*, *Helicobacter pylori*) while the decoding of the mouse genome is currently underway.

Mouse as a model for mammals: The mouse, being small and a rapid breeder has become the foremost model organism for experimental studies. Another reason is the genetic similarity between mice and humans. Many human genes have a related mouse version, which makes it possible to gain insights into human disease. There are efforts to sequence the entire mouse genome in analogy to the Human Genome Project. Mouse models of human disease will then be more easily developed, facilitating the understanding of gene function in health and disease.

Transgenic mice: Animals that have been permanently reengineered by either gene insertion, gene deletion or gene replacement are called *transgenic organisms* and any foreign or modified genes that are added are called *transgenes*. Transgenic mice are genetically engineered to contain additional foreign genes in every cell allowing them to be used to study gene function and to model human diseases

Reporter genes: Intense exploration is taking place in the biological sciences to determine the patterns of gene expression that encode normal biological processes. There is also a growing belief that diseases result from alterations in normal *regulation*² of gene expression that transition cells to *phenotype*³ of disease. These alterations in gene expression can result from interactions with the environment, hereditary deficits, developmental errors and aging process. A reporter gene is a gene that researchers attach to another gene of interest for the study of its function. Reporter genes are generally used to determine whether the gene of interest has been expressed in the cell or organism population.

Fluorescent proteins: are commonly used as reporter genes products to monitor gene expression by attaching the target gene. A number of gene products with fluorescent properties have been described. The best known reporter genes is the those that encode for the green fluorescent protein(GFP) and the enzyme *Luciferase*, which catalyzes a reaction with *luciferin* to produce light.

GFP: is an excellent marker for labeling of proteins in terms of specificity. GFP was discovered in the hydroid jellyfish *Aequorea victoria*. GFP is widely used as noninvasive probes to study different biological models-from individual cells to whole organisms. The use of GFP enables the tracking of every step of the protein of interest: expression, localization, movement, interaction and activity in the cell, tissue or organism.

A transgenic organism can be made with the gene encoding for GFP attached to the target gene; this then gives a directly visible display of the gene's expression pattern in the living organism. Optical imaging systems allow the noninvasive recording of fluorescent signals from within the intact organism and thus the gene products can be monitored. In the last few years, there has been a veritable explosion in the field of molecular imaging, with the aim of determining location, duration and extent of gene expression within intact living systems.

²the process through which the cell determines-through interactions among DNA, RNA, proteins and other substances-when and where genes will be activated and how much gene product will be produced.

³the observable properties of an organism, resulting form the interaction between organism's genotype and the environment in which it develops

Ευχαριστίες

Κατά τη διάρκεια της πραγματοποίησης της εργασίας αυτής ήμουν τυχερός ώστε να έρθω σε επαφή με αξιόλογους ανθρώπους, η αλληλεπίδραση με τους οποίους ήτανε πολύ σημαντική για εμένα. Η ολοκλήρωση μίας ερευνητικής εργασίας δεν είναι υπόθεση ενός ανθρώπου αποκλειστικά αλλά μία συλλογική προσπάθεια. Γι' αυτό, θα ήθελα να ευχαριστήσω τους παρακάτω ανθρώπους οι οποίοι συμβάλλανε στο να έρθει σε πέρας η παρούσα εργασία.

Καταρχήν θα ήθελα να ευχαριστήσω τον καθ. κ. Ελευθέριο Οικονόμου ο οποίος με εμπιστεύθηκε σαν υποψήφιο διδάκτορα και του οποίου οι εύστοχες συμβούλες με βοήθησαν στο να βελτιώνομαι συνεχώς.

Ένα μεγάλο ευχαριστώ είναι λίγο για να περιγράψω την ευγνωμοσύνη μου προς τον δρ. κ. Jorge Ripoll για την συναρπαστική καθοδήγησή του και την υπομονή του ως προς το πρόσωπο μου. Αισθάνομαι τυχερός που τον γνώρισα και θαυμάζω το μοναδικό του τρόπο στο να προσεγγίζει τις προκλήσεις της έρευνας.

Ένα μεγάλο ευχαριστώ στην δρ κ. Κλείω Μαμαλάκη, για την καθοδήγηση της σε θέματα βιολογικού χαρακτήρα και για την όμορφη συνεργασία που είχαμε. Με βοήθησε να καταλάβω πολλά πράγματα στον τομέα της Βιολογίας ο οποίος στα μάτια μου φάνταζε σαν ο «μεγάλος άγνωστος» τουλάχιστον στο ξεκίνημα της παρούσας εργασίας.

Θέλω να ευχαριστήσω επίσης τον καθ. κ. Φωτάκη για την ευκαιρία που μου έδωσε να εργαστώ στο ερευνητικό περιβάλλον του Ι.Τ.Ε..

Η σχέση μου με τον δρ κ. Γιάννη Ζαχαράκη δεν περιορίζεται στα όρια της δουλειάς και μόνο. Υπήρξε οδηγός στα πρώτα βηματά μου στα εργαστήρια του Ι.Τ.Ε. και εξακολουθεί να αποτελεί για μένα πρότυπο πειραματικού.

Θα ήθελα να ευχαριστήσω το συνεργάτη μου υποψήφιο διδάκτορα Heiko Meyer για την συνεργασία που είχαμε κυρίως στο ξεκίνημα αυτής της εργασίας. Προευτήκαμε για μεγάλο χρονικό διάστημα μαζί και σημαντικό μέρος από την εξέλιξη της διάταξης ανήκει σε αυτόν.

Έιχα την τύχη όχι μόνο να συνεργαστώ άλλα και να συναναστραφώ με αξιόλογους ανθρώπους που με βοήθησαν ο καθένας με τον τρόπο του στο να έρθει σε πέρας αυτη η εργασία. Θέλω λοιπόν να ευχαριστήσω τον συνοδοιπόρο Μπούνο Γιάννη για το ότι μοιραστήκαμε τις ανησυχίες και τις χαρές μίας διδακτορικής εργασίας, τον δρ Γιώργο Φιλιππίδη γιατί ήταν πάντα εκεί όταν τον χρειαζόμουνα, τους Rosy Favvichio, Στέλιο Ψυχαράκη, Ana Sarasa, Juan Aguirre, Αλέξανδρο Darrell, Γεωργία Φουστέρη και Γιάννη Χατζιδάκη για τις εργαστηριακές ώρες που περάσαμε μαζί και για τις συζητήσεις πάνω σε θέματα ερευνητικού και όχι μόνο χαρακτήρα.

Θα ήθελα, επίσης, να ευχαριστήσω τους μηχανουργούς του Ι.Τ.Ε. για το μεράκι τους και τις ιδέες τους προκειμένου να υλοποιήσουν τα ομολογουμένως εξεζητημένα κάποιες φορές μηχανολογικά μας σχέδια.

Η περάτωση μίας διδακτορικής διατριβής είναι μία απαιτητική διαδικασία που αποτελεί μία περιπέτεια από την μια αλλά και μια δοκιμασία από την άλλη. Θέλω να ευχαριστήσω όσους στάθηκαν στο πλάι μου και έδειξαν υπομονή στο πρόσωπό μου τις ώρες εκείνες που η αφοσίωση μου στις απαιτήσεις της εργασίας στάθηκαν εμπόδιο στην επικοινωνία μας.

Η εργασία αυτή αφιερώνεται στους γονείς μου Μανόλη και Ευαγγελία Γαροφαλάκη. Τους ευχαριστώ για την αμέριστη υλική και ψυχική τους συμπαράσταση. Αποτελούν για μένα παραδείγματα εργατικότητας, ήθους και αφοσίωσης, στοιχείων απαραίτητων για την επίτευξη οποιουδήποτε στόχου.